# Synthesis and characterization of $ZrO_2$ dispersion strengthened Fe based alloys

*By*
**RAGHAVENDRA K. G**
**PHYS 02 2012 04 004**

**Indira Gandhi Centre for Atomic Research, Kalpakkam**

***A thesis submitted to the***

***Board of Studies in Physical Sciences***

***In partial fulfillment of requirements***
***for the Degree of***
**DOCTOR OF PHILOSOPHY**
***of***
**HOMI BHABHA NATIONAL INSTITUTE**

**August, 2017**

# Homi Bhabha National Institute[1]

## Recommendations of the Viva Voce Committee

As members of the Viva Voce Committee, we certify that we have read the dissertation prepared by Raghavendra K. G. entitled "**Synthesis and characterization of $ZrO_2$ dispersion strengthened Fe based alloys**" and recommend that it may be accepted as fulfilling the thesis requirement for the award of Degree of Doctor of Philosophy.

G. Amarendra May 14, 2018

Chairman – Dr. G. Amarendra **Date:**

14/05/2018

Guide / Convener – Dr. Arup Dasgupta **Date:**

Examiner – Prof. Rahul Mitra **Date:** 14-05-2018

Rahul Mitra

Member 1- Dr. R. Divakar **Date:**

14/05/2018

Member 2- Dr. R. Rajaraman **Date:**

14/5/18

Final approval and acceptance of this thesis is contingent upon the candidate's submission of the final copies of the thesis to HBNI.

I/We hereby certify that I/we have read this thesis prepared under my/our direction and recommend that it may be accepted as fulfilling the thesis requirement.

**Date:** 14th May, 2018

**Place:** Kalpakkam

**Guide**

# STATEMENT BY AUTHOR

This dissertation has been submitted in partial fulfillment of requirements for an advanced degree at Homi Bhabha National Institute (HBNI) and is deposited in the Library to be made available to borrowers under rules of the HBNI.

Brief quotations from this dissertation are allowable without special permission, provided that accurate acknowledgement of source is made. Requests for permission for extended quotation from or reproduction of this manuscript in whole or in part may be granted by the Competent Authority of HBNI when in his or her judgment the proposed use of the material is in the interests of scholarship. In all other instances, however, permission must be obtained from the author.

Raghavendra K. G.

# DECLARATION

I, hereby declare that the investigation presented in the thesis has been carried out by me. The work is original and has not been submitted earlier as a whole or in part for a degree / diploma at this or any other Institution / University.

Raghavendra K. G.

# List of Publications arising from the thesis

## *Journal Publications*

### a) Published

1. "Synthesis and characterization of Fe-15 wt.% $ZrO_2$ nanocomposite powders by mechanical milling"
   **K. G. Raghavendra**, A Dasgupta A, P Bhaskar P, K Jayasankar K, Athreya C. N, Panda P, Saroja S, Subramanya Sarma V, Ramaseshan R.
   **Powder Technology** 287, 190-200, 2016

2. "Thermal Evolution of Nano-crystalline Fe - 15 Wt. % $ZrO_2$ composite: Insights from calorimetric and microscopy investigations"
   **K. G. Raghavendra**, Arup Dasgupta, Raj Narayan Hajra, K. Jayasankar, V Srihari, S. Saroja.
   **Materials Characterization,** 132, 448-457, 2017

3. Development of a novel $ZrO_2$ dispersion strengthened 9Cr ferritic steel: Characterization of milled powder and subsequent annealing behavior
   **K. G. Raghavendra**, Arup Dasgupta, K. Jayasankar, V. Srihari and S. Saroja
   **"Powder Technology",** 327, 267-274, 2018

4. "Microstructural evolution of nanocrystalline $ZrO_2$ in a Fe matrix during high-temperature exposure"
   **K. G. Raghavendra**, Arup Dasgupta, , Athreya C. N, K. Jayasankar, S. Saroja, V. Subramanya Sarma.
   Accepted Manuscript in **"Metallurgical and Materials Transactions A"**

## *Conference proceedings*

1. "Novel $ZrO_2$ dispersion strengthened 9 Cr steel: Synthesis and Microstructural Characterization"
   **Raghavendra K. G**, Vaishnavi Krupa B. R, Arup Dasgupta, Karthiselva N.S, Jayasankar V, Saroja S and Srinivasa Rao Bakshi; International Conference on Electron Microscopy and XXXVIII Annual Meeting of the Electron Microscope Society of India, EMSI-2017, July 17-19, 2016, Mahabalipuram, India. ISBN No. 978–81–933428-1-7, Page # 233-235

## *Conference presentations*

1. "Synthesis and Microstructural Characterization of Zirconium Oxide dispersion strengthened model alloy and 9 Cr Ferritic Steel"
   **K. G. Raghavendra**, Arup Dasgupta, Raj Narayan Hajra, K. Jayasankar and S. Saroja; TMS 2017, 146th Annual Meeting and Exhibition, February 26 - March 2, 2017, San Diego, USA

2. "Microstructural evolution of $ZrO_2$ dispersion strengthened Ferritic Steel Powder during milling and subsequent annealing"
   **K. G. Raghavendra**, Arup Dasgupta, K. Jayasankar and S. Saroja; International Symposium for Research Scholars, ISRS-2016, December 21-23, 2016, IIT-Madras, Chennai, India

3. "Synthesis and Characterization of $ZrO_2$ dispersion strengthened Ferritic Steel Powder"
   **K. G. Raghavendra**, Arup Dasgupta, K. Jayasankar and S. Saroja; International Conference on Electron Microscopy and XXXVII Annual Meeting of the Electron Microscope Society of India, EMSI-2016, June 2-4, 2016, IIT BHU - Varanasi, India.

4. "Microstructural investigation of dispersoids in annealed Fe based model ODS alloy using in-situ FIB"
   **K. G. Raghavendra**, P. K. Parida, Arup Dasgupta, K. Jayasankar and S. Saroja; International Conference on Electron Microscopy and XXXVI Annual Meeting of the Electron Microscope Society of India, EMSI-2015, July 6 – 10, 2015, Mumbai, India

5. "Microstructural Characterization of $ZrO_2$ dispersoids during annealing in Fe-15 Wt. % $ZrO_2$ model ODS alloy"
   **K. G. Raghavendra**, P. K. Parida, Arup Dasgupta, K. Jayasankar and S. Saroja; 52nd National Metallurgists Day and 68th Annual Technical Meeting, November 12 - 15, 2014, College of Engineering, Pune, India.

6. "Synthesis and characterization of $ZrO_2$ dispersoid strengthened Fe based model ODS alloy"
   **K. G. Raghavendra**, Pradyumna Kumar Parida, K. Jayasankar, Arup Dasgupta and S. Saroja; International Conference on Electron Microscopy and XXXV Annual Meeting of the Electron Microscope Society of India, EMSI-2014, July 7-11, 2014, University of Delhi, India.

Raghavendra K. G.

**Thesis dedicated to**

**my parents,**

**Mr. Gururaj Bhat and**

**Mrs. Suryakala Devi**

# *Acknowledgements*

It all began with an uncertain and perplexed state of mind, back in 2012. Since then, it has been a journey with ups and downs filled with moments of joy and sorrow. At the end, I feel immensely pleasured to reach my destiny on a satisfactory note. For sure, I will begin my next journey with much credence. Herewith, I wish to recall all those, who made this journey worthy and memorable.

I express my deepest sense of gratitude to my beloved supervisor Dr. Arup Dasgupta, for his guidance, constant support and for keeping faith in me all these years. I am grateful to him for shaping my career and showing the path to flourish. I thank him for allowing me to learn by mistakes and for inspiring me to be a better version of myself.

I do not have words to render thanks to Mr. Pradyumna Kumar Parida and Mrs. Pragna Bhaskar, for being my mentors, especially during my initial days and teaching me all the tricks of the trade. I thank them for their love and support in reaching me this level.

I thank Dr. Saroja Saibaba, Associate Director, Materials Characterization Group, Dr. M. Vijayalakshmi, former Associate Director, Physical Metallurgy Group, Dr. S. Raju, Head, Physical Metallurgy Division for their consistent encouragement with dutiful management in providing me the necessary infrastructure and resources to accomplish my research work in this group.

I wish to sincerely thank my Doctoral Committee for evaluating my work periodically and providing valuable suggestions which greatly helped me to enhance the quality of my research work. I thank my Chairman Dr. G. Amarendra, Head, Metallurgy and Materials Group and members Dr. R. Divakar and Dr. R. Rajaraman for the same.

I am indebted to my research collaborators for being supportive during this journey and providing the necessary scientific inputs. On this occasion, I thank, Dr. K. Jayasankar, Senior Scientist, IMMT Bhubaneshwar, Dr. Srihari, Scientist, RRCAT, Indore, Dr. V. S. Sarma, Associate Professor, IIT Madras, Mr. C. N. Athreya, IIT Madras, Dr. R. Ramaseshan, Dr. Magudapathy, MSG – IGCAR, Dr. Sujoy, UGC-DAE, Mr. Padmalochan Panda and Mr. Raj Hajra, for all your supports.

I would like to extend my heartfelt thanks to Dr A. K. Bhaduri, Director, IGCAR, for allowing me to pursue research in this esteemed institute and for providing the necessary infrastructure.

I express my hearty thanks to Dr. R. Mythili, Dr. V. Thomas Paul, Dr. Sudha, Dr. Prasanthi, Mr. Manmath Kumar Dash, Mrs. Alphy and Dr. Chanchal Ghosh for their constant support and encouragement.

The strong co-operation and kind support of all the members of Physical Metallurgy Division is deeply acknowledged.

I thank Dr. M. Saibaba for providing with a calm stay at JRF Enclave and also for his encouragement.

I acknowledge Mr. Sridhar, Mr. Gururaj Kadiri and Mrs. Kalavathi, MSG for introducing me to IGCAR as a STIP student and for being supportive all these years.

I am indebted to all my senior / junior research scholar friends from Physical Metallurgy Division, for their co-operation and help. I am remembering and thanking Ravi, Sabeena, Thangam, Santhosh, Siva, Sai, Suresh, Shreevalli, Vaishnavi and Soham on this occasion.

I thank my research scholar friends who helped me in many ways towards completion of this thesis. I thank Devidas, Mahendran, Karthikeyan, Shashwath, Subrth, Manas, Sanjay, Jai Ganesh, Mohandoss, Gopi, Srini, Raghav, Yad, Bala, Sravanthi, Sumathi, Chandan, Naveen, Vairavael, Lakshmanan, Radhikesh, Irshad, Nila, Zaibudden, Enclave shuttlers and cricketers for bearing with me and help keeping me sane all these days.

Special thanks to “Kudla” gang, Sharath, Santhosh, Pavan, Madhura, Sumana, Suma, Valli, Vaish for their love, affection and the for the weekend food.

Thanks to my buddies Preethi, Janani, Karthika for their everlasting love. Thanks to Mr. Madhan, for his brotherly affection.

I take this opportunity to remember the affection and support of my family members who are the backbone for all my endeavors. I dedicate this Thesis to my parents Mr. Gururaj Bhat and Mrs. Suryakala Devi, who takes all the credit of what I am today. I also wish to thank my sisters Mrs. Shwetha Ananthesh and Mrs. Shantha Shrikanth for their love. I also thank my niece Ashmitha and Shravya for their unconditional love.

I thank god for this beautiful life.

# CONTENTS

## CHAPTER III - SYNTHESIS AND MICROSTRUCTURAL CHARACTERIZATION OF Fe - 15 Wt.% $ZrO_2$ MODEL ALLOY

## CHAPTER IV - THERMAL EVOLUTION OF NANO-CRYSTALLINE Fe - 15 Wt. % $ZrO_2$ MODEL ALLOY

## CHAPTER V - SYNTHESIS AND CHARACTERIZATION OF $ZrO_2$ DISPERSED 9Cr STEEL POWDER

## CHAPTER VI - MICROSTRUCTURAL CHARACTERIZATION OF CONSOLIDATED $ZrO_2$ DISPERSION STRENGTHENED FERRITIC STEEL

## CHAPTER VII - SUMMARY AND FUTURE SCOPE

# SYNOPSIS

The sustainable development of a country largely depends on the energy resources it possesses. This energy is required to support its expanding economy, fulfill the growth ambitions and for domestic purposes. Sustainable energy production is a global challenge and can be met only with judicious choice of energy resources which includes efficient utilization of conventional energy resources and by developing the alternate energy resources [1-3]. The choice of nuclear fusion and Generation IV fission nuclear power plants becomes important here because they are bestowed with a low release of green-house effect gases which makes them viable to produce the energy required to satisfy the growing demand and limit the global warming.

Economic operation of a fission / fusion reactor requires an efficient usage of the fuel it consumes, which depends on the material which houses the fuel. Limitations on prolonged residence time of the fuel arise from the property degradation of the core structural material (clad) due to high-temperature creep and void swelling, which need to be addressed. Special interest exists in developing high strength and radiation damage resistant materials and Oxide Dispersion Strengthened (ODS) alloys have emerged as a new class of materials bestowed with these properties [4-9]. Specific to the nuclear environment, ODS ferritic steels have gained prominence over their austenite counterparts, as, the relatively open bcc structure of ferritic steels are known to possess inherently superior irradiation resistance than the close packed fcc [10, 11] structure. Fine dispersions of ceramic particles are added either to the elemental or to the alloy powders and mechanically milled to get uniform dispersion. These fine dispersions lead to increasing strength parameters by impeding the dislocation movement, which brings about significant improvement in its high-temperature creep resistance [4]. Additionally, these dispersoids are also known to enhance the void swelling resistance by acting as vacancy sinks [12].

Conventionally ODS alloys are dispersed with $Y_2O_3$. It needs to be mentioned here that, finer dispersoids and homogeneous dispersion in the matrix is an absolute necessity, in order to achieve the required strengthening; mainly because the volume fraction of dispersoids in the steel matrix is rather low (<< 1%). Fine dispersions having smaller interparticle spacing in the matrix are key to block the mobile dislocations, whereas the larger ones can be cut through or can even be bypassed easily when the inter-dispersoid spacing is large. By this way, typically an Ultimate Tensile Strength (UTS) of 500–550 MPa at 923K can be obtained [6]. For this class of powder metallurgically processed materials, a careful optimization of the mechanical milling conditions can reduce the dispersoid sizes to < 5 nm, leading to a high number density of dispersoids with smaller interparticle spacing in the matrix thereby increasing the high-temperature creep strength of such materials [13]. However, problem arises at temperatures above 873K, where $Y_2O_3$ has been reported to coarsen [14, 15], resulting in limitations to high-temperature processing and application of this material. This problem can be overcome with an addition of Ti to the matrix, which results in the precipitation of Y-Ti-O complex oxides measuring about ~ 2 - 6 nm in size [6, 16], thereby allowing the process temperatures to go up to 1423K and extending the long term thermal stability limit of these complex oxides to 1073K [14], consequently, the stability of the material.

## Scope of the Thesis

Although there are extensive research activities on $Y_2O_3$ – Ti dispersed ODS alloys [4-6, 12, 16-22], there is a dearth of literature on the potentiality of using other rare earth oxides as dispersoids in ODS materials. Some recent reports on exploring alternate dispersoids such as $La_2O_3$[23], $CeO_2$, $MgO_2$ and $ZrO_2$ [24] for ODS materials suggest superiority over $Y_2O_3$ and hence it is necessary to investigate them in detail. Thus, the current thesis focuses on investigating the possibility for an alternate oxide, namely $ZrO_2$, as dispersoid for strengthening the material.

Successful realization of alternative dispersoid ODS alloys would require a thorough understanding of the stability and microstructural evolution of the dispersoid during mechanical milling and subsequent stages involving exposure of the powder to high temperatures during consolidation and thermo mechanical treatments. Though alternate oxides have been tried to a little extent as reported in the literature, the focus was mainly on the final microstructure of the material and its mechanical properties, rather than on the dispersoid evolution during milling and annealing. Thus, in order to investigate suitability of an oxide as an effective dispersoid, in-depth studies concentrating on its structural evolution with milling and also at high temperatures is required. Further, in order to facilitate reliable characterization, it is necessary to choose a concentrated alloy with high dispersoid composition.

Keeping this in mind, the methodology applied in this study involves synthesis and detailed characterization of a model Fe - 15 Wt. % $ZrO_2$ system. The microstructure and microchemical evolution of this model system has been investigated as a function of milling duration to arrive at the optimized condition. Further the microstructural evolution of this model system with temperature is also been investigated. The knowledge accumulated on the behavior of dispersoids by these analyses were then utilized for developing a 9 Wt. % Cr ferritic steel. The behavior of as milled and annealed $ZrO_2$ dispersed steel powder has been evaluated and its consolidation properties using Spark Plasma Sintering (SPS) technique has also been investigated.

Present thesis entitled **“Synthesis and characterization of $ZrO_2$ dispersion strengthened Fe based alloys”** reports the results of the above experimental studies and is organized into seven chapters as outlined below.

### Chapter I: Introduction

This chapter begins with a brief introduction highlighting the material challenges for nuclear applications and gives an introduction to the ODS alloys. Historical perspectives of development of ODS alloys is given and a comprehensive literature survey has been provided on the choice of ODS alloys based on mechanical properties and radiation damage resistance. This is followed by a discussion on the criteria for selection of dispersoids for the ODS alloy for structural applications under harsh environments and literature reports on alternate oxides for dispersion strengthening. A section is dedicated to the discussion on the choice of $ZrO_2$ as candidate dispersoid in the current study and additionally, the rationale behind choosing the model alloy system for ODS is also been discussed with extensive literature on model alloy systems. The scope and organization of the thesis is also been detailed in this chapter.

### Chapter II: Materials and Methods

This chapter deals with the experimental techniques and procedures employed for the synthesis, characterization and evaluation of the structural, chemical and mechanical properties of Fe – 15 Wt. % $ZrO_2$ model system and $ZrO_2$ dispersed 9Cr steel. Mechanical milling is utilized for the synthesis of alloy powders and the working principle is described in this chapter. The major characterization tools utilized for understanding the microstructure are Scanning and Transmission Electron microscopy (SEM and Analytical/HRTEM) and X-Ray diffraction (Lab source and Synchrotron XRD) and this chapter provides a brief description on the same. Short note on specimen preparation for TEM is also given with special emphasis on Focused Ion Beam (FIB) technique for site specific TEM lamellae preparation from powder particles. Chemical analysis by Energy Dispersive Spectroscopy (EDS) and thermal analysis by Differential Scanning Calorimetry (DSC) is also described. Further, the chapter also consists of a brief description on the consolidation of powders through SPS. A concise note on Electron Backscatter Diffraction (EBSD) technique for texture study is also provided.

### Chapter III: Synthesis and microstructural characterization of Fe - 15 Wt. % $ZrO_2$ model alloy

In this chapter, a model Fe - 15 Wt. % $ZrO_2$ composite powder has been synthesized via mechanical milling with an aim to study the evolution of powder morphology and refinement of the oxide dispersoid and Fe crystallites during milling. Milling durations were varied as 0, 10, 30, 60 and 100h and detailed microstructural and microchemical investigations have been carried out on all the powder samples in order to optimize the milling conditions based on microstructural uniformity and microchemical homogeneity. A homogeneous mixture was confirmed by X-ray mapping after 100h. The $ZrO_2$ dispersoids were observed to retain crystallinity even after 100h of milling, as observed by XRD and confirmed through TEM. Statistical analysis of the Dark Field (DF) TEM micrographs indicated superior refinement of both matrix and dispersoid phase after 100h of milling. Modified Williamson-Hall technique (mod. W-H) was employed to measure the matrix crystallite size and dislocation density and it showed that dislocation density in the matrix increased from ~ $5 \times 10^{15}$ / $m^2$ at the onset of milling to ~ $2.3 \times 10^{16}$ after 100h milling indicating the severe plastic deformation of the Fe grains. Nanoindentation technique has been employed to evaluate the nano-hardness of the milled powder as a function of milling duration, which showed an increase in hardness from ~ 6 GPa at the beginning of the milling to ~ 11 GPa after 100h milling The results were in line with the dislocation density measurements. This chapter establishes that the optimized milling duration is 100h and $ZrO_2$ retains crystallinity even after this milling. Further, the thermal evolution of this powder and kinetics of $ZrO_2$ dispersoid growth is another crucial factor to be understood and dealt in the next chapter. The graphical summary of Chapter 3 is given below.

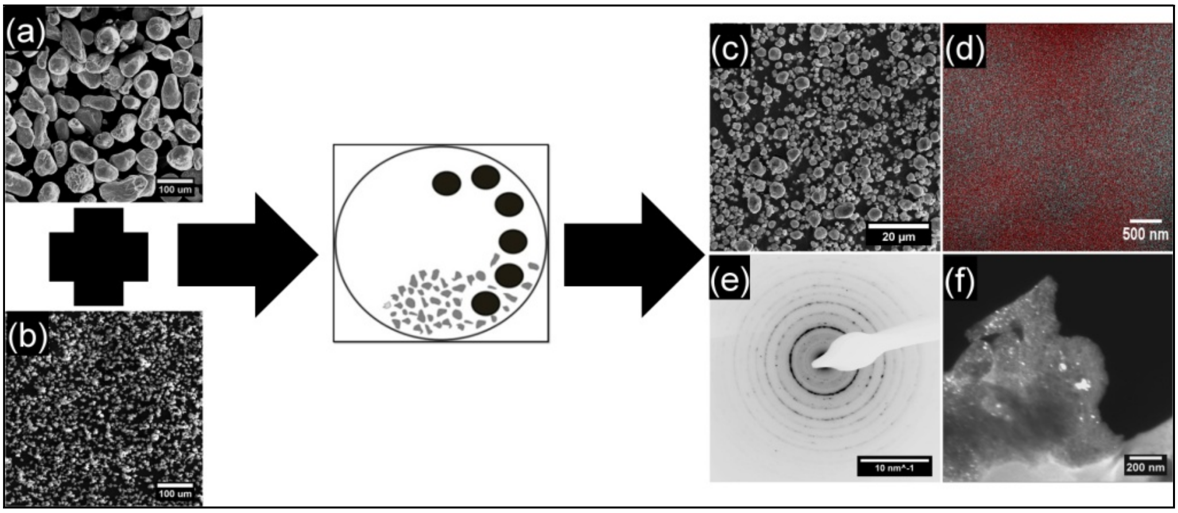

**Figure 1: Graphical summary of Chapter 3, showing Initial microstructure of (a) Fe and (b) $ZrO_2$. (c) Indicates the SE micrograph of 100h milled powder and (d) shows the X-ray mapping from a powder particle. (e) and (f) shows the Selected area diffraction pattern and DF micrograph corresponding to the $ZrO_2$ dispersoid.**

## Chapter IV: Thermal evolution of nanocrystalline Fe - 15 Wt. % $ZrO_2$ model alloy

This chapter presents the results on the evolution of phases during annealing of Fe - 15 Wt. % $ZrO_2$ model alloy system. The thermal behavior is assessed by means of DSC measurements and a comprehensive understanding on the thermal evolution of system is arrived with rigorous analysis through diffraction and microscopic techniques. The formation of FeO and $Fe_3O_4$ phases were observed under different conditions. These phases were studied using Synchrotron XRD techniques and analyzed by Rietveld refinement method. A metal deficient $Fe_{0.87}O$ phase was thus identified. Owing to its thermal stability as observed through synchrotron diffraction analysis, this phase, which may have resulted through reaction with residual oxygen in the matrix, is believed to be beneficial and deemed as an autogenous dispersion strengthener in the Fe matrix. The activation energy of formation of the $Fe_{0.87}O$ phase was estimated to be ~ 195 kJ $mol^{-1}$. Further, this phase was also found to be partially stabilizing the cubic phase of $ZrO_2$, at 923K, which was found to be unstable as it undergoes a cubic $\leftrightarrows$ tetragonal transformation at 1140K and the monoclinic phase reverts back after cooling it to room temperature. Further, this chapter also reports a broad peak for Fe $\alpha \rightarrow \gamma$ transformation in the calorimetry thermogram which is understood in terms of the nanocrystalline nature of the sample. Additionally, this chapter assesses the evolution of $ZrO_2$ crystallite size with time and temperature. It has been found that $ZrO_2$ retains its nanocrystallinity even after 600 min hold time at 1073K. The Arrhenius analysis of variation of crystallite size with time at different temperatures resulted in an activation energy of ~ 51 kJ $mol^{-1}$, which is rather low compared to the bulk. Nanocrystalline nature of the sample is assumed to be a possible reason for this variation.

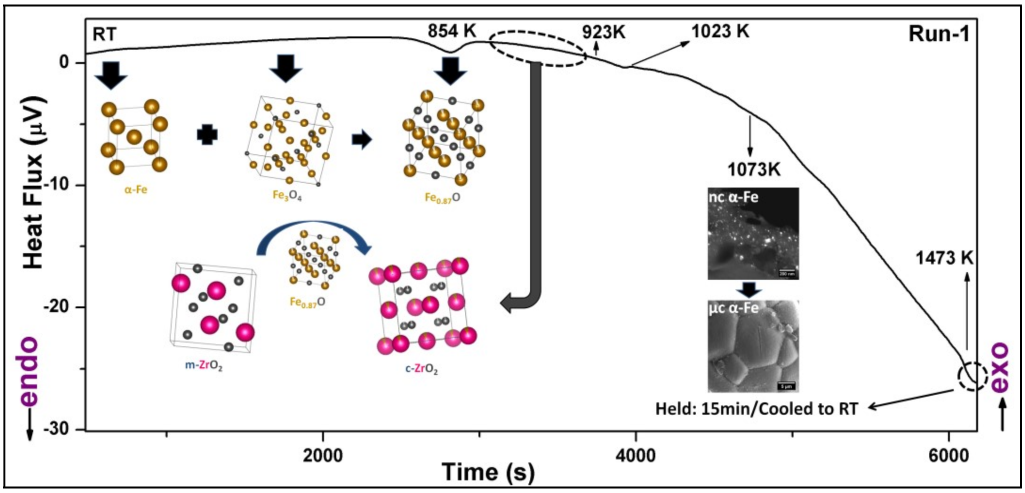

**Figure 2: The graphical summary of chapter IV. The formation of FeO phase upon annealing and phase transformation of $ZrO_2$ phase is indicated on a DSC thermogram. The size dependent α→γ phase transformation of Fe nanocrystallites is also indicated.**

## Chapter V: Synthesis and characterization of $ZrO_2$ dispersed 9Cr steel powder

Having established an alternate oxide suitable for dispersion strengthening in the earlier two chapters, this chapter reports the synthesis and characterization of $ZrO_2$ dispersoid strengthened ferritic steel powder (Fe-9Cr-2W-0.01C). The synthesis is carried out under optimized ball milling conditions arrived in the previous chapters. The analysis of milled powder showed powder particles of size ~ 1 - 10 µm, from an initial size of ~ 5 - 90 µm. The fine dispersions of $ZrO_2$ with a size range of 2 – 10 nm were also observed. Upon annealing at 1223K, precipitation of non-stoichiometric FeO (autogenous dispersoid) was observed along with $ZrO_2$ dispersoids. An excellent thermal stability has been manifested by both the dispersoids as it retained its fine structure during the annealing treatment with ~ 95% of dispersoids measuring < 11 nm for $ZrO_2$ and < 16 nm for the FeO. The matrix phase was also found to be nanocrystalline with nanometric grains. All the constituent phases are identified using Synchrotron XRD, Conventional and High Resolution TEM. This dual strengthening by $ZrO_2$ and FeO dispersoids along with nanostructured matrix is believed to play the major role in improving the high-temperature mechanical properties of the material being developed.

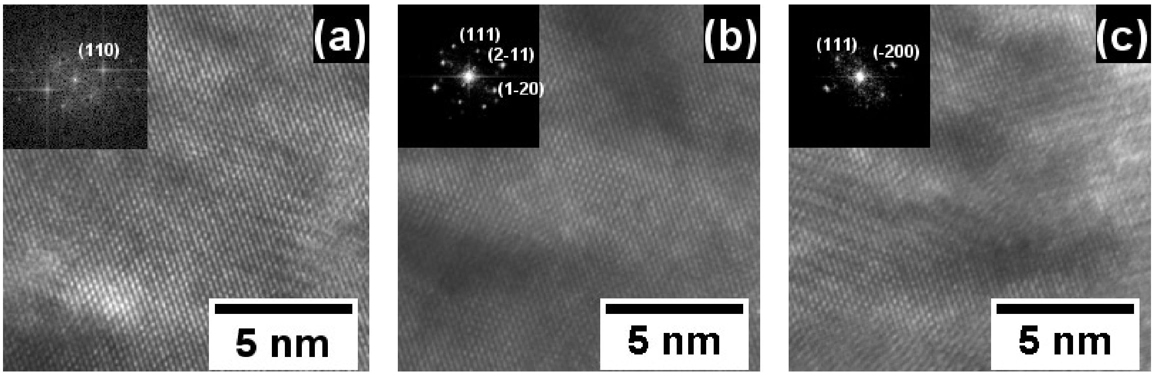

**Figure 3: Phase contrast micrographs corresponding to (a) Fe (b) m-$ZrO_2$ and (c) FeO. The power spectrum corresponding to the (a) (b) and (c) are shown as an inset.**

## Chapter VI: Microstructural characterization of consolidated $ZrO_2$ dispersion strengthened ferritic steel

The comprehensive understanding on the $ZrO_2$ dispersed steel powders from chapter V is utilized in SPS of the $ZrO_2$ dispersed steel powder with an objective to understand the consolidation behavior of the steel powder and the results obtained are summarized in this chapter. The density of sample consolidated through SPS was measured as ~ 94%. SEM analysis of the as sintered sample revealed fine grained microstructure with grains measuring ~ 1 – 5 μm. A normalizing and tempering treatment was carried out and TEM analysis revealed fine laths embedded in the ferritic matrix in the material. However, the lath structure was rather rare to observe, believed to be because of low C content in the steel. The dark field analysis of the $ZrO_2$ dispersoids revealed average dispersoid size to be ~ 6 nm, with fairly uniform distribution in the matrix. Long term thermal aging treatments were carried out at 973K for 400 h and 1000 h to understand the thermal effects microstructural stability. EBSD analysis revealed that average grains were polygonal and their size showed insignificant changes between 400 and 1000 h aged samples indicating excellent stability of the structure; brought about by Zener pinning from the nano-sized FeO and $ZrO_2$ dispersoids in the matrix. The hardness of the material was compared with conventional $Y_2O_3$ ODS and with RAFM. The SPS processed $ZrO_2$ ODS showed comparable hardness with $Y_2O_3$ ODS and higher than RAFM steel, indicating superior mechanical properties.

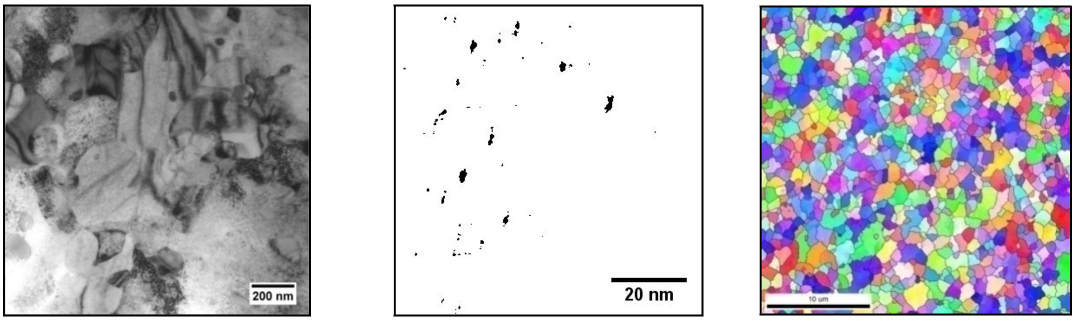

**Figure 4: (a) TEM micrograph of N&T $ZrO_2$ dispersed steel showing finer lath structure. (b) The processed image of $ZrO_2$ crystallites showing nano-dispersoids. (c) The grain structure of 1000h aged sample showing fine grains with an average size ~ 1.4 µm.**

## Chapter VII: Summary and future work

This chapter summarizes the salient features of the thesis and discusses the outcome of the described work and also presents the scope for the future work. The perceptive on exploring alternate dispersoids for ODS is scarce in literature and during the course of this work, the attempts have been made towards exploring $ZrO_2$ as an alternate to $Y_2O_3$ for dispersion strengthening. A model Fe - 15 Wt. % $ZrO_2$ composite was developed and characterized towards achieving comprehensive understanding on the behavior of $ZrO_2$ during prolonged milling and thermal exposure. The knowledge gained through this model system was utilized in developing 9Cr ferritic steel reinforced with $ZrO_2$ and the alloy was extensively characterized through Electron Microcopy and other techniques both in powder form and in consolidated state. Attempts are also made to answer several fundamental questions which arose during the course of study with an extensive experimental investigation. Through this thesis work, it is believed that foundation has been laid towards development of a new $ZrO_2$ dispersoid based ODS steel for high temperature structural applications.

## References

1. Dept. of Atomic Energy, *Annual Report of the Department of Atomic Energy, Government of India*. S.N. Gupta: 1992
2. Dept. of Atomic Energy, *The Saga of Atomic Energy Programme in India*. 2005
3. Sundaram, C. V.*, et al.*, *Atomic Energy in India, 50 Years*. Government of India, Department of Atomic Energy: 1998
4. Ukai, S.*, et al.*, *Journal of Nuclear Science and Technology* (1997) 34 (3), 256
5. Ukai, S.*, et al.*, *Journal of Nuclear Materials* (1993) 204 (0), 65
6. Ukai, S., and Fujiwara, M., *Journal of Nuclear Materials* (2002) 307–311, Part 1 (0), 749
7. Odette, G. R.*, et al.*, *Annual Review of Materials Research* (2008) 38 (1), 471
8. Odette, G. R., *Scripta Materialia* (2017)
9. de Carlan, Y.*, et al.*, *Journal of Nuclear Materials* (2009) 386–388, 430
10. Baldev Raj, V. M., Ferritic Steels and Advanced Ferritic - Martensitic Steels. In *Comprehensive Nuclear Materials*, Elsevier Science, Amsterdam, (2012), p 105
11. Klueh, R. L., *Transactions of the Indian Institute of Metals* (2009) 62 (2), 81
12. Murty, K. L., and Charit, I., *Journal of Nuclear Materials* (2008) 383 (1–2), 189

13. Krautwasser, P., *et al.*, *High Temperatures. High Pressures* (1994) 26 (5), 549

14. Sundararajan, G., *et al.*, *Current Science* (2013) 105 (8), 1100

15. Allen, T. R., *et al.*, *Journal of Nuclear Materials* (2008) 375 (1), 26

16. Dasgupta, A., *et al.*, Electron Microscopy Studies on Oxide Dispersion Strengthened Steels. In *Materials Challenges and Testing for Supply of Energy and Resources*, Springer Berlin Heidelberg, Berlin, Heidelberg, (2012), pp 117

17. Ukai, S., *et al.*, *Materials Science and Engineering: A* (2009) 510–511, 115

18. Ohtsuka, S., *et al.*, *Journal of Nuclear Materials* (2004) 329–333, Part A, 372

19. Kimura, A., *et al.*, *Journal of Nuclear Materials* (2011) 417 (1–3), 176

20. Dou, P., *et al.*, *Journal of Nuclear Materials* (2013) 442 (1–3, Supplement 1), S95

21. Klueh, R. L., *et al.*, *Journal of Nuclear Materials* (2005) 341 (2–3), 103

22. Susila, P., *et al.*, *Journal of Materials Science* (2010) 45 (17), 4858

23. Pasebani, S., *et al.*, *Acta Materialia* (2013) 61 (15), 5605

24. Hoffmann, J., *et al.*, *Journal of Nuclear Materials* (2013) 442 (1–3), 444

# LIST OF FIGURES

## LIST OF TABLES

# LIST OF ABBREVIATIONS

| | |
|---|---|
| PHWR | Pressurized Heavy Water Reactor |
| FBR | Fast Breeder Reactor |
| dpa | displacements per atom |
| ODS | Oxide Dispersion Strengthening |
| DBTT | Ductile to Brittle Transition Temperature |
| MA | Mechanical Alloying |
| BPR | Ball-to-Powder weight Ratio |
| HIP | Hot Isostatic Pressing |
| HE | Hot Extrusion |
| SPS | Spark Plasma Sintering |
| $T_m$ | Melting Temperature |
| XRD | X-Ray Dffraction |
| FIB | Focused Ion Beam |
| SEM | Scanning Electron Microscopy |
| TEM | Transmission Electron Microscopy |
| EDS | Energy Dispersive Spectroscopy |
| DSC | Differential Scanning Calorimetry |
| EBSD | Electron Back Scattered Diffraction |
| RPM | Revolutions Per Minute |
| ROI | Region Of Interest |
| GIS | Gas Injection System |
| FEG | Field Emission Gun |
| SE | Secondary electron |
| BSE | Backscattered Electron |
| CCD | Charge Coupled Device |
| SAED | Selected Area Electron Diffraction |
| ICDD | International Centre for Diffraction Data |
| BF | Bright Field |
| DF | Dark Field |
| HRTEM | High Resolution Transmission Electron Microscopy |
| ASTM | American Society for Testing and Materials |
| nc | nanocrystalline |
| SPD | Severe Plastic Deformation |
| FWHM | Full Width at Half Maximum |
| bcc | body centered cubic |
| W-H | Williamson Hall |
| KJMA | Kolmogorov-Johnson-Mehl-Avrami |
| N&T | Normalizing and Tempering |
| KAM | Kernel Average Misorientation |
| IPF | Inverse Pole Figure |

Chapter I

# Introduction

## 1.1 Objectives and strategies for energy production

The sustainable development of a country largely depends on the energy resources it possesses. India, being a country with an estimated population of about 1.3 billion, is slowly but steadily advancing towards rapid growth in economy and sustaining this growth, greatly depends on the efficient supply of energy. Apart from support to its expanding economy, this energy is required to fulfill the growth ambitions of a country in which majority of the population are youth. This ambitious younger generation is driving the aspiration of the country for new technology and innovation, leading to better quality of life. The successful realization of these aspirations demands sustainable energy. In fact this demand, though more specific to a fast growing economy as India, is also a worldwide challenge [1]. It can be met only with judicious choice of energy resources, such as an efficient utilization of conventional energy resources together with development of all sectors of alternate energy resources. This has to be done with a careful study on all issues related to sustainability including abundance of available energy resources, diversity of sources of energy supply and technologies, self-sufficiency, security of energy infrastructure, effect on local, regional and global environment and health externalities [2-4].

Renewable energy options such as solar, wind etc. is known to provide clean energy but their technology is still evolving [5, 6], as efficiencies are still much below their anticipated limits. In this scenario, the nuclear energy is one of the viable options for the production of electricity with existing technologies, huge operation experience and most importantly it has possibly one of the least carbon footprints [7].

Environmental awareness related to climatic changes, increased reliability, improved safety culture and the necessity for sustainable energy are some of the reasons for the renaissance of nuclear power in the recent times [8]. Specifically to India, deploying the nuclear energy programme is of great importance, as India has rich reserves of thorium, constituting ~ 30% of the world's total reserves [9, 10]. The effective utilization of this thorium reserves can make India energy independent, but this involves closing the nuclear fuel cycle with three stages of nuclear programme. The first stage involves using the indigenous uranium in PHWRs, which, along with production of energy, also produces fissile plutonium (Pu – 239). In the second stage, by reprocessing the spent nuclear fuel and using the recovered plutonium in FBRs, the non-fissile depleted uranium and thorium can breed additional fissile nuclear fuel, namely, plutonium and uranium-233. In the third stage, thorium and uranium-233 based nuclear reactors can meet India's long-term energy requirements [8, 11-16]. Thus India's nuclear energy programme involving a closed fuel cycle technology is of great importance to the development of energy sector of the nation.

As explained above, it is acknowledged that fast reactors in stage II of the Indian nuclear program shall play an eminent role. It is to be noted here that, the large scale exploitation of fast reactors shall meet requirements such as, economic competitiveness, safe and optimized waste management, increased proliferation resistance, improved use of uranium and thorium and enhanced efficiency [8, 17]. It is known that fast reactors pose a serious challenge to materials scientists, as it employs high flux of neutrons, uses liquid metal coolant and operates at high temperature [18]. Thus addressing the material issues is one of the major challenges of Indian nuclear programme.

## 1.2 Selection of nuclear structural materials – General criteria

Selection of materials for fast reactor applications is vital in maintaining a controlled self-sustainable reactor operation. Nuclear materials can be classified into two major categories: in-core and out-of-core component materials based on their site of application [8]. Advanced nuclear reactor systems like fast rectors need to be operated at temperatures up to 973 K in an intense neutron radiation environment of the order of $10^{15}$ ncm$^{-2}$s$^{-1}$[19]. In-core materials thus need to survive these harsh environments. One such critical component is the fuel clad tube, which is a thin walled cylindrical tube housing the fuel pellets. Due to the presence of fission products, the high energy radiation interact with clad material producing large concentration of point defects, leading to void swelling and dimensional changes to the material, which in turn can lead to catastrophic effects such as ‘bowing’. Consequently, the clad tubes need to be retracted from the core, well in time, which still has unspent fuel in it. This is a major issue of concern, because the unspent fuel has to be further re-processed to separate it from the clad material which also hampers the economic operation of a reactor. The development of material with superior high temperature mechanical properties and irradiation resistance (upto ~ 200 dpa) has thus gained prominence.

General requirement for a fast reactor core structural material are dimensional stability under irradiation, low fast neutron absorption cross section, high-temperature mechanical properties (tensile strength, ductility, creep resistance, fracture toughness etc), chemical compatibility with the fuel and coolant, and fabricability [8, 20-22]. These requirements narrow down the choice of materials to be used in the reactor environment. Austenitic stainless steel and nickel based alloy could be candidate materials for reactor core components. But, nickel based alloys undergo (n, α) reaction and thus have high tendency for helium embrittlement which causes decrease in ductility. Austenitic stainless steel is by far the most preferred material. But swelling in these materials at doses higher than 50dpa is rather concerning, which led to the research and development on improvised steel, with varying Ni and Cr content [23, 24].

On the other hand, in comparison to austenitic steels, ferritic steels have superior thermal conductivity, low thermal expansion coefficient, good compatibility with liquid metal coolant, void swelling resistance and embrittlement resistance even at displacement dose above 150dpa. Figure 1.1 (a) shows the superiority of the ferritic steels in terms of its void swelling resistance in compassion to austenitic steels. A JMatPro prediction in figure 1.1 (b) shows the superior thermal conductivity of ferritic steels. However, a major concern of ferritic steel is their relatively low creep resistance as shown in figure 1.1 (c), from JMatPro calculations. A comparison of some of typical materials properties for austenitic and ferritic steels is given in Table 1.1.

As explained earlier, the poor high temperature creep properties of ferritic steels limit their application and need to be addressed. This issue can be overcome with the dispersion of nano sized ceramic particles into the ferritic or ferritic–martensitic matrix. Because of their high hardness, high temperature stability, inertness and insolubility in the metal matrix and also owing to their ability to be dispersed uniformly in fine particulate form, the most preferred dispersoids are oxides [25], in particular $Y_2O_3$ [26] and these materials are widely known as ODS alloys. This class of steel need to be powder metallurgically processed and is one of the most promising emerging structural materials for high temperature structural application. The current state-of-the-art of this very important material will be reviewed in the subsequent sections.

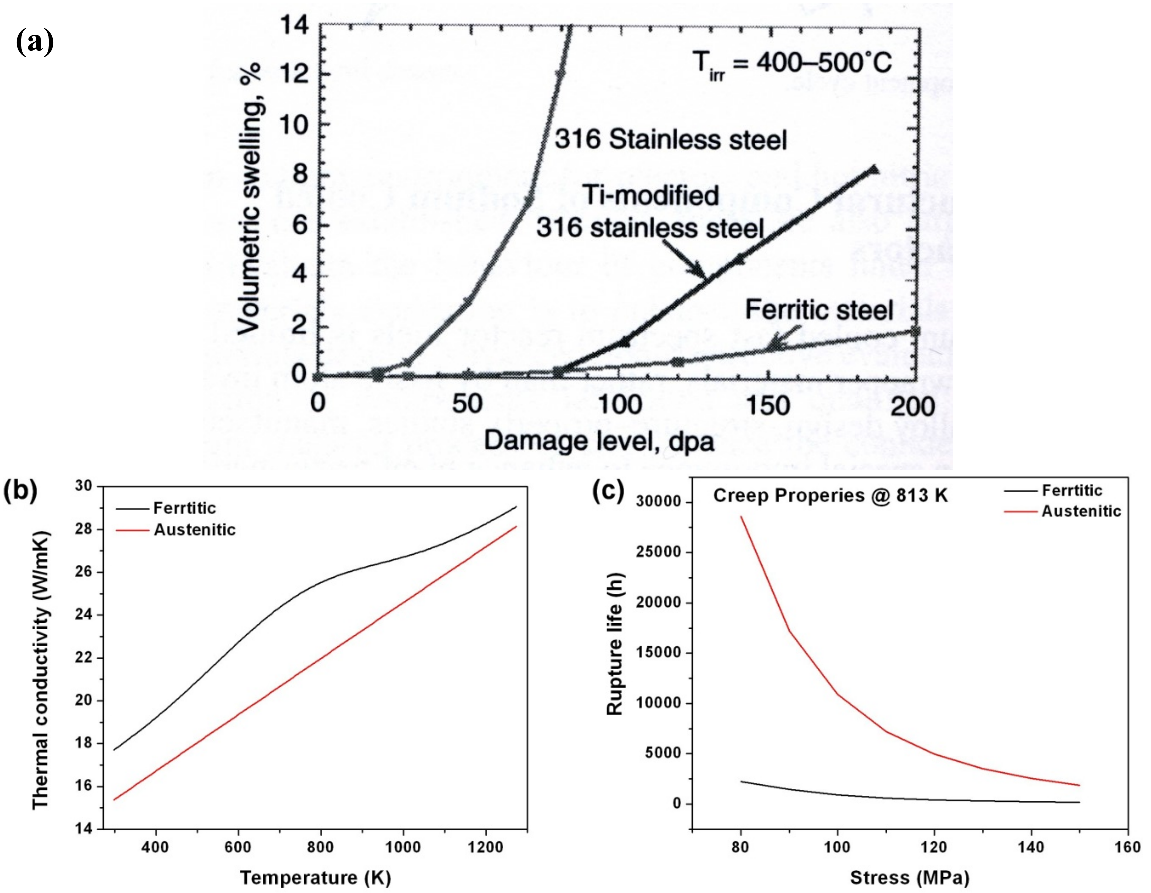

**Figure 1.1: (a) Comparison of swelling resistance of ferritic and austenitic steels [27]. (b) Variation of thermal conductivity with temperature for ferritic and austenitic steels. (c) Variation of creep rupture life with applied stress for ferritic and austenitic steels.**

**Table 1.1 : Comparison of some of the typical properties of Austenitic and Ferritic steels**

| Sl. No | Property | Condition | Value | | Ref. |
|---|---|---|---|---|---|
| | | | Ferritic | Austenitic | |
| 1 | Thermal conductivity | @900 K | ~ 26 W/mK | ~ 22 W/mK | [28] |
| 2 | Thermal expansion coefficient | @900 K | ~ 0.75% | ~ 1.2% | |
| 3 | Void swelling resistance | Irradiation @673-723 K, 180 dpa | Volumetric swelling < 2% | Volumetric swelling ~ 8% | [27] |

## 1.3 Oxide Dispersion Strengthened alloys

As discussed in the previous sections, development of materials with superior mechanical properties under extreme environments such as high temperature and irradiation is critical to the success of achieving higher dpa in fast reactors. ODS alloys have emerged as a new class of materials bestowed with these properties. The superior high temperature mechanical properties in these materials are derived from uniformly dispersed nanometer sized oxides, which act as barriers to dislocation motion at high temperature, increasing the creep resistance and in turn increasing the effective operating temperature [21, 26, 29-40].

Historically, much of the development in oxide dispersion strengthening is dedicated to improve the high temperature creep resistance of nickel and iron based super alloys by introducing a dispersion of stable oxide particles into a metal alloy matrix [41, 42]. Interestingly, the concept of adding inert particles to metals to improve their elevated temperature mechanical properties was first explored by W. D. Coolidge in thoriated tungsten as early as in 1910 [43]. It was soon discovered that, such additions help in increasing the creep properties of the material which led to significant scientific and technological interest in this field. These materials were mainly designed for sag resistance, requiring the strength to support their own weight for very long times at high temperatures. In a first dispersion strengthened material designed for load bearing application, a dispersion of aluminum oxide flakes in aluminum has been reported as sintered aluminum powder and reported by Irmann in 1949 [44]. It was observed that, the strength of this material increased with increasing volume fraction of the oxide and with decreasing inter-particle spacing. However, it was soon discovered that low melting point of aluminum was a limitation for its use at elevated temperatures which led to attempts of dispersion strengthening in higher melting point materials such as alloys based on Co and Ni [45]. The advent and development of mechanical alloying technique during 1960 -1970 further accelerated the research on dispersion strengthened materials and lead to the development of materials, such as Co [46-49], Fe [26, 32, 50], Cu [51-53], Al and Ni based ODS [45, 54-56] alloys. Some of the major domains of applications of ODS alloys are listed in Table 1.2 [57].

**Table 1.2: Application domains for ODS alloys [57]**

| Alloy base | Industry | Application |
|---|---|---|
| Fe | Aerospace / Military | Gas turbine combustion lines |
| | | Fuel nozzle shrouds |
| | Automotive | Diesel fuel inlet atomizer |
| | | Turbocharger scrolls |
| | Power generation | Burner nozzles, swirlers |
| | | High temperature heat exchangers |
| | | Core structural materials like clad tubes |
| Ni | Aerospace / Military | Turbine, compressor blades |
| | Automotive | Recombustors |
| | Power generation | Gas turbine combustion blades |
| Al | Aerospace / Military | Low density aerospace forgings |
| | | Compressor vanes, torpedo hulls |
| | Automotive | Composite pistons, compressor rotors, vanes, impellors |

### 1.3.1 Oxide Dispersion Strengthened steels for nuclear applications

The first mention of a ODS steel dates back to 1967 [58, 59], when J. J. Huet reported a stable oxide dispersion in a 12Cr ferritic steel using oxides such as $Al_2O_3$, MgO, $ZrO_2$, $TiO_2$ and $ZrSiO_4$. However, the interests in ODS ferritics have gained momentum since 1985 [32, 60] and the research in ODS steels has been in continuous growth since then. ODS steels find applications in nuclear fission and fusion reactors and in ultra super critical steam turbines [26, 32, 34, 37, 38, 40, 61], owing to their superiority over other materials. They are candidate core structural materials for both fast fission as well as fusion reactors and derive their superior irradiation performance from the fine and uniform dispersoids in the ferrite matrix [39]. For application as core structural material, the materials needs to have stability up to 973 K over prolonged duration and so as to yield fuel burn up of about ~200 $GWdt^{-1}$. Additionally, neutron flux to which the core materials are subjected to, is of the order of $10^{19}$ $nm^{-2}s^{-1}$ [62], and hence they should be designed to resist void swelling and irradiation creep [63]. The ferritic ODS alloys have gained prominence over their austenite counterparts because of their low activation and reduced void swelling [40]. This is due to the relatively open bcc structure, which results in rapid atomic transport by diffusion and consequently recombination rates of vacancy interstitial pairs are very high [12, 19, 64]. Introducing uniformly distributed oxides in these alloys provides simultaneous improvements in creep strength and radiation damage resistance, as these dispersoids act as obstacles to dislocation motion and also play a role as point defect recombination centers for radiation induced point defects thus avoiding void swelling. The superiority of ODS ferritic steels over conventional ferrtic-martenstic steels and austenitic steels is schematically shown in figure 1.2.

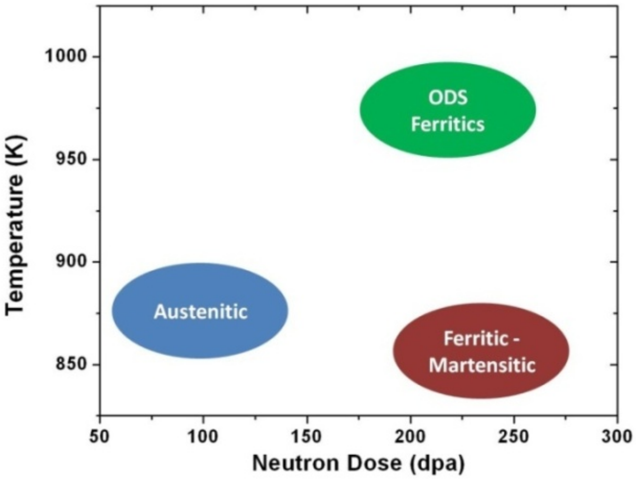

**Figure 1.2: Schematic of operating temperatures and irradiation doses for ferritic-martensitic, Austenitic and ODS ferritic steels [65]**

Further, the 9Cr variant of ODS steels have advantages over the high Cr variant because of their ferritic–martensitic structure. Though it is true that, to maintain high corrosion resistance ~13 - 18 Wt. % Cr is required, a lower Cr concentration, such as 9Cr ODS, allows for an improved resistance to high temperature mechanical property degradation and void swelling. Also, the martensitic microstructure of the steel is usually isotropic with a low DBTT [66]. High Cr steels lead to thermal embrittlement due to the formation of α’- phase at temperatures between 673 K and 823 K, which is detrimental. Additionally, tungsten is added to this alloy which is a low activation element and also responsible for solution hardening. However addition beyond 2 Wt. % leads to precipitation of laves phases which may cause concern with irradiation/thermal embrittlement [40]. In view of this, the 9 - 12Cr ODS steels are candidate materials which are being developed for nuclear applications [26, 39, 67, 68]. The figure 1.3 shows the comparison of 9Cr ODS in comparison with other variants. Figure 1.3(a) shows superior tensile strength of 9Cr ODS in comparison to conventional ferritic steel

[69], whereas, figure 1.3(b) shows the superior creep rupture properties of 9Cr ODS in comparison to conventional ferritic–martensitic and austenitic steel. It can be inferred that, the improved creep rupture strength is far beyond that of conventional ferritic–martensitic steel and superior to austenitic steel beyond 1000 h at 1023 K [26].

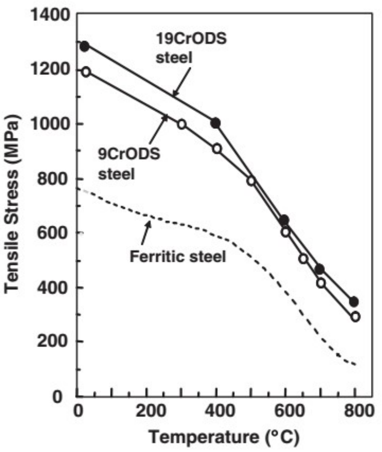

**Figure 1.3(a) :The dependence of tensile stress on test temperature in ferritic steel, 9Cr-ODS steel and 19Cr-ODS steel [69]**

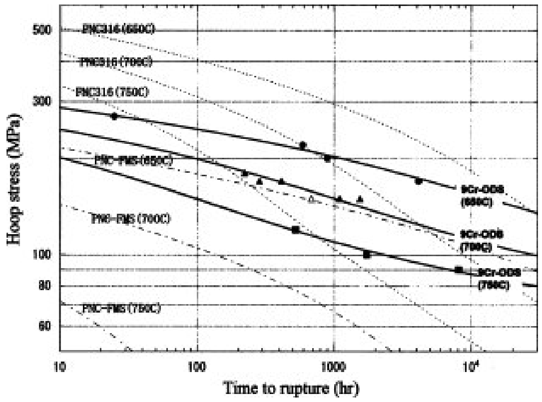

**Figure 1.3(b): Creep rupture properties of manufactured martensitic 9Cr-ODS steel cladding, comparing with those of conventional ferritic steel and austenitic steel [26].**

### 1.4 Synthesis of Oxide Dispersion Strengthened alloys

The major challenge in developing the dispersion strengthened alloy is to produce a material with uniform dispersion of fine refractory oxides [70] such that they have a minimum inter-particle spacing between them [71, 72]. Conventional casting route cannot be used because of the density differences between the matrix (heavier) and the refractory oxides (lighter), which leads to the separation of matrix and dispersoid phase during cooling due to buoyancy [73]. The tendency for agglomeration by nano-oxides before introduction and in the melt is also a cause for concern here. Further, it is also true that, the refractory oxides generally remain unwetted in a molten matrix and as a result there are difficulties in penetrating the oxide skin. In addition to these, the practical difficulties and possible health and safety issues in dealing with considerable volumes of nano-particles in the foundry environment also limits the melting route for synthesis of ODS alloys [73].

Historically, several methods have been adopted for synthesis of dispersion strengthened alloys [42]. For simple metal – dispersoid systems, the synthesis routes such as simple mixing [74], ignition surface coating [75], internal oxidation [76] and selective reduction [77] were found to be successful [42]. But these methods failed to be applied in alloy systems, mainly owing to the reactive nature of the alloying elements. Mixing technique resulted in the oxidation of fine titanium and aluminum powders, because of their high specific surface area. In case of ignition surface coating technique, matrix alloy powder is mixed with a liquid solution of a salt of a reactive metal. The salt is then converted to refractory oxide by heating the powder in an inert or reducing atmosphere which then produces powders with oxide coating. Powder contamination is a major issue here because of the presence of reaction products in the salt decomposition step. The internal oxidation technique involves oxidation of the alloy powder in an oxidizing atmosphere at elevated temperatures. The reactive element is then converted to a dispersoid by diffusing oxygen. It has been found that the dispersoid size increases with increasing depth of penetration of the internal oxidation into metal. Thus, to have fine dispersions, the initial powders need to be refined. Further, in case of super alloys, where γ' precipitates also play a role, the oxygen potential could not be raised above the extremely low values required to oxidize the γ' forming elements and the oxidation rate of the desired dispersoid forming elements would be slow. Selective reduction is another method which was used for the synthesis of dispersion strengthened materials, where, an intimate mixture of metal oxides is produced (both that of matrix and dispersoid) and oxides of the matrix is selectively reduced. It leaves the dispersoid unaffected, leading to oxide dispersoids in a metal matrix and hence strengthening is achieved. But with Al and Ti in the matrix, reduction was not possible with gases due to the stability of $Al_2O_3$ and $TiO_2$. Use of molten alkali and alkaline earth metals thus becomes essential but resulted products such as reaction salt, which needs to be removed. The excessive growth of dispersoid was also noticed.

The synthesis route for ODS alloys is an evolving domain in itself, with much of the interest is in developing cost effective methods aimed for bulk synthesis of materials [73, 78-81]. Novel methods such as vacuum casting [82], laser additive manufacturing [80] and selective laser melting [83] are gaining interest in the recent past, although their technology has not matured yet. The well - established and widely used technique for synthesis of ODS alloys is MA, which is discussed below.

### 1.4.1 Oxide Dispersion Strengthened powders by Mechanical Alloying

The advent of MA is majorly due to the desperation of researchers to find a suitable method for synthesis of dispersion strengthened alloys with the limitations of the existing methods as explained earlier. Historically, the concept of ball milling was known with the synthesis of tungsten carbide dispersed cobalt [84] and it was also known, that, heavy plastic deformation can fracture the powder particles. The MA technique was invented by John S. Benjamin and his colleagues in 1966 with the development of high energy ball mills [85]. The idea here was to refine the microstructure of a material by a constant interplay between welding and fracturing of the powder particles to arrive at an internal structure, but having an overall particle size, which was relatively coarse and therefore stable. Specific to the ODS alloys, MA makes possible, the combination of dispersion, solid solution and precipitation strengthening by mixing all the constituents in powder form to produce an intimate mixture of alloy powder with oxides dispersed in the solid solution [86]. It is to be mentioned here that, when pre-alloyed powder is utilized for synthesis instead of elemental powder, there is no alloying but only milling and consequently, the process is called as Mechanical Milling [85].

Over the years, MA technique has been employed in the production of a variety of commercially useful and scientifically interesting materials. These materials mainly fall into three different categories of metals and alloys, namely: (1) ductile-ductile, (2) ductile-brittle and (3) brittle-brittle. It is to be noted that, the mechanism of these processes is also well documented in literature [85, 87-92]. Synthesis of ODS alloys by MA fall in the category of ductile-brittle component, because here, the brittle oxide particles are dispersed in a ductile matrix. The mechanism with which the powder morphology varies during MA depends on the nature of initial powder particle. For a ductile starting material, the powder particles trapped between the grinding balls form flattened layers, where, the nascent atomically clean overlapping surfaces overlap and form cold welds, on the other hand the work hardened regions will fracture. The competing events of cold welding and fracturing continue repeatedly throughout the milling period, eventually forming a refined and homogenized microstructure [85]. The different stages of processing of ODS alloys are schematically shown in figure 1.4.

In the early stages of processing the metal powder particles gets flattened and forms layered composites with a large lamellar spacing. The sizes of these composite particles vary over a large range and their chemistry also varies significantly from particle to particle. At this stage, some unwelded starting metal powder particles also may still exist. The dispersoids are closely spaced along the lamellar boundaries.

At the Intermediate Stage of Processing, the cold welding and fracturing events continue to take place leading to further microstructural refinement. The particles evolve here with convoluted lamellar structure. Owing to the increased amount of cold working, a large number of crystal defects are introduced and these provide short-circuit diffusion paths, which is further facilitated with a rise in the powder temperature. This results in alloy formations with stable or metastable phases. The oxide dispersion becomes more uniform and finer.

At the final stage of processing, the lamellae become finer and more convoluted with the chemistry of individual powder particles approaching that of the overall composition of the starting powder. The finer lamellar and dispersoid spacing is characteristic of this stage. Further processing will not improve the distribution of the dispersoid, and a steady state is reached.

The structure that develops during high energy ball milling depends on the nature of powder particles and on the process variables. It is important to optimize these process variables to achieve the desired microstructure and properties. For a given composition of the powder, the important variable which has an effect on the final constitution of the milled powder includes milling medium, milling energy/speed, milling duration, BPR and temperature of milling.

| | |
|---|---|
| **Early stage:** | 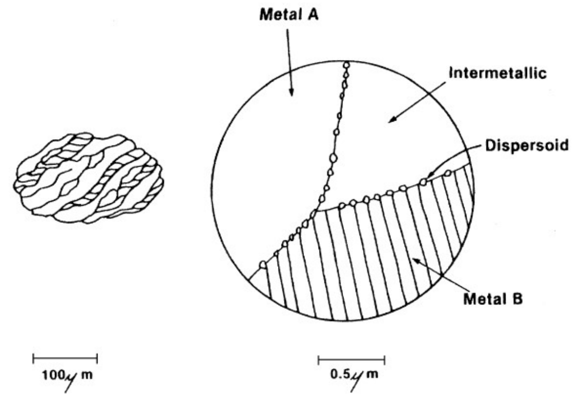 |
| **Intermediatestage:** | 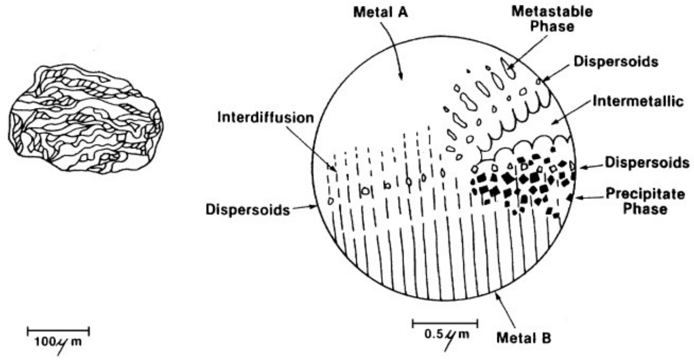 |
| **Final stage:** | 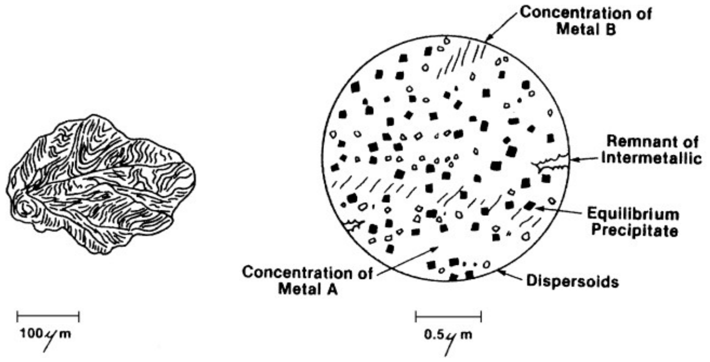 |

**Figure 1.4: Schematic representation of stages during MA for ODS alloys[85]**

It should be noted here that, some of these process variables are dependent on each other and hence the optimization of milling conditions should be carried out on a case to case basis. For e.g. the optimal milling duration depends on the BPR ratio because increased BPR imparts more energy to the powder particle per collision, consequently resulting in lower optimal milling duration.The optimized milling duration is chosen based on achievement of a steady state between fracturing and coldwelding of powder particles to facilitate alloying. In addition to BPR, the optimal milling time also depend on the type of mill used, intensity of milling and temperature of milling, which tells us that, the optimal times have to be decided for each combination of the above parameters and for the particular powder system under consideration.

### 1.4.2 Consolidation of Oxide Dispersion Strengthened powders

The ODS powder synthesized through MA needs to be compacted in order to produce an engineering component out of it. The general rationale here is to obtain a dense product without losing the strengthening achieved through ball milling. There are several ways this can be achieved, such as the HIP, HE and SPS, all of which employ simultaneous application of high pressure with high temperature to achieve density. HE is known to produce highly dense ODS alloys components but it is also known to render a material anisotropic in nature with texturing and elongated grains. Owing to this, the extruded tubes typically known to have half the creep strength in the hoop compared with the axial extrusion direction.The milled powders can also be consolidated by HIP after degassing and vacuum sealing in a stainless-steel container in vacuum. A process of HIP in general is taken up by applying an Ar pressure typically ~ 200 MPa for about 2-4h at temperatures ~ 1423 K [93]. Generally, HIP yields a more isotropic microstructure and a lower ductility and fracture toughness compared to HE. The SPS technique has been explored as an alternative route for consolidation, which has the advantage of high thermo-efficiency as well as the fast heating-up of the sample to high temperature which avoids grain growth or nano-precipitate coarsening. Fine microstructure is reported for SPS synthesized ODS materials, with fine microstructure and nano dispersion strengthening. The schematic of ODS alloy synthesis starting from powder up to consolidation and thermo-mechanical treatments is given below in figure 1.5.

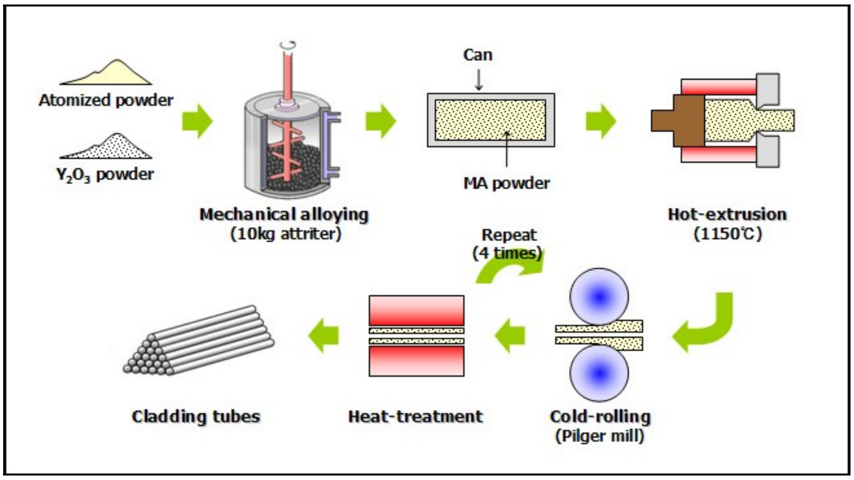

Figure 1.5: Schematic of ODS alloy synthesis

## 1.5 Strengthening mechanism in Oxide Dispersion Strengthened alloys

Strength of a material refers to its ability to withstand an applied load without failure or plastic deformation. In a wider perspective, the mechanical properties of a material, such as, tensile strength, creep etc, are the measure of strength of a material. It needs to be mentioned here that, the mechanical properties of a material is also a function of temperature, stress etc. This is due to the fact that, dislocations in a material are the carriers of plasticity and the ability of a metal to deform plastically depends on the ability of dislocations to move, which in turn, depends on temperature and stress [94].

Strengthening in ODS alloys is achieved through dispersoids, as, these oxides are known to act as barriers to dislocation motion. Strengthening here can be described by various mechanism with which the dislocation – dispersoids interact. In addition to the direct strengthening by dispersoids, the other strengthening mechanisms in ODS alloys are also known to be affected by dispersoids or through the MA process, this includes, Hall–Petch strengthening, dislocation forest hardening and matrix strengthening.

The Hall–Petch strengthening results due to barriers for dislocation motion through grain boundaries, which increases with the decrease in grain size [95, 96]. This is a chief strengthening mechanism in nanocrystalline materials for obvious reasons. It is observed that incoherent oxide particles can refine the grain size of an alloy during processing, through pinning of the grain boundaries. It is also true that, the oxides exert retarding force on the migrating grain boundaries, resulting in their high temperature stability. The retarding force per unit area, $F_r$, is given by [97],

$$F_r = \frac{3f\gamma_{gb}}{2r} \tag{1.1}$$

Where, $f$ is the volume fraction of dispersoid with radius $r$ and grain boundary energy $\gamma_{gb}$. It can be noted from the above equation that, for a given volume fraction of dispersoids, smaller dispersoids offer greater hindrance compared to larger ones.

Since ODS alloys are synthesized by MA, these materials are associated with high dislocation densities. Now, dislocation forest strengthening arises from dislocation - dislocation interaction and since dislocations repel each other there is an energy associated with their interaction. This strengthening is known to contribute significantly to the high temperature strength in ODS alloys.

Matrix strengthening modifies dislocation mobility by precipitation hardening or solution hardening. These mechanisms also modify the Peierls-Nabarro stress which is the lattice friction. Precipitation hardening results from formation of coherent phases in the crystal lattice, which strains the matrix thus contributing to strengthening specially at low temperatures.

The direct strengthening of alloys by dispersoids results from obstacle for dislocations by dispersoids as they move through the lattice. The impenetrable dislocations can move through a dispersoid only by changing their curvature sharply whereas, in case of coherent particles the dislocations can pass through at very high stress levels [94]. The dislocations can overcome the dispersoids through (i) Orowan bowing (ii) cross slip and (iii) climb. Bowing and cross slip of dislocations generally occur at temperatures < 0.5 $T_m$. When a dislocation encounters dispersoids in its glide plane, they inhibit the passage of dislocations by blocking them through pinning, mechanism of which is shown schematically in figure 1.6 below. The blocked dislocations had to bow between the dispersoids resulting in the initial Orowan yield stress. This yield stress $\tau$ is decided by the stress required for a dislocation line to pass by the dispersoids and is given by,

$$\tau = \frac{Gb}{\lambda} \tag{1.2}$$

Where, $\lambda$ is the distance between the dispersoids, G is the shear modulus of the matrix and b is the burgers vector. As the applied stress is increased, the dislocation line is bowed around the two particles until the dislocation line reaches a critical curvature, after which the dislocation line can move forward without increasing its curvature. The segments of dislocation line on either side of each dispersoid then join, and a dislocation loop is created around the dispersoid. Further, these loops would exert a back stress on the slip plane raising the level of applied stress needed to continue further slip. The accumulation of loops about the dispersoids will continue until a limiting stress in or about the particles were reached after which the number of trapped loops remain at that saturation level. The resultant saturation back stress was identified as the maximum hardening increment. When the dislocations are not confined to their slip planes during the bowing out process, cross slip may occur.

Now, at high temperatures, where the diffusion is high, the dislocations overcome dispersoids, by an out of plane motion of the dislocation loop, known as climb. This is highly relevant to creep, which is a thermally activated diffusion process where edge dislocations exhibit climb, or motion out of the slip plane. Since dispersoids cannot be sheared unlike precipitates, the dislocations need to climb around the dispersoids at high temperature. Although, there is an availability of thermal energy at high temperatures, it is still higher than, if the dispersoids were not there. Consequently, the dislocation propagation is retarded and resulting in exceptional creep resistance in ODS alloys at high temperatures [98]. Additionally, the dispersoids are thought to be beneficial above the equicohesive temperatures, wherein, the grain boundary sliding can be limited with finer dispersoids pinning the grain boundaries, thus contributing to creep resistance [99].

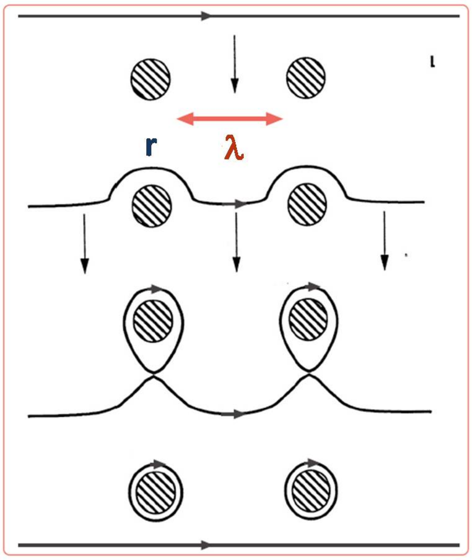

**Figure 2.6: Dislocation line Passing dispersoids [94]**

## 1.6 Criteria for selection of dispersoids for Dispersion Strengthening

Since dispersoids in ODS alloys are essentially responsible for their superior high temperature mechanical properties, selection of dispersoid type is of paramount importance. It is basic necessity of the dispersoids to be thermally stable at elevated temperatures and chemically inert and additionally, the attention should also be given on the interactions between dislocations and inert dispersoids, since they govern the creep resistance property and thermal stability. It is to be mentioned here that, the selection of dispersoid must be carried out based on the careful watch on the functional requirements of the alloy product. Specific to the ODS steels, as mentioned earlier, the emphasis is on the high temperature mechanical properties and its suitability to be used in a nuclear environment. Some of the important criteria which need to be considered in selecting the dispersoids for strengthening are discussed below.

### 1.6.1 High temperature thermodynamic stability

The typical operating temperature for fast reactors is ~ 973 K, which may go up to 1073 K during transients [73]. However, the expected processing temperatures for consolidation of alloy powders and subsequent thermo-mechanical treatments may go up to 1423 K. Similarly, the operating temperatures for high temperature turbine blades, heat exchangers will also fall in this temperature range. Therefore, the dispersoid is expected to be chemically and thermodynamically stable up to this temperature. Owing to their large negative heats of formation and high melting points, the oxides become primary candidates for dispersion strengthening. There exists reports of nitrides [80, 100] and carbides [101, 102] utilized for strengthening but oxides remain the widely used species for strengthening. The Ellingham diagram shown in figure 1.7, is an useful guide towards selection of dispersoids. This is because; the graph shows the thermal stability of various oxides and nitrides, as a function of temperature. The higher stability of oxides in comaparison to nitrides is to be noted [103]. The heat of formation energy of some of candidate oxide dispersoids are also listed in Table 1.3 [104].

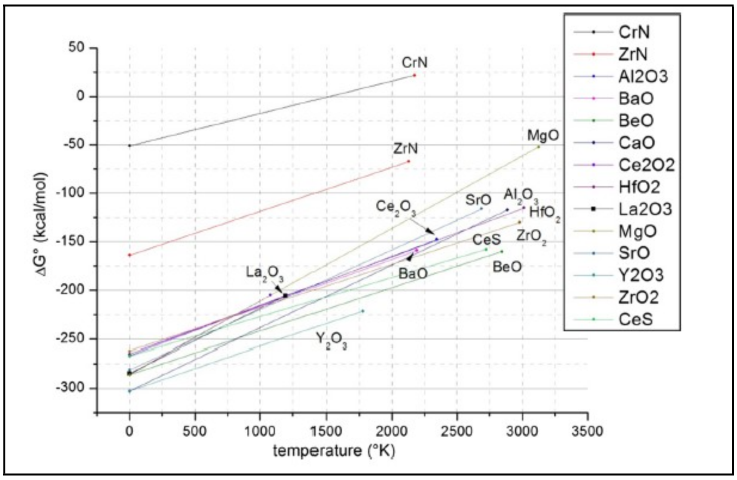

Figure 1.7: Gibbs-free-enthalpy of various oxides and nitrides [103]

**Table 1.3: Heat of formation of some important oxides at 300 K**

| Oxide | Heat of formation ($\Delta G$ in kJ $mol^{-1}$) |
|---|---|
| $Y_2O_3$ | -1816.65 |
| $ZrO_2$ | -1042.8 |
| MgO | -569.3 |
| $La_2O_3$ | -1705.8 |
| $CeO_2$ | -1024.7 |
| CaO | -603.3 |
| $ThO_2$ | -1169.2 |
| $TiO_2$ | -888.8 |
| $Al_2O_3$ | -1582.3 |
| $Cr_2O_3$ | -1058.1 |

### 1.6.2 Mechanical and thermal properties

The mechanical properties of dispersoids themselves is an important consideration in optimizing ODS alloy design [105]. The choice of ceramic particles as dispersoids has a basis due to the fact that, they possess high strength as reflected by their high hardness. As a result, the dispersoids are deformation resistant and cannot be sheared by dislocations. In addition to these, distinctive relationship between the dispersoid - matrix interface and dislocations are also known to play a role and are discussed in this section.

The Orowan bowing mechanism as explained in section 1.5, suggests that, the creep strength is determined by dispersoid diameter and volume fraction alone. However, the creep properties are stress sensitive and temperature dependent, which the Orowan theory failed to take into account. Modern theories proposes that, properties of dispersoid - matrix interface also play a role in governing creep properties of ODS alloys. They suggests at an attractive interaction between the dislocation and the dispersoid-matrix interface which leads to a detachment stress $\sigma_D$given by [97, 106],

$$\sigma_D = \sqrt{(1 - k^2)} * \sigma_{OR} \quad (1.3)$$

Where k is an interaction parameter and $\sigma_{OR}$ is the Orowan stress. The interaction parameter k describes the degree of relaxation of dislocation line energy at the dispersoid - matrix interface and is given by

$$k = E_p / E_m \quad (1.4)$$

where, $E_p$ and $E_m$ are the dislocation line energy at the dispersoid and in the matrix respectively. k = 1, when no relaxation takes place which is for fully coherent interface whereas, k= 0 when a strong attractive interaction occurs and the dislocation completely relaxes its energy i.e., for incoherent interfaces. When $0 < k < 1$, the dislocation segment has a reduced line energy at the interface and the dispersoid exerts an attractive force on the dislocation. The maximum creep resistance is thus obtained for the incoherent dispersoid matrix interface.

Another important dispersoid – matrix property which plays a critical role is the difference between their coefficients of thermal expansion. This is of significance for materials used in high heat flux environments which undergoes thermo - mechanical fatigue. When exposed to thermal cycling, the thermal mismatch strain $\varepsilon_{th}$ between the particle and matrix is related to the difference between the coefficients of thermal expansion $\Delta\alpha$ of the particle and the matrix by the expression,

$$\varepsilon_{th} = \Delta\alpha * \Delta T \quad (1.5)$$

Where, $\Delta T$ is the change in temperature. When these materials are cooled fast, the relaxation of these thermal strains is accomplished by dislocation generation at second-phase particles. Although the high dislocation density would be beneficial to the fatigue strength, it is known to affect the thermal conductivity of the matrix phase and additionally, the dislocations act as high diffusivity paths that enhance particle - coarsening processes. Therefore, to reduce the dislocation density in the matrix with fine dispersoids, it is necessary to minimize the thermal strains by minimizing $\Delta\alpha$. i.e., to choose a dispersoid - matrix combination with minimum thermal mismatch.

### 1.6.3 Stability against high temperature coarsening

An additional factor to be considered for selection of dispersoids is their resistance to coarsening at high temperature. The coarsening of oxide particles in ODS is a subject of serious interest as witnessed by a number of publications in this domain [107, 108]. This is of importance because, $Y_2O_3$, the most commonly used dispersoid in ODS alloys, is known to coarsen at high temperatures. Owing to the large milling intensity, it is known that $Y_2O_3$ amorphize [109, 110] during mechanical milling and rapidly recrystallize into large crystallites during consolidation. This leads to a large inter - particle separation, resulting in property degradation.

The coarsening of oxide particles at high temperatures takes place via Ostwald ripening [111, 112]. The driving force for coarsening comes from the decrease in total surface free energy and the process occurs by the growth of large particles at the expense of smaller ones which dissolve [113]. It is predicted that, at any stage during coarsening there is a critical particle radius $r^*$ in equilibrium with the mean matrix composition; particles with $r > r^*$ will grow and particles with $r < r^*$ will shrink. Elements of lower solubility are preferred in this regard, because they are known to show less tendency for coarsening and slower diffusion in the matrix in comparison to soluble ones [114].

## 1.7 Choice of $Y_2O_3$ for strengthening and note on alternate dispersoids

The choice of dispersoid for strengthening an alloy is limited due to the rather demanding characteristics of the dispersoid, as explained earlier. The widely used dispersoid for strengthening is $Y_2O_3$, with vast literature on various aspects of $Y_2O_3$ addition to alloys and its characteristics [46, 109, 110, 115, 116]. However, it is experimentally observed that, the $Y_2O_3$ dispersoids amorphize during extended duration of ball milling leading to Y and O dissociation. This is detrimental, as the Y and O will reprecipitate to produce large crystallizes during annealing. In a model Fe -15 Wt. % $Y_2O_3$ ODS alloy system, it is reported that, $Y_2O_3$ grows up to micron in sizes [109]. The addition of a small amount of Ti thus becomes essential, as it is known to aid in precipitation of fine Y-Ti-O complex oxides such as, $Y_2Ti_2O_7$ or $YTiO_3$. The sizes of these oxide particle are believed to be around 3 nm in ODS alloys [26]. The ODS alloys with Y-Ti-O complex oxides have gained larger attention with wide range of studies carried out on this system. The science of complex oxide formation in ODS is still an evolving field with studies ranging from ab-initio to extensive experimentation [117, 118].

An alternate method to achieve fine and stable dispersions would be to harness a material with a novel dispersoid which is structurally stable during milling, yet have the inertness of $Y_2O_3$. It is to be noted here that, the potentiality of alternate dispersoids in ODS steels is not extensively studied and superior properties in terms of dispersoid refinement mechanisms for one of them cannot be ruled out. Thus, the search for alternate dispersoids is incessant and interesting.

The majority of the literatures on alternate dispersoids were carried out during the initial days, when $Y_2O_3$-Ti combination was not established. However, a few reports from recent past have rejuvenated the interests in the alternate dispersoids. The key motivation for the search for alternate dispersoids in the recent past majorly comes from the fact that little is known on the role of other potential alternative rare earth oxides for dispersion strengthening. Pasebani et al [119, 120] have studied $La_2O_3$ dispersed ODS alloys considering that, Lanthanum has no solubility in Fe at all temperatures [121] and it has a very high affinity to oxygen to form La–O bond, which essentially will be helpful in resisting the Ostwald ripening and thermal stability, respectively. In line with their assumption, the authors were successful in developing a nano-structured ferritic steel with La-Cr-O enriched precipitates in it. The authors further studied the role of alloying elements such as Mo and Ti and reported La-Ti-Cr-O enriched particles in the matrix. The irradiation response of the alloy has also been studied and showed an increase in number density of nano-precipitates and hardening of the matrix with increased irradiation dose [122]. In a similar line with this, Hoffmann et al [123] have studied $Ce_2O_3$, $La_2O_3$, MgO and $ZrO_2$ as alternate dispersoids as they have sufficient thermal stability at the desired operating temperatures. The results of their analyses showed that, stable oxides other than $Y_2O_3$ are also able to form fine dispersoids in ferritic steels and is very promising in terms of material costs and the design of low activation-materials for fission and fusion applications. It is to be mentioned here that, in order to develop alternate dispersoids, extensive work needs to be carried out to determine the optimal processing conditions to obtain a uniform microstructure. A list of alternate dispersoids reported in literature is given in Table 1.4.

**Table 1.4:List of literatures on alternate dispersoids for dispersion strengthening**

| Sl. No. | Dispersoid used | References |
|---|---|---|
| 1. | MgO | [58, 123-125] |
| 2. | $Al_2O_3$ | [58, 126-129] |
| 3. | SiO | [126, 128] |
| 4. | $La_2O_3$ | [119, 120, 123, 130, 131] |
| 5. | $CeO_2$ | [123, 128, 131] |
| 6. | $ZrO_2$ | [123, 124, 126, 132-135] |
| 7. | $TiO_2$ | [58] |
| 8. | $Cr_2O_3$ | [128] |

### 1.7.1 Rationale behind choosing $ZrO_2$ as an alternate dispersoid

Having established the criteria for selection of dispersoids, this thesis examines the feasibility of using $ZrO_2$ as an alternate dispersoid for strengthening. The foremost criterion for a dispersoid, as discussed earlier is the thermal stability and $ZrO_2$ is bestowed with a superior thermal stability at elevated temperatures as revealed from the Ellingham diagram [Figure 1.6]. It is also true that ability of a dispersoid to interact with dislocation depends on free energy of formation [86] and accordingly, this value for $ZrO_2$ is reported to be ~ -920 kJ $mol^{-1}$ [103] at 1000 K. It may be noted that, this value is also in close comparison to ~ -1080 kJ $mol^{-1}$ of $Y_2O_3$, indicating comparable stabilities. Further, melting temperature of $ZrO_2$ is ~ 2988 K which indicates its high temperature stability. Relevant to the nuclear applications, it is to be noted that, Zr has a lower fast neutron absorption cross section signifying its nuclear friendly character [136].

Additionally, yttrium (Y) and zirconium (Zr) are expected to exhibit similar physical and chemical properties due to their positions in the periodic table [132]. The role of Zr stabilizing grain sizes of Fe at elevated temperatures has attracted attention recently based on both experiments [137-139] and modeling [140, 141]. It is known that, addition of solute atoms which segregate at grain boundaries can lower the grain-boundary energy and due to the fact that, Zr has a limited equilibrium solubility in Fe even up to temperatures of ~ 1573 K (less than 0.5 at.%) [137], it can help in grain size stabilization in Fe based alloys. It was shown that, the addition of Zr to Fe alloys resulted in relatively narrow nanocrystalline grain size distribution with an average grain size of 52 nm and no abnormal grain growth in a Fe – 4 at. % Zr alloy after annealing at 1186 K. This is exceptional because pure Fe would have a 12 μm grain size at this temperature. Also, Zr addition to ODS steel as a size refiner for $Y_2O_3$ [142-145] to improve its thermal stability and mechanical property is a field of gaining interest [132, 139]. Literature shows that Zr addition to $Y_2O_3$ based ODS alloys resulted in enhancement of its thermal stability [146] and mechanical properties by formation of fine Y-Zr-O precipitates [147, 148]. It was shown by first principle calculations that, $Y_2Zr_2O_7$ oxides are of higher stability than $Y_2Ti_2O_7$, which are chief strengtheners in conventional ODS [149]. The Zr addition in ODS has also shown superior radiation resistance owing to the superior sink characteristics of matrix – oxide interface.

In addition to it, Fe – $ZrO_2$ nanocomposite has attracted attention owing to its interesting magnetic properties such as enhanced coercivity and remanence [150]. Superior hardness value, compared to the base matrix is reported in a Fe-$ZrO_2$ composite [151] and improved strength and hardness in a nano $ZrO_2$ added Al composite is reported [152]. Further, there are also few recent reports on superior mechanical properties of $ZrO_2$ dispersed ODS [133, 153] and a study [132] examined addition of Zr to the steel powder to arrive at $ZrO_2$ dispersions in the matrix and reported that size distribution of $ZrO_2$ is comparable to that of Y-Ti-O complexes.

Another important factor which is postulated in this thesis in selecting $ZrO_2$ as a dispersoid is its fewer number of atoms per unit cell (structure: mP12) compared to $Y_2O_3$ (structure: cI80), schematics of which is shown in figure 1.8.

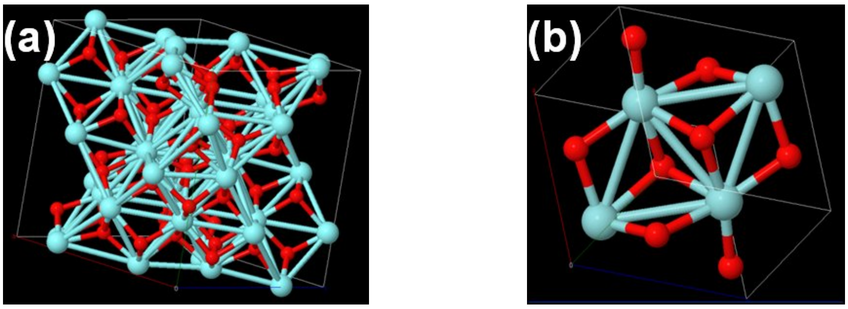

**$Y_2O_3$ : cI80**
**a = b = c = 10.6 Å**
**Volume = 1192.4 Å$^3$**

**$ZrO_2$ – mP12**
**a = 5.3 Å, b = 5.2 Å, c = 5.1 Å**
**Volume = 140.7 Å$^3$**

**Figure 1.8: Unit cell structure and lattice parameters of (a) $Y_2O_3$ (b) $ZrO_2$**

Owing to their large number of atoms in the unit cell, the unit cell volume of $Y_2O_3$ is much bigger in comparison to $ZrO_2$ as shown above. It is postulated that, the large number of unit cell atoms (80 in number) in $Y_2O_3$ may be playing a role in its structural instability leading to amorphization during mechanical milling. The literature suggest [154] that, during ball milling of $ZrO_2$ and $Y_2O_3$ mixture, $Y_2O_3$ amorphizes, whereas $ZrO_2$ does not. Although there is no concrete proof to correlate this result to number of atoms in unit cell, we may take hints from the irradiation induced amorphization in materials. It can be postulated irradiation as a form of mechanical damage by minute projectiles thus leading to disordering of atoms from their mean lattice positions. Complexity in structure is correlated to its amorphization behavior in case of a NiAl/PdAl thin films [155], where it was reported that, simple cubic structures with 2 or 4 number of atoms in unit cell survived under ion irradiation, whereas, complex structure became amorphous. A localized region is thought to be energized with penetration of highly energetic ion beam followed with quenching to the lattice temperature leading to amorphization. It is also said that, chemical disordering, departure from stoichiometry, point defect accumulation and lattice imperfections such as grain boundaries, dislocations and antiphase boundaries all plays a role in irradiation induced amorphization [156]. Since the high energy milling is also a non equilibrium process, it is logical to assume that, the science of irradiation induced amorphization holds for ball mill induced amorphization. Consequently, we predict a better amorphization resistance for $ZrO_2$ in comparison to $Y_2O_3$, thus, a superior dispersoid refinement mechanism.

## 1.8 Development of a model alloy system for understanding Oxide Dispersion Strengthening

The weight fraction of the dispersoid in an ODS alloy typically varies between ~ 0.2 - 1 Wt. % depending on the alloy composition. There is an upper limit on the amount of dispersoid that can be added to an alloy because larger dispersoid fraction in the material is known to adversely affect the ductility [50] and also the thermal conductivity of the material [97, 157]. A typical ferritic ODS steel, apart from the oxide dispersoid, mainly consists of Fe, Cr, W and other trace elements such as P, Mn, Si etc. This multi-elemental system makes this alloy relatively complex to characterize and there is a possibility that certain crucial information may be missed during the analysis. For example, as mentioned earlier, owing to the small weight fraction of dispersoid in ODS alloys, studying the evolution characteristics of dispersoid through XRD becomes difficult and hence understanding this information through a model system becomes essential.

An approach to overcome this issue is that to choose a model alloy of less complexity to mimic selected aspects of ODS steels. The short-term goal of studying the model systems is to gain an understanding on ODS alloys by analyzing its microstructure to arrive at definite conclusions about the properties intended to study and the long-term goal is to utilize this knowledge towards developing an actual alloy, which can be then characterized with better assurance [158]. There are extensive literature on model ODS alloy systems which include Fe-Cr, Fe-Cr-$Y_2O_3$, Fe-$Y_2O_3$, Fe-$Y_2O_3$-Ti etc. Some of the highlights from these studies are discussed below.

Since the existing research on ODS mainly concentrates on $Y_2O_3$ based dispersoids and owing to the lack of in-depth understanding on the dispersoid microstructure evolution with milling and annealing, the interests on concentrated $Y_2O_3$ in a Fe matrix is widespread. A model Fe - 25 Wt. % $Y_2O_3$ alloy has been studied by Tong Liu and co workers to understand the morphology change and structural evolution of $Y_2O_3$ during milling and subsequent annealing [110] and in an another effort, M. Brocq and co-workers have evaluated the milled and annealed behavior of $YFe_3$ and $Fe_2O_3$ powders to arrive at an understanding on reactive ball milling and subsequent annealing [159]. A series of work on model ODS alloys have also been carried out by Pradyumna and co workers [109, 160, 161] to understand the amorphization behavior of

$Y_2O_3$ during milling, influence of Ti on structural evolution of $Y_2O_3$ during milling and annealing. Further, strengthening mechanisms in mechanically milled oxide dispersed Iron powders have been studied by R. Vijay and coworkers with a thorough analysis of Fe, Fe-$Y_2O_3$ and Fe-$Y_2O_3$-Ti model alloys [162]. Similar to this, studies have been also carried out on Fe-Cr-$Y_2O_3$ systems also with an objective to understand the microstructure from preliminary stage [163, 164]. As a whole, the model ODS alloy systems have contributed substantially towards developing an understanding on some of the domains, which would not have been possible with an actual alloy. Some of the important literature reports on the model ODS alloy systems are listed in Table 1.5.

**Table 1.5: Some of the model ODS alloysystems studied in literature**

| Sl. No | Model alloy under study | Reference |
|---|---|---|
| **1.** | Fe - 15 Wt. % $Y_2O_3$ | [109] |
| **2.** | Fe -15 Wt. % $Y_2O_3$ - 5 Wt. % Ti | [160] |
| **3.** | Fe - 25 Wt.% $Y_2O_3$ | [110] |
| **4.** | Fe - 12 Cr<br>Fe - 12 Cr-0.4 Wt.% $Y_2O_3$ | [165] |
| **5.** | Fe - 9 Cr - 0.3/0.6 Wt.% $Y_2O_3$ | [158] |
| **6.** | Fe - 24 Wt.% Cr-15Wt.% $Y_2O_3$ | [163] |
| **7.** | Fe - 0.35 Wt.% $Y_2O_3$<br>Fe - 0.35 Wt.% $Y_2O_3$-0.2 Wt.% Ti | [162] |
| **8.** | Fe -14Cr - 0.25 wt.% $Y_2O_3$<br>Fe -14Cr | [166] |
| **9.** | Co-15 $Y_2O_3$ | [46] |
| **10.** | Fe - 9 Wt. % Cr-15 Wt.% $Y_2O_3$ | [115] |
| **11.** | Fe - 38 atm.% $Y_2O_3$ | [159] |
| **12.** | Fe - 0.3 $Y_2O_3$<br>Fe - 0.2Ti - 0.3 $Y_2O_3$<br>Fe - 14Cr–0.2Ti - 0.3$Y_2O_3$ | [167] |

## 1.9 Scope and Objectives of the Thesis

Although there are extensive research activities on $Y_2O_3$ – Ti dispersed ODS alloys [26, 31, 32, 34, 39, 40, 50, 67, 68, 168, 169], there is a dearth of literature on the potentiality of using other rare earth oxides as dispersoids in ODS materials. Some recent reports on exploring alternate dispersoids such as $La_2O_3$ [119], $CeO_2$, MgO and $ZrO_2$ [123] for ODS materials suggest superiority over $Y_2O_3$ and hence it is worth investigating them in detail to develop and establish it as a legitimate dispersoid. Thus, the current thesis focuses on investigating the possibility for an alternate oxide, namely $ZrO_2$, as dispersoid for strengthening the material.

Successful realization of alternative dispersoid ODS alloys would require a thorough understanding of the stability and microstructural evolution of the dispersoid during mechanical milling and subsequent stages involving exposure of the powder to high temperatures during consolidation and thermo mechanical treatments. Though alternate oxides have been tried to a little extent as reported in the literature, the focus was mainly on the final microstructure of the material and its mechanical properties, rather than on the dispersoid evolution during milling and annealing. Thus, in order to investigate suitability of an oxide as an effective dispersoid, in-depth studies concentrating on its structural evolution with milling and also at high temperatures is required. Further, in order to facilitate reliable characterization, it is necessary to choose a concentrated alloy with high dispersoid composition.

Keeping this in mind, the methodology applied in this study involves synthesis and detailed characterization of a model Fe - 15 Wt. % $ZrO_2$ system. The microstructure and microchemical evolution of this model system has been investigated as a function of milling duration to arrive at the optimized condition. Further the microstructural evolution of this model system with temperature is also been investigated. The knowledge accumulated on the behavior of dispersoids by these analyses were then utilized for developing a 9 Wt. % Cr ferritic steel. The behavior of as milled and annealed $ZrO_2$ dispersed steel powder has been evaluated and its consolidation properties using SPS technique has also been investigated.

### 1.10 Organization of the Thesis

This thesis, entitled **“Synthesis and characterization of $ZrO_2$ dispersion strengthened Fe based alloys”,**is organized into seven chapters as outlined below.

**Chapter I** provide a brief introduction to the ODS alloys emphasizing their mechanical properties and irradiation damage resistance. Criteria for selection of dispersoids for ODS alloy are discussed with a note on alternate oxides for dispersion strengthening. The choice of $ZrO_2$ as candidate dispersoid and rationale behind choosing the model alloy system for understanding ODS alloys is also been discussed.

**Chapter II** deals with the experimental techniques and procedures employed for the synthesis, characterization and evaluation of the structural, chemical and mechanical properties of Fe – 15 Wt. % $ZrO_2$ model system and $ZrO_2$ dispersed 9Cr steel.

**Chapter III** describes the synthesis and characterization of Fe - 15 Wt.% $ZrO_2$ model alloy, aiming at optimization of milling condition based on microstructure and microchemistry. The variation of mechanical property and its correlation to microstructure is also discussed.

**Chapter IV** presents the results on the evolution of phases during annealing of Fe - 15 Wt. % $ZrO_2$model alloy. Assessment of the thermal behavior by DSC measurements and an understanding on the microstructural evolution of the system with temperature is arrived with rigorous analysis through diffraction and microscopic techniques.

**Chapter V** reports the synthesis and characterization of $ZrO_2$ dispersion strengthened 9 Cr ferritic steel powder at optimized milling conditions and its evolution with high temperature annealing. Stability of the matrix and the dispersoid is investigated and formation of new phases is discussed.

**Chapter VI** details the structural analysis of 9 Cr $ZrO_2$ ODS consolidated through SPS. The microstructure of the sintered sample, long term thermal evolution of the matrix and dispersoid phases is discussed. The evaluation of mechanical property through experimental and predictive tools is also conferred.

Finally, **Chapter VII** provides a comprehensive summary of the thesis and also describes the scope for future work.

Table 1.6 given below shows the thesis organization as well as the brief contents of each of the chapter.

**Table 1.6: Organizations of thesis chapters**

| Chapter | Title | Content |
|---|---|---|
| **I** | Introduction | Literature survey, existing gaps, objectives of the present study and organization of the thesis. |
| **II** | Materials and methods | Theory and Principle, experimental details, calibration, error and accuracy of investigation methods. |
| **III** | Synthesis and microstructural characterization of Fe – 15 Wt. % $ZrO_2$ Model alloy | Evolution of microstructure and microchemistry and optimization of milling condition. The variation of mechanical property and its correlation to microstructure. |
| **IV** | Thermal evolution of Fe – 15 Wt. % $ZrO_2$ model alloy | Evolution of phases during annealing,Assessment of the thermal behavior and microstructural evolution through diffraction and microscopic techniques. |
| **V** | Synthesis and characterization of $ZrO_2$dispersed 9 Cr steel powder | Microstructure of as synthesized powder and its evolution with high temperature annealing. Stability of the matrix and the dispersoid at high temperatures and formation of new phases. |
| **VI** | Microstructural characterization of consolidated $ZrO_2$dispersion strengthened ferritic steel | Structural analysis of the consolidated $ZrO_2$ dispersed steel. The microstructure of the sintered sample, long term thermal evolution of the matrix and dispersoid phases. The evaluation of mechanical property through experimental and predictive tools. |
| **VII** | Summary and scope for future work | |

## 1.11 References

1. Ladoucette, P. D., "*Electricity of the future: a worldwide challenge*" France, (2010)
2. Sundaram, C. V., *et al.*, *Atomic Energy in India, 50 Years*. Government of India, Department of Atomic Energy(1998)
3. *Annual Report of the Department of Atomic Energy,* Government of India. S.N. Gupta, (1992)
4. *The Saga of Atomic Energy Programme in India,*Department of Atomic Energy, (2005)
5. Kapoor, K., *et al.*, *Renewable and Sustainable Energy Reviews* (2014) 40, 475
6. Dawn, S., *et al.*, *Renewable and Sustainable Energy Reviews* (2016) 62, 215
7. Nature Materials Editorial (2009) 8:81
8. Raj, B., *et al.*, *MRS Bulletin* (2008) 33 (4), 327
9. Vijayan, P. K., *et al.*, *Progress in Nuclear Energy* (2017) 101, 43
10. Jayaram, K. M. V., In *Thorium-Based Nuclear Fuel: Current Status and Perspectives*, International Atomic Energy Agency(1987)
11. Raj, B., *et al.*, *Sodium Fast Reactors with Closed Fuel Cycle*. CRC Press (2015)
12. Baldev Raj, V. M., Ferritic Steels and Advanced Ferritic - Martensitic Steels. In *Comprehensive Nuclear Materials*, Elsevier Science, Amsterdam, (2012), p 105
13. Banerjee, S., and Gupta, H. P., *Progress in Nuclear Energy* (2017) 101, 4
14. Wattal, P. K., *Progress in Nuclear Energy* (2017) 101, 133
15. Kakodkar, A., Evolving Indian nuclear programme: Rationale and perspective (2011)

16. Gopalakrishnan, A., *Annual Review of Energy and the Environment* (2002) 27 (1), 369
17. Duffey, R. B., and Sur, B., *Energy Procedia* (2011) 7, 286
18. Baldev Raj, A. T., Fazio Concetta, Structural Materials: New Challenges, Manufacturing and Performance. (2009)
19. Rodriguez, P., What Happens to Structural Materials in a Nuclear Reactor: The Fascinating Radiation Enhanced Materials Science; (2005)
20. Yvon, P., and Carré, F., *Journal of Nuclear Materials* (2009) 385 (2), 217
21. Azevedo, C. R. F., *Engineering Failure Analysis* (2011) 18 (8), 1943
22. Simnad, M. T., Nuclear Reactor Materials and Fuels. In *Encyclopedia of Physical Science and Technology*, Academic Press, New York, (1987)
23. Raj, B., *Bulletin of Materials Science* (2009) 32 (3), 271
24. Northwood, D. O., *Materials & Design* (1985) 6 (2), 58
25. Sheinberg, H., *et al.*, Dispersion strengthened copper. Google Patents(1990)
26. Ukai, S., and Fujiwara, M., *Journal of Nuclear Materials* (2002) 307–311, Part 1 (0), 749
27. Baldev Raj, P. S. R., T Jayakumar, Advances in Stainless steels. In *Series in Meatllurgy and Materials Science*, Raj, B., (ed.) Universities Press(2010)
28. Leibowitz, L., and Blomquist, R. A., *International Journal of Thermophysics* (1988) 9 (5), 873
29. Zinkle, S. J., and Snead, L. L., *Annual Review of Materials Research* (2014) 44 (1), 241
30. Saroja, S., *et al.*, *Journal of Nuclear Materials* (2011) 409 (2), 131

31. Klueh, R. L., *et al.*, *Journal of Nuclear Materials* (2005) 341 (2–3), 103

32. Ukai, S., *et al.*, *Journal of Nuclear Science and Technology* (1997) 34 (3), 256

33. Ukai, S., *et al.*, *Journal of Nuclear Materials* (1993) 204, 65

34. Kimura, A., *et al.*, *Journal of Nuclear Materials* (2011) 417 (1–3), 176

35. Verhiest, K., *et al.*, *Ceramics International* (2014) 40 (9, Part A), 14319

36. Verhiest, K., *et al.*, *Journal of Nuclear Materials* (2009) 385 (2), 308

37. Odette, G. R., *et al.*, *Annual Review of Materials Research* (2008) 38 (1), 471

38. Odette, G. R., *Scripta Materialia* (2017)

39. Dasgupta, A., *et al.*, Electron Microscopy Studies on Oxide Dispersion Strengthened Steels. In *Materials Challenges and Testing for Supply of Energy and Resources*, Springer Berlin Heidelberg, Berlin, Heidelberg, (2012), pp 117

40. Murty, K. L., and Charit, I., *Journal of Nuclear Materials* (2008) 383 (1–2), 189

41. Benjamin, J. S., Mechanical Alloying. In *Scientific American*, (1976), Vol. 234, pp 40

42. Benjamin, J. S., *Metallurgical Transactions* (1970) 1 (10), 2943

43. Coolidge, W. D., *Proc. Am. Inst. Elect. Eng* (1910), 961

44. Irmann, R., *Techn. Rundschau* (1949) 41 (36), 19

45. Alexander, G. B., Iler, R. K., West, S. F., US Patent 2,972,529, (February 21, 1961.)

46. Zhang, L., *et al.*, *Acta Materialia* (2009) 57 (12), 3671

47. Zhang, L., *et al.*, *Journal of Alloys and Compounds* (2012) 512 (1), 39

48. Zhang, L., *et al.*, *Journal of Materials Engineering and Performance* (2012) 21 (11), 2487

49. Zhang, L., *et al.*, *Powder Metallurgy* (2013) 56 (1), 24

50. Ukai, S., *et al.*, *Journal of Nuclear Materials* (1993) 204 (0), 65

51. Ogbuji, L. U., *Oxidation of Metals* (2004) 62 (3), 141

52. Zhao, X., *et al.*, *International Journal of Minerals, Metallurgy, and Materials* (2016) 23 (12), 1444

53. Galatanu, M., *et al.*, *Fusion Engineering and Design* (2017)

54. He, X. D., *et al.*, *Journal of Alloys and Compounds* (2009) 467 (1), 347

55. M. Mujahid, C. A. G. a. J. W. M. A. I.,

56. Hayama, A. O. F., *et al.*, *Materials Science and Engineering: A* (2004) 371 (1), 198

57. Jones, A., *"Historical Perspective: ODS Alloy Development*". San Diego, CA, (November 2010.)

58. Huet, J. J., *Powder Metallurgy* (1967) 10 (20), 208

59. De Bremaecker, A., *Journal of Nuclear Materials* (2012) 428 (1), 13

60. Ukai, S., *et al.*, *Journal of Nuclear Materials* (1998) 258, 1745

61. Odette, G. R., *Journal Of Materials* (2014) 66 (12), 2427

62. Bailly H, M. D. a. P. C., *The nuclear fuel of pressurized water reactors and fast reactors design and behaviour*. Lavoisier Publishing: Paris, 1999

63. Lallement R, M. H., Mustelier J P and Villeneuve J, *Nuclear Energy* (1989) 28(1), 41

64. Klueh, R. L., *Transactions of the Indian Institute of Metals* (2009) 62 (2), 81

65. Kadiri, G., Ph.D Thesis. Homi Bhabha National Institute

66. Goddard, J. K., Characterization of Two ODS Alloys: 18Cr ODS and 9Cr ODS University of South Carolina, (2001)
67. Ukai, S., *et al.*, *Materials Science and Engineering: A* (2009) 510–511, 115
68. Ohtsuka, S., *et al.*, *Journal of Nuclear Materials* (2004) 329–333, Part A, 372
69. Kimura, A., *et al.*, *Journal of Nuclear Science and Technology* (2007) 44 (3), 323
70. Rösler, J., *et al.*, *Metallurgical Transactions A* (1992) 23 (5), 1521
71. Mirchandani, P. K., *et al.*, Aluminum-base composite alloy. Google Patents(1992)
72. Martin, J. W., *Micromechanisms in Particle-Hardened Alloys*.
73. Bergner, F., *et al.*, *Metall and Mat Trans A* (2016) 47 (11), 5313
74. Worn, V. A. T. a. D. K., *Powder Metallurgy* (1962) (10)
75. Grant, R. M. a. N. J., *Powder Metallurgy* (1962) (10)
76. Grant, L. J. B. a. N. J., *Trans. TMS-AIME* (1962) 224
77. B.Alexander, G., U.S. Patent, (1961)
78. Wen, Y., *et al.*, *Materials Science and Engineering: A* (2012) 544, 59
79. Moghadasi, M. A., *et al.*, (2016) 6, 38621
80. Springer, H., *et al.*, *Materials & Design* (2016) 111, 60
81. Toualbi, L., *et al.*, *Journal of Nuclear Materials* (2012) 428 (1), 47
82. Shi, Z., and Han, F., *Materials & Design (1980-2015)* (2015) 66, 304
83. Boegelein, T., *et al.*, *Acta Materialia* (2015) 87, 201
84. Hoyt, S. L., (1930) 89, 9
85. Suryanarayana, C., *Mechanical Alloying And Milling*. Taylor & Francis: (2004)

86. Badmos, A. Y., Some Properties of Mechanically Alloyed Oxide Dispersion Strengthened Metals. University of Cambridge, Cambridge, (1997)

87. Suryanarayana, C*., et al.*, *Journal of Materials Science* (2011) 46 (19), 6301

88. Suryanarayana, C*., et al.*, *Materials Science and Engineering: A* (2001) 304–306, 151

89. Suryanarayana, C., and Al-Aqeeli, N., *Progress in Materials Science* (2013) 58 (4), 383

90. Suryanarayana, C., *Progress in Materials Science* (2001) 46 (1–2), 1

91. C. Suryanarayana, E. I., V.V. Boldyrev, *Materials Science and Engineering A* (2001), 151

92. Murty, B., and Ranganathan, S., *International materials reviews* (1998) 43 (3), 101

93. Unifantowicz, P*., et al.*, *Fusion Engineering and Design* (2011) 86 (9), 2413

94. Dieter, G. E., *Mechanical metallurgy*. McGraw-Hill: (1986)

95. Jang, J. S. C., and Koch, C. C., *Scripta Metallurgica et Materialia* (1990) 24 (8), 1599

96. Petch, N. J., *J. Iron Steel Inst. London* (1953) 173, 25

97. Groza, J. R., and Gibeling, J. C., *Materials Science and Engineering: A* (1993) 171 (1), 115

98. Humbert, M., Oxide Dispersion Strengthened Alloys(2012)

99. A K Bhargava , and C.PSharma, *Mechanical Behaviour and Testing of Materials*. PHI Learning Private Limited: (2011)

100. Popovich, A. A., *Journal of Alloys and Compounds* (1994) 215 (1), 169

101. Dai, L., *et al.*, *Materials Science and Engineering: A* (2016) 674, 579
102. Jha, S. C., *et al.*, *Materials Science and Engineering: A* (1989) 119, 103
103. Reed, T. B., *Free Energy formation of Binary compounds*. MIT Press: Cambridge, Massachusetts, (1971)
104. Dean, J. A., and Lange, N. A., *Lange's handbook of chemistry*. McGraw-Hill: 1992
105. He, L. F., *et al.*, *Scripta Materialia* (2011) 64 (6), 548
106. Rösler, J., and Arzt, E., *Acta Metallurgica et Materialia* (1990) 38 (4), 671
107. Krautwasser, P., *et al.*, *High Temperatures. High Pressures* (1994) 26 (5), 549
108. Chen, T., *et al.*, *Acta Materialia* (2016) 116, 29
109. Parida, P. K., *et al.*, *Journal of Nuclear Materials* (2013) 441 (1–3), 331
110. Liu, T., *et al.*, *Progress in Natural Science: Materials International* (2013) 23 (4), 434
111. Oono, N. H., *et al.*, *Journal of Nuclear Materials* (2017) 493, 180
112. Oono, N., *et al.*, *Nuclear Materials and Energy* (2016) 9, 342
113. Baldan, A., *Journal of Materials Science* (2002) 37 (11), 2171
114. Pint, B. A., *et al.*, The Oxidation Behaviour of ODS Iron Aluminides. In *Oxidation of Intermetallics*, Wiley-VCH Verlag GmbH(2007), pp 183
115. Dai, L., *et al.*, *Powder Technology* (2012) 217 (0), 281
116. Susila, P., *et al.*, *Materials Science and Engineering: A* (2011) 528 (13–14), 4579
117. Hirata, A., *et al.*, *Nat Mater* (2011) 10 (12), 922
118. Hsiung, L. L., *et al.*, *Physical Review B* (2010) 82 (18), 184103

119. Pasebani, S*., et al.*, *Acta Materialia* (2013) 61 (15), 5605

120. Pasebani, S*., et al.*, *Journal of Nuclear Materials* (2013) 434 (1–3), 282

121. ASM International, Ohio, Materials Park, (1992)

122. Pasebani, S*., et al.*, *Journal of Nuclear Materials* (2017) 495, 78

123. Hoffmann, J*., et al.*, *Journal of Nuclear Materials* (2013) 442 (1–3), 444

124. Kim, I.-S*., et al.*, *Metals and Materials* (2000) 6 (6), 513

125. Lescoat, M. L*., et al.*, *Journal of Nuclear Materials* (2011) 417 (1), 266

126. Yozo Kawasaki, Y. I., Toshiharu Kobayashi, Hideshi Sumiyoshi, *ISIJ International* (1996) 36, 1208

127. Zhang, J*., et al.*, *Acta Metallurgica Sinica (English Letters)* (2016) 29 (11), 1047

128. Lawn, R. E*., et al.*, *Powder Metallurgy* (1976) 19 (4), 196

129. Wilson, F. G*., et al.*, *Metallurgical Transactions A* (1978) 9 (2), 275

130. Pasebani, S., and Charit, I., *Journal of Alloys and Compounds* (2014) 599, 206

131. Li, Z*., et al.*, *Fusion Engineering and Design* (2017) 121, 159

132. Xu, W. Z*., et al.*, *Journal of Nuclear Materials* (2014) 452 (1–3), 434

133. Wang, B. A*., et al.*, *Materials Science and Engineering: A* (2017) 692, 168

134. Nagorka, M. S*., et al.*, *Metall and Mat Trans A* (1995) 26 (4), 873

135. Bandriyana*, et al.*, *IOP Conference Series: Materials Science and Engineering* (2017) 176 (1), 012047

136. M.Bormann, B. L., *Nucl.Phys. A* (1969) 130, 195

137. Darling, K. A*., et al.*, *Materials Science and Engineering: A* (2010) 527 (15), 3572

138. Darling, K. A*., et al.*, *Scripta Materialia* (2008) 59 (5), 530

139. Saber, M., *et al.*, *Materials Science and Engineering: A* (2012) 556 (0), 664

140. Saber, M., *et al.*, *Journal of Applied Physics* (2013) 113 (6), 063515

141. Saber, M., *et al.*, *Journal of Applied Physics* (2013) 114 (10), 103510

142. Li, W., *et al.*, *Powder Technology* (2017) 319, 172

143. Zhang, L., *et al.*, *Materials Science and Engineering: A* (2017) 695, 66

144. Xu, H., *et al.*, *Materials Science and Technology* (2017), 1

145. Takaya, S., *et al.*, *Journal of Nuclear Materials* (2012) 428 (1), 125

146. Kotan, H., *et al.*, *Journal of Alloys and Compounds* (2014) 615 (0), 1013

147. Dou, P., *et al.*, *Journal of Nuclear Materials* (2014) 444 (1), 441

148. Gao, R., *et al.*, *Journal of Nuclear Materials* (2014) 444 (1–3), 462

149. Takahashi, K., and Tanaka, Y., *Physical Review B* (2017) 95 (1), 014101

150. Axtell, S. C., and Schalek, R., *Journal of Applied Physics* (1996) 79 (8), 5263

151. Jha, P., *et al.*, *Journal of Composite Materials* (2014) 48 (17), 2107

152. Hemanth, J., *Materials Science and Engineering: A* (2009) 507 (1–2), 110

153. Taguchi, M., *et al.*, *Materials Transactions* (2008) 49 (6), 1303

154. Muccillo, R., *Materials Science Forum* (2005) 498-499, 331

155. Hung, L. S., *et al.*, *Applied Physics Letters* (1983) 42 (8), 672

156. Yavari, A. R., *Ordering and Disordering in Alloys*. Springer Netherlands, (2012)

157. Groza, J., *Journal of Materials Engineering and Performance* (1992) 1 (1), 113

158. Heintze, C., *et al.*, *Journal of Nuclear Materials* (2012) 428 (1), 139

159. Brocq, M., *et al.*, *Acta Materialia* (2010) 58 (5), 1806

160. Parida, P. K., *et al.*, *Transactions of the Indian Institute of Metals* (2016), 1

161. Parida, P. K., *et al.*, *European Microscopy Congress 2016: Proceedings*, Wiley-VCH Verlag GmbH & Co. (2016)

162. Vijay, R., *et al.*, *Metall and Mat Trans A* (2013) 44 (3), 1611

163. Y. Kimura, S. T., S. Suejima, R. Uemor, H. Tamehiro, *ISIJ International* (1999) 39 176

164. Dai, L., *et al.*, *Journal of Materials Science* (2013) 48 (4), 1826

165. de Castro, V., *et al.*, *Journal of Nuclear Materials* (2009) 386, 449

166. Keith, M., Processing and Characterization of Oxide Dispersion Strengthened 14YWT Ferritic Alloys. University of Tennessee, Knoxville, (2006)

167. London, A. J., *et al.*, *Acta Materialia* (2015) 97, 223

168. Dou, P., *et al.*, *Journal of Nuclear Materials* (2013) 442 (1–3, Supplement 1), S95

169. Susila, P., *et al.*, *Journal of Materials Science* (2010) 45 (17), 4858

Chapter II

# Materials and Methods

## 2.1 Introduction

To arrive at a comprehensive understanding of the material properties, it is important to choose the right set of characterizing tools, keeping in mind their capabilities. Proper choice of operating conditions, sources of errors, accurate interpretation of results are all equally important. The current chapter gives a detailed explanation of the experimental methodology adopted in the current study. The discussions include experimental procedures used for the synthesis of mechanically milled powders. The microstructural characterization tools described include diffraction and microscopy based techniques along with thermal analysis through calorimetry. Techniques utilized for mechanical property evaluation are also discussed. Details of operating conditions, data analysis and sources of errors are also explained wherever it is relevant.

The chapter is organized as follows. Section 2.1 gives a brief introduction to the chapter with section wise flow of the thesis. Section 2.2 and 2.3 describes the materials investigated and methods utilized for characterizing the materials. These sections are further subdivided as follows. Brief discussion on synthesis of alloy powders through mechanical milling is discussed in section 2.2.1 with details on Fe - 15 Wt. % $ZrO_2$ model alloys in 2.2.1.1 and $ZrO_2$ dispersed 9 Cr steel powders in 2.2.1.2. The details includes the milling conditions, medium and instrumental details. Section 2.2.2 describes the compaction and annealing of milled powders followed with a note on consolidation of powders by Spark Plasma Sintering in 2.2.3. Section 2.2.4 gives description of specimen preparation for different characterizations with an emphasis on

FIB technique. Further, the details on the microstructural characterization methods are divided into 5 subsections as follows. The section 2.3.1 presents a note on microstructural analysis through SEM, followed with a description on TEM technique in section 2.3.2. Discussion on semi quantitative chemical analysis through EDS is presented in section 2.3.3, with a note on sources of error. Further, the XRD analysis of the materials through cobalt and synchrotron radiation are described in section 2.3.4 with description on experimental conditions and also on the choice of target material. The thermal analysis of the powder through DSC technique is discussed in section 2.3.5. Hardness measurements of the material through nanoindentation and Vickers hardness measurements for both powder and consolidated specimen are described in section 2.3.6. The section 2.3.7 gives a very brief note on EBSD technique which was utilized in the current study for the analysis of grain size and strain evolution of the consolidated and long term thermally exposed material. The chapter concludes with a summary of the whole chapter in section 2.4.

## 2.2 Materials

### 2.2.1 Synthesis of alloy powders through mechanical milling

This study includes synthesis of two alloy systems namely (1) Fe-15 Wt. % $ZrO_2$ and (2) 9Cr steel powder dispersed with 0.35 Wt. % $ZrO_2$ powder. Since the pre alloyed steel powder is utilized, the synthesis route here is termed as mechanical milling [1]. The mechanical milling is carried out at Institute of Minerals and Materials Technology, Bhubaneswar, in an In-Smart, India make planetary ball mill with a grade 440C stainless steel balls and vial, with a hardness of 832 HV. The milling mechanism involves, high energy frequent impact of balls resulting in milling of the powder. In addition, the rotation of base plate provides the centrifugal force to the grinding balls. Independent rotation of vials, in opposite direction, makes the balls to hit the inner wall of the vial [1-4]. Since the vials are rotating in opposite direction, a considerable part of grinding is done due to friction. In the present work the base plate rotation is fixed at 300 RPM whereas the vial rotates at 150 RPM. Post milling, the powders were collected from the vial inside a glove box maintained under Argon atmosphere and preserved in a sealed container.

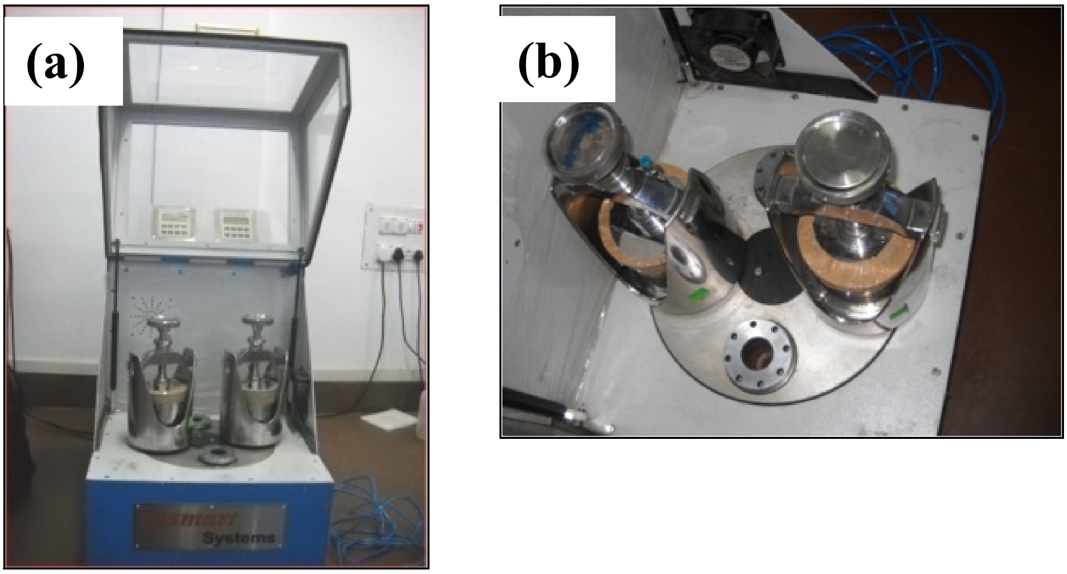

**Figure 2.1: (a) In Smart make planetary ball mill used in the present study (b) A magnified image showing the stainless steel vials placed on a base plate.**

### 2.2.1.1 Synthesis of Fe - 15 Wt. % $ZrO_2$ model alloy

Fe (sieve size of +325 mesh) and $ZrO_2$ powders were procured from M/s, HIMEDIA, India with a commercial purity grade of 99.5% and 99%, respectively. The powders were blended together and mechanically milled in the proportion of Fe -15 Wt. % $ZrO_2$. The ball to powder ratio was maintained at 10:1 and process carried out under high purity Argon atmosphere in order to avoid unwanted oxygen pickup from atmosphere during milling. Milling was carried out for different durations, viz., 0 (blended powder), 10, 30, 60 and 100 h.

### 2.2.1.2 Synthesis of $ZrO_2$ dispersed 9Cr steel powder

The gas atomized 9Cr steel powders with particle sizes of <150μm (sieve size -100 mesh) is used for the synthesis of $ZrO_2$ dispersed steel powder and its chemical composition is listed in Table 2.1. The alloy powder was mixed with ~ 0.35 Wt. % of monoclinic $ZrO_2$ and mechanically milled for 100h in a planetary ball mill in an Ar atmosphere. The ball to powder ratio was kept constant at 10:1.

**Table 2.1: Chemical composition of the 9Cr steel powder (Wt. %)**

| Fe | Cr | W | Mn | Ni | Si | P | C | S | O | N | Al |
|---|---|---|---|---|---|---|---|---|---|---|---|
| Bal | 9.2 | 2.25 | 0.026 | 0.01 | 0.02 | 0.004 | 0.015 | 0.001 | 0.015 | 0.002 | <0.005 |

## 2.2.2 Compaction and annealing of milled powders

In order to understand the microstructural changes with high temperature exposure, annealing of milled powders of both model alloy and ODS steel was carried out at different temperatures. To avoid the high temperature oxidation, pelletisation of the powder followed by vacuum sealing was necessary. Accordingly, the powders were formed into pellets of 10 mm diameter in a uni-axial press under a pressure of ~ 200 MPa. The pellets were then transferred to a quartz tube, evacuated to vacuum levels better than $10^{-5}$ mbar and fused for sealing. Extreme care was taken in avoiding the contamination of the powders during these stages. The quartz tubes containing the pellets were annealed at temperatures of interest, details of which are given in the relevant sections.

### 2.2.3 Consolidation of powders by SPS and their heat treatments

Applicability of a powder depends on the ability to reach near theoretical density through a suitable method. In this respect, SPS of powders is a relatively new sintering based technique having specific advantages for ODS steel production. Compared to other conventional techniques such as HE and HIP, which has a ramp rate of 50 - 80 K/min and a few hours of holding time, SPS has the advantage that it is characterised by very fast heating (up to 2000 K/min) and cooling rates and short holding times (minutes) to achieve near theoretical density [5]. In addition to that, SPS works at a lower temperature of compaction and relatively low applied pressure [6].

During the SPS process, the powder to be consolidated is loaded into an electrically and thermally conductive graphite mould and a large DC pulsed current (1000–5000 A) is applied under a uni-axial pressure. Though heat is rapidly generated internally during SPS, the sintering process is very different from pressureless or hot press sintering [7]. When current passes through the graphite mould the powder is heated from both outside and inside owing to the Joule heating from the intrinsic electrical resistance of the powder material, resulting in a consolidated specimen [8]. The schematic representation of an SPS unit is shown in figure 2.2. The SPS unit consists of a pressure device with upper and lower water-cooled hydraulic rams, a DC generator that generates pulses and a computer-based process controller. The shrinkage, pressure, average voltage and current are recorded during the process. The powder is filled inside the conductive graphite die for sintering with optical pyrometer or thermocouple as temperature detector [7]. The experimental conditions chosen in the current study are listed as below in Table 2.2. It is to be noted here that, the SPS process is followed by conventional Normalizing and Tempering treatments for the release of excess strain. This is done to achieve fair ductility and homogeneous microstructure. The normalizing was carried out at 1323 K for 1h followed by a tempering treatment at 1023 K for 1h.

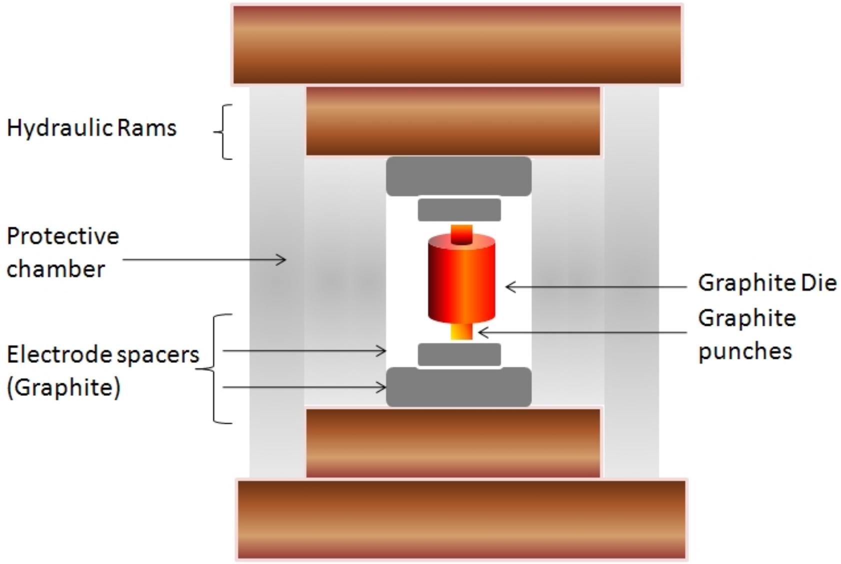

**Figure 2.2: Schematic drawing of an SPS unit containing an assembled graphite die and punches**

**Table 2.2: SPS parameters used in the current study**

| | |
|---|---|
| **Temperature** | 1323 K |
| **Pressure** | 50 MPa |
| **Hold time** | 10 minutes |
| **Ramp rate** | 100 K/min during heating and furnace cooling |

### 2.2.4 Specimen preparation for microstructural characterizations

Specimen preparation for microstructural characterization is often referred to as an art. However, lot of science and technology is involved in modern day specimen preparation methodology. Possibly, the most critical point in the preparation of a sample, is that it must be representative of the bulk material in both structure and composition and there should be no alteration to these properties during the preparation itself, else that would be an artifact. Hence the specimen preparation step is an essential and important [9, 10] step in studying a material. In short, a specimen prepared well, is half job done! Accordingly, the preparation methods employed for SEM, TEM and hardness measurements are discussed in detail as follows.

For SEM of powder samples, an adhesive carbon tape was spread and sprinkled with powder particles and gold coated. The coating is required for better conduction and to avoid SEM column contamination by fine magnetic powder particles. For SEM of consolidated specimen, flat surface was obtained by successive grinding with SiC abrasives followed by a mirror finish of the surface obtained by polishing with 1 μm diamond paste with DP blue as the lubricant. The polished samples were etched with Villela's reagent to reveal the microstructural features. Vilella's reagent used for the sample preparation contained 1g of picric acid and 5 ml of HCl in solution of 100 ml in methanol.

Specific to the TEM analysis, the goal of the specimen preparation is to produce an electron transparent specimen, representative of the bulk. The alloy powders produced in this study consists of nanoparticles which are magnetic in nature and thus demands special attention in specimen preparation. The preparation of TEM samples of magnetic powders is difficult due to following reasons. The magnetic particles exhibit agglomeration, which although can be dispersed in a solution by ultrasonication, readily get agglomerated as soon as the sonification is stopped. Agglomerates are thick and hence will not be electron transparent. In addition to that, since the sample is placed between electromagnetic pole pieces of the objective lens of the TEM, the nanoparticles can get magnetized, leading to sample drift under electron beam and it may also contaminate the pole pieces with the nanoparticles attracted towards them [10]. Hence, it becomes essential that, the nanoparticles should be embedded in a medium, which is stable under an electron beam for TEM investigations. A Gatan made G1 epoxy has been utilized for TEM sample preparation of nanoparticles. The two parts of this epoxy, i.e; resin and hardener were mixed in 10:1 ratio in a glass slide, using a toothpick and the alloy powder to be examined was sprinkled on to this and thoroughly mixed. The powder mixture embedded in epoxy was then transferred to Teflon cylinders of ~ 3.5 mm diameter and 2 mm height, placed on a glass slide covered with Teflon tape. This assembly of Teflon rings in a glass slide was then transferred to a hot plate and temperature is increased to ~ 393 K. In ~ 20 - 30 minutes, the epoxy sets into a brown colored stable solid cylinder. Since the bonding between the epoxy and the Teflon is weak, the powder embedded epoxy can be peeled-off readily. Further, it was subjected to mechanical polishing which reduces the thickness to about ~ 100 μm.

These discs were then dimpled so that the thickness at the central portion reduces to about 20 μm. Further, argon ion beam thinning (Technoorg Linda make IV-4) at high angles (~ $12^o$) was carried out till a perforation in the sample appear followed by that, final polishing was done at ~ $4^o$ in a gentle miller (Technoorg Linda make IV-6). A schematic of the procedure is given in figure 2.3.

Further, When the powder particle size was large (> 10 μm), the sample preparation through conventional technique becomes difficult and thus FIB technique is employed. The FIB technique is also important owing to the great interest in the preparation of site-specific TEM specimen preparation [11, 12]. Typically FIB uses a

$Ga^+$ ion beam source, which is accelerated and rastered over the specimen’s surface so that site-specific milling / imaging of the sample can be performed based on the choice

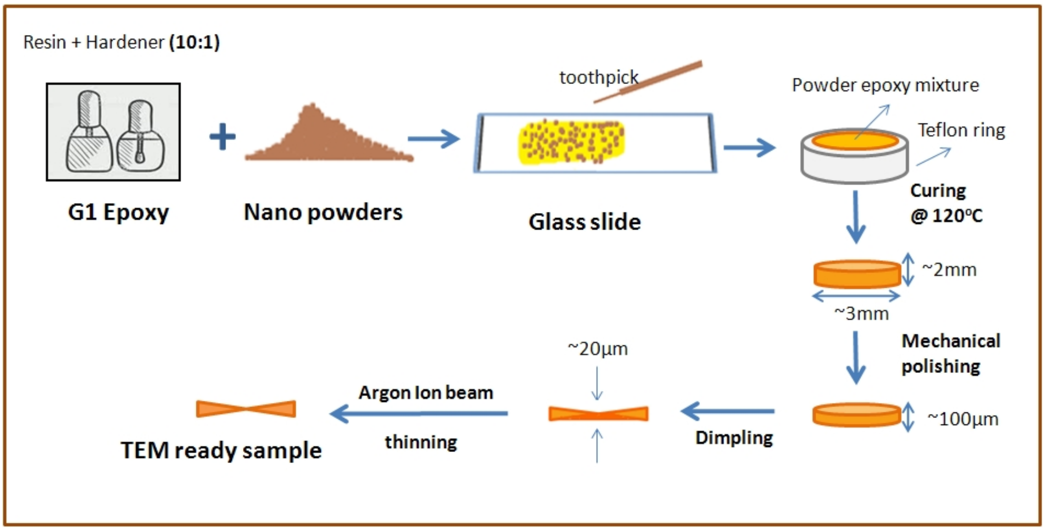

**Figure 2.3 : Schematic of TEM specimen preparation from magnetic powder particles**

**(a)** **(b)** **(c)**

**Figure 2.4: (a) Protective Platinum coating on ROI (b) Trench creation through high ion beam current (c) Lift out of the lamellae with omniprobe needle**

**(d)** **(e)**

**(d) Welding of the lamellae to the TEM grid**

**(e) Thinning of the specimen to electron transparency**

of ion current [10]. In the current study, FEI make dual-beam Helios Nanolab 600i instrument was used for the site specific sample preparation.

The typical steps involved in this process are as follows. The process begins with an identification of ROI followed by protection of ROI with platinum deposition using GIS. Further, trenches were created adjacent to the platinum coated region using high ion beam current followed by removal of excess beam damage by slightly lower beam current. The under cuts were made to enable the lamellae to be free from the bulk specimen. Further, the lamella was lift out using an Omniprobe attached with the SEM column. The lifted lamellae was then transferred to the TEM grid and welded with platinum metal. The lamellae thus prepared was then thinned down to ~ 20 – 40 nm and finally cleaned with low energy $Ga^+$ beam. The stepwise preparation of FIB lamella is shown in figure 2.4.

## 2.3 Characterization of powders and consolidated specimen

Extensive analysis tools available for microstructural characterization of the material were utilized in the current investigation to gain a comprehensive understanding of the material. Attempts were made to correlate the results and supplement with various characterizations. An overall picture of the tools utilized in the current study and the experimental conditions are presented in the subsequent sections.

### 2.3.1 Scanning Electron Microscopy

SEM is an important tool for microstructural investigation, which can provide crucial information based on topography and atomic number contrast. SEM investigation provides direct information about surface morphology of materials which is essential to understand the evolution of phases with changes in processing parameters. Accordingly it was utilized in the current study for characterizing the surface microstructure of the material [13, 14]. The FEI make Helios NanoLab-600i dual beam FEG-SEM was used to study the size and morphology of the as milled and annealed powders and also to investigate the microstructure of the consolidated specimen. Both SE and BSE modes of operation are used depending on the requirement of problem at hand. Accelerating voltage in the range of 5 - 30 kV and beam current from 1.4 nA to 5.5 nA were utilized based on the requirements.

### 2.3.2 Transmission Electron Microscopy

TEM studies were carried out using a Philips CM200 analytical Transmission Electron Microscope fitted with an on axis TVIPS make CCD camera with a resolution of 2048 x 2048 pixels. The operating voltage was maintained at 200 kV throughout. Magnification calibration was carried out with a cross grating of 2160 lines/mm with a separation of 469 nm between two lines. Camera length was calibrated with standard nanocrystalline oriented gold in holey carbon film at different accelerating voltages. Analyses of SAED and micro-diffraction patterns were carried out to identify the presence of different phases. A selected-area aperture of 10 μm size was used for obtaining the SAED pattern and its rotation with respect to magnification was calibrated using $MoO_3$ crystals. For indexing electron diffraction patterns, the angles and d-spacing were measured with an accuracy of <1° and 0.2 Å respectively. The measured d-spacing values are compared with standard ICDD card, the angle between the planes were calculated and matched to the measured values.

BF and DF microscopy techniques were employed in structural imaging of the material. For obtaining DF images, smallest aperture available i.e. 5 μm size is utilized.

For analyzing the size distribution of the matrix phase (Fe), $ZrO_2$ dispersoids and FeO, as a function of either milling duration or annealing temperature, Image J analysis software is utilized [15]. The sizes were measured by manually adjusting the color threshold by judiciously choosing the pixels corresponding to the crystallites (whose sizes have to be measured) and by fixing the minimum size and maximum pixel area size to exclude anything that is not an object of interest in the image. Roundness values between 0.0 and 1.0 were selected to help exclude unwanted objects [16]. The particle sizes were then obtained by choosing the minimum ferret diameter, which is often used as the diameter equivalent to a sieve analysis.

The Phase contrast microscopy studies were carried out in a Tecnai $G^2$ F30 ultra-twin HRTEM operated at 300 kV with a point to point resolution of 0.17 nm. The microscope consist an ultra-twin objective lens with 0.65 mm spherical ($C_s$) and 1.4 mm chromatic aberration ($C_c$) coefficients. The microscope is also equipped with a high speed digital search and view camera (2k x 2k) of Gatan Inc make for image and spectrum acquisition and analysis.

### 2.3.3 Chemical analysis through Energy Dispersive Spectroscopy

EDS makes use of the X-rays emitted by a solid sample when bombarded with a focused beam of electrons, to obtain localized chemical information. In principle, elements from atomic number 4 (Be) to 92 (U) can be detected, but quantification of elements with atomic number <10 is not reliable. EDS is a qualitative analysis involving the identification of the lines in the spectrum with the corresponding elements and it is also a semi quantitative analysis technique, which allows a rough estimation of the concentrations of the elements present in the material. The EDS analysis can be carried out in a SEM as well as TEM and in the current study both were utilized.

The EDS in SEM was carried out using an EDAX make Apollo X Silicon Drift Detector attached to the FEI make Helios Nanolab 600i instrument. In order to excite the Kα X Rays of Fe and keeping in mind, the over voltage required for this, a 20 kV voltage is used. For spot analysis, the beam current was maintained at 2.7 nA and a collection time of 50 live seconds were maintained. To get the elemental mapping for an area of 512*512 pixels, beam conditions were maintained at a voltage of 20 kV, beam current of 5.5 nA and a dwell time of 50 µs. The higher current enable in enhanced signal and reduced scan time, which helped in overcoming the beam drift issues for a longer scan time.

Within the TEM, EDS analysis was carried out using an Oxford X-Max 80 detector. A spot size of ~7.5 nm was used to collect the characteristic X-rays from the constituent phases for determining the composition. A low background single tilt holder was used to reduce the noise due to spurious X-rays. In-hole spectra were collected periodically to ensure the absence of spurious X-ray sources in the column of the microscope. The performance of the equipment and the reliability of the measurements were monitored by the periodical checking of the energy calibration carried out with pure Al and Cu and the energy resolution with Mn Kα. Composition analysis was carried out assuming the thin foil criterion based on the observation that the intensity difference was less than 10% between the in-hole spectrum and that on the specimen. The error in quantifying the elemental composition was minimized by keeping a collection time of ~100 live seconds. It is assumed that collection of the spectra is from within the beam size and volume of the sample encloses only the ROI without overlapping of phases, though in some cases it was difficult to ensure this condition.

### 2.3.4 X-Ray Diffraction Technique

The proper choice of radiation for diffraction analysis depends on what we are looking for and on nature of the sample under investigation. In this study, for the analysis of model ODS alloy, the Co Kα X-rays ($\lambda$=1.78896 Å) were preferred over Cu to avoid the loss of information due to excess fluorescence. The X-ray powder diffraction step scan data were recorded at room temperature using a Bruker AXS D8 discover instrument. The X-ray Beam voltage and current were maintained at 35 kV and 25 mA respectively. The step scan data of the experimental samples was recorded for the angular range of $15^o$ – $105^o$, in step size $0.02^o$ and for 5 sec counting time per each step. Instrumental broadening was calculated by collecting the XRD spectrum for a strain free corundum sample with a large grain size. Modified Williamson Hall technique [17-21] was employed for the determination of matrix crystallite size, strain and dislocation density and Williamson Hall technique was adopted for determination of $ZrO_2$ crystallite size.

Further Synchrotron XRD measurements were carried out on annealed powder samples of model ODS and $ZrO_2$ dispersed steel powder. The high brilliance of synchrotron source compared to conventional source and superior signal to noise ratio is been exploited for identification of minor phases in the material. Well ground powders were used and measurements were recorded in transmission geometry at ambient temperature and pressure using synchrotron facility at extreme conditions XRD beamline (BL-11), Indus-2, RRCAT [22], Indore, India. For this purpose, the angle dispersive mode with a wavelength, $\lambda = 0.44092$ Å is used. A MAR345 imaging plate system was used and this image plate data was further processed with an automated software FIT2D [23] by integrating over full circle, to obtain the 2 dimensional XRD data. The center of the pattern has been fixed carefully to minimize the possible error. The calibration of the X-ray photon energy and the distance between the sample and the image plate was carried out by using standard $LaB_6$ and $CeO_2$ samples. The Phase identification was carried out by comparison with ICDD card, within a $\Delta\theta$ ($\theta$ observed-$\theta$ expected) of 0.2°. The phase analysis by Rietveld refinement was carried out using GSAS without any internal calibrant. The raw data was processed in three steps involving, background subtraction, normalizing the counts and multiplication by a common factor.

### 2.3.5 Thermal analysis through Differential Scanning Calorimetry

DSC is a thermo-analytical technique which measures the difference in heat flow between the sample and a reference material (empty alumina crucible), when both are heated or cooled at a preset heating or cooling rate [24]. The absorption or evolution of heat due to a thermal event will then result in a change in the differential heat flow between the sample and reference, which appears as a peak in the DSC thermogram. The analysis of the DSC thermogram involves carefully analyzing this DSC peak and understanding the thermal event responsible for it.

In the present study, thermal characterization of 100h ball milled sample was carried out in a SetaramSetsys16 heat flux type differential scanning calorimeter. DSC experiments were performed by using 10K $min^{-1}$ heating rate up to 1473 K, held for 15 min and subsequently cooled at a rate of 10K $min^{-1}$ (Run-1). In order to distinctly identify the nature of phase transformation, the DSC experiment was repeated on the same sample under identical experimental conditions (Run-2). Further, study of transformation kinetics was carried out by another set of DSC experiments using different heating rates of 3, 10, 30, 50, and 70 K min$^{-1}$ followed by cooling at the rate of 90 K min$^{-1}$. It is required to mention here that the temperature calibration was carried out using the Al, Cu standards and heat flow calibration was carried out with reference to the polymorphic transitions in pure iron (99.999 %).

### 2.3.6 Hardness Measurements

Hardness refers to the resistance of a material to plastic deformation, usually by indentation. With greater hardness, the material shows a greater resistance to deformation. Hardness measurement gives a preliminary idea about the mechanical property of a material with a quick and simple measurement from a small sample.

For the body of work given in this thesis, the Vickers hardness tests were performed using a Leitz micro-hardness tester with an applied load of 100 g. Repeated hardness tests were performed on the specimen (~ 20 trials per reading) within the samples with a careful selection of locations to avoid influences of the plastic zone. The dwell time of 15 seconds for each indent was concurrent with ASTM standards.

The nano-indentation was performed in the current study on ball milled model ODS powder samples. For this, the powder particles which were embedded in epoxy glue (as explained in section 2.5) were polished to get a flat and scratch free surface. The nano-hardness measurements on the powder particles were carried out in a nano-indenter (M/s CSM, Switzerland) equipped with a three sided pyramidal diamond (Berkovich) tip with an end radius of ~ 30 nm. Loading and unloading rates were maintained at 20 mN min$^{-1}$ and indentation was carried out for a fixed depth of 200 nm. At least 20 indentations were carried out on each sample and the average value of the hardness is measured after ignoring the erroneous readings. The measurements were carried out on the powder milled for different durations and hardness value as a function of milling time is analyzed.

### 2.3.7 Electron Back Scattered Diffraction

EBSD is a SEM based quantitative microstructural analysis technique extensively utilized in the materials development for obtaining crystallographic information about the microstructure of a sample. Here, a stationary electron beam is made to interact with a tilted crystalline sample (~ 70$^{o}$ with the horizontal) and subsequently the diffracted electrons form a pattern that can be detected with a fluorescent screen, as shown schematically below in figure 2.5.

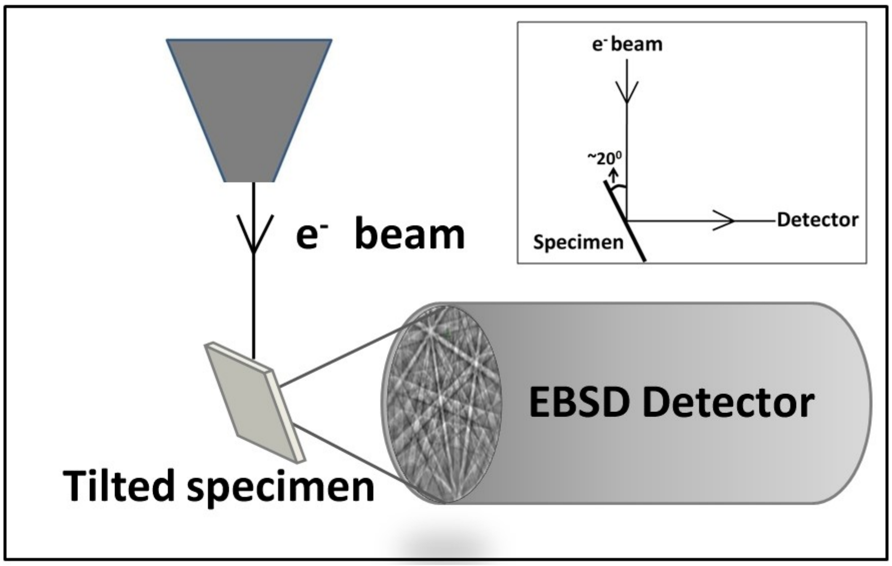

**Figure 2.5: A schematic of EBSD experimental set up**

The diffraction pattern of material is characteristic of the crystal structure and orientation in the region in the material, from where it was generated. Hence the diffraction pattern can be used to determine the crystal orientation, distinguish between crystallographically different phases, characterize grain boundaries, and provide information about the local crystallinity [25]. The mechanical and physical properties of metallic materials are often related to grain size and EBSD is an ideal technique for characterizing the same [26].

In the present study, EBSD analysis is carried out in FEI make Helios Nanolab 600i SEM attached with a Hikari camera for detection of Kikuchi patterns. The scanned data was then analyzed using TSL software. The EBSD studies were carried out at an accelerating voltage of 20 kV and electron beam current of 2.7 nA. A step size of 0.05 μm was used at 8000X magnification. The specimen preparation includes, fine polishing of the sample with SiC grit and diamond polish, followed with electro polishing using 10% percholoric acid solution.

## 2.4 Summary

A comprehensive description of alloy synthesis, heat treatments and their microstructural and microchemical characterizations has been given in the present chapter. Brief descriptions of all the techniques used in the present thesis, their principle and relevance to the context of the current study are also mentioned. The following Table 2.3 gives a summary of all the characterization tools utilized in the thesis.

**Table 2.3: Summary of all the techniques employed in the current study**

| Technique | Instrument | Operating conditions | Measurement performed |
|---|---|---|---|
| **Scanning Electron Microscopy** | Helios Nanolab 600i | Operated at 5-30 kV, depending on the problem at hand.<br>(SE and BSE detector) | Microstructural and microchemical characterization |
| **Transmission Electron Microscopy** | Philips CM 200<br>Tecnai F30 | Operated at 200 kV<br>Operated at 300 kV | |
| **Focused Ion Beam in SEM** | Helios Nanolab 600i | Operated at various kV and Currents depending on the requirement | Subsurface microstructure analysis and preparation of TEM lamellae |
| **X-ray Diffraction** | Bruker AXS D8 discover | $\theta$ range: 15° - 105°<br>Co K$\alpha$ radiation,<br>$\lambda$ = 1.78896 Å | Phase identification and Micro strain Analysis |
| | Synchrotron facility at RRCAT Indore, BL 11 | $\theta$ range: 5° - 35°<br>$\lambda$ = 0.44092 Å | |
| **Hardness** | LeitzVickers hardness tester | Load 100 g for 15 sec. | Vickers hardness number |
| | Nanoindenter (M/s CSM, Switzerland) | Force : 20 mN min$^{-1}$<br>Depth : 200 nm | Nanohardness of powder particles |
| **Differential Scanning Calorimetry** | Setaram® Setsys 1600heat flux DSC | Various Heating / cooling rates as mentioned in the respective chapters | Transformation temperature and enthalpy |
| **Spark Plasma Sintering** | Dr. Sinter | Temperature: 1323 K<br>Pressure 50 MPa<br>Hold time: 10 minutes<br>Heating rate: 100K/min | Powder consolidation |

## 2.5 References

1. Suryanarayana, C., *Mechanical Alloying And Milling*. Taylor & Francis: 2004
2. Suryanarayana, C., *Progress in Materials Science* (2001) 46 (1–2), 1
3. C. Suryanarayana, E. I., V.V. Boldyrev, *Materials Science and Engineering A* (2001), 151
4. Murty, B., and Ranganathan, S., *International materials reviews* (1998) 43 (3), 101
5. Munir, Z. A*., et al.*, *Journal of the American Ceramic Society* (2011) 94 (1), 1
6. Staltsov, M. S*., et al.*, *Nuclear Materials and Energy* (2016) 9, 360
7. Hu, J., Grain Growth by Ordered Coalescence of Nanocrystals in Ceramics. Stockholm University, Stockholm, Sweden, 2013
8. Zhang, H*., et al.*, *Journal of Nuclear Materials* (2015) 464, 61
9. Giannuzzi, L. A*., et al.*, *Microscopy and Microanalysis* (2005) 9 (S02), 1572
10. D. V. Sridhara Rao, K. M., and C. J. Humphreys, *Microscopy: Science, Technology, Applications and Education*, Díaz, A. M.-V. a. J., (ed.) Formatex Research Center, Badajoz, Spain, (2010), Vol. 2, pp 1232
11. Jacques, G., *Semiconductor Science and Technology* (2009) 24 (4), 043001
12. Melngailis, J., *Journal of Vacuum Science & Technology B: Microelectronics Processing and Phenomena* (1987) 5 (2), 469
13. Reichelt, R., Scanning Electron Microscopy. In *Science of Microscopy*, Hawkes, P. W., and Spence, J. C. H., (eds.) Springer New York, New York, NY, (2007), pp 133

14. Goldstein, J., *Scanning Electron Microscopy and X-ray Microanalysis: Third Edition*. Springer US: 2003

15. https://imagej.nih.gov/ij/,

16. https://imagej.net/Particle_Analysis.

17. Ungár, T*., et al.*, *Acta Materialia* (1998) 46 (10), 3693

18. Ungár, T., and Tichy, G., *physica status solidi (a)* (1999) 171 (2), 425

19. Ungár, T., and Borbély, A., *Applied Physics Letters* (1996) 69 (21), 3173

20. Ungar, T., *Advances in X-ray Analysis (AXA) - the proceedings of the Denver X-ray Conferences*, JCPDS - International Centre for Diffraction Data (1996), Vol. 40

21. Ribárik, G., Modeling of diffraction patterns based on microstructural properties. Eötvös Loránd University, Budapest, Hungary, 2008

22. Pandey, K*., et al.*, *Pramana* (2013) 80 (4), 607

23. http://www.esrf.eu/computing/scientific/FIT2D/.

24. Höhne, G*., et al.*, *Differential Scanning Calorimetry*. Springer: 2003

25. Oxford, http://www.ebsd.com/introduction.

26. Suwas, S., and Gurao, N. P., *Journal of the Indian Institute of Science* (2008) 88

Chapter IV

# Thermal evolution of nanocrystalline Fe – 15 Wt. % $ZrO_2$ model alloy

## 4.1 Introduction

The milling characteristics of Fe – 15 Wt. % $ZrO_2$ powders were described in detail in chapter III and the study resulted in optimized duration of ball milling for the synthesis of powders based on its microstructure and chemical homogeneity. But for any engineering application the powder needs to be compacted to the desirable shape and hence it is an important step in material development. This conventionally involves exposure of the powder to high temperature and pressure, wherein the non-equilibrium structure relaxes by release of excess strain energy at high temperatures. Consequently, there is a possibility that the material might lose its nc structure owing to grain growth. Hence, the properties of the consolidated material are dependent upon the structural and chemical evolution during high temperature / pressure exposure. For example, the formation of intermetallics, precipitates and other transformation products at high temperature play a key role in governing the final microstructure and thus the mechanical properties of the material. The stability of these intermetallics or precipitates is usually known to determine the temperature limit to which the material can be exposed [1]. Hence, thermal evolution is an important aspect in determining the process parameters in manufacturing as well as in-service operation. Further, as the material derives its strength from the finely dispersed oxides, their stability in terms of chemistry and size at high temperature is the key factor in determining the material's high temperature strength. Grain growth of dispersoids at high temperatures is almost inevitable but its rate would be intriguing to investigate. Keeping in sight of all these, thermal evolution of Fe – 15 Wt. % $ZrO_2$ model alloy system has been taken up and reported here in this chapter. Section 4.2 gives a brief introduction to the Phase evolution in Fe – 15 Wt. % $ZrO_2$ model alloy system and underlines the methodology adopted. Section 4.2.1 describes the results of analysis of DSC thermogram and lists the important transformations observed during the DSC analysis. Further section 4.2.2 assigns the DSC thermogram peaks to the possible transformation reactions and summarizes the results obtained from the DSC analysis. Section 4.2.3 presents a detailed explanation on the structural analysis of the thermally treated powder for identification of phase transformations in the system. Rigorous XRD analysis is carried out and microscopic evidences are provided for the same. Section 4.3 summarizes the results on X-ray Phase analysis through Rietveld method and discussion is made about the phase fractions. Section 4.4 describes the modeling of phase formation and also discusses the Kinetics of FeO phase formation by adopting KJMA analysis. The crystallite size evolution of $ZrO_2$ with time and temperature is discussed in section 4.5. The section 4.5.1details about the determination of crystallite size by XRD followed by determination of crystallite size by TEM in Section 4.5.2. Section 4.6 discusses the kinetics of grain growth by Ostwald ripening model and discusses the activation energy for grain growth. The chapter concludes with summary of important results in section 4.7.

## 4.2 Phase Evolution of Fe - 15 Wt. % $ZrO_2$ model alloy

For the reasons discussed earlier, the study of evolution of phases in the Fe - 15 Wt. % $ZrO_2$ system as a function of temperature has been studied through careful analysis of the DSC thermogram supported by structural studies using synchrotron

XRD and TEM. DSC experiments were performed by using 10K min$^{-1}$ heating rate up to 1473 K, held for 15 min and subsequently cooled at a rate of 10K min$^{-1}$ (Run-1). In order to distinctly identify the nature of phase transformation, the DSC experiment was repeated on the same sample under identical experimental conditions (Run-2). Further, study of transformation kinetics was carried out by another set of DSC experiments using different heating rates of 3, 10, 30, 50, and 70 K min$^{-1}$ followed by cooling at the rate of 90 K min$^{-1}$. These results are discussed below.

### 4.2.1Analysis of DSC thermogram

Figure 4.1(a) depicts the DSC thermogram of Run-1 which has been carried out at 10K min$^{-1}$ heating and cooling rate. The heat flux profile in figure 4.1(a) shows two sharp endothermic peaks at 854 K and 1023 K during heating. A magnified heat flux profile for the heating cycle is shown in figure 4.1(b). Careful analysis of this heat flux profile reveals two relatively broad endothermic peaks centered around 1140 and 1172 K. All the 4 peaks at 854, 1023, 1140 and 1172 K are marked as 1, 2, 3 and 4 in figure 4.1(a) and (b). The cooling profile in figure 4.1(a) shows three sharp exothermic peaks at 1154, 1136 and 1023 K, which are complementary to 4, 3 and 2 respectively of the heating profile. The deviations in the transition points in heating and cooling profiles could be due to superheating and supercooling, respectively. The heat flux profile of Run-2, which was carried out under identical experimental conditions as Run-1, is shown in figure 4.1(c). The thermogram shows three endothermic peaks at 1023, 1144 and 1178 K, marked as 2, 3 and 4, respectively. The cooling profile of Run-2 shows three exothermic peaks at 1151, 1137 and 1023 K, marked as 4, 3 and 2, respectively. These peak positions are listed in Table 4.1.

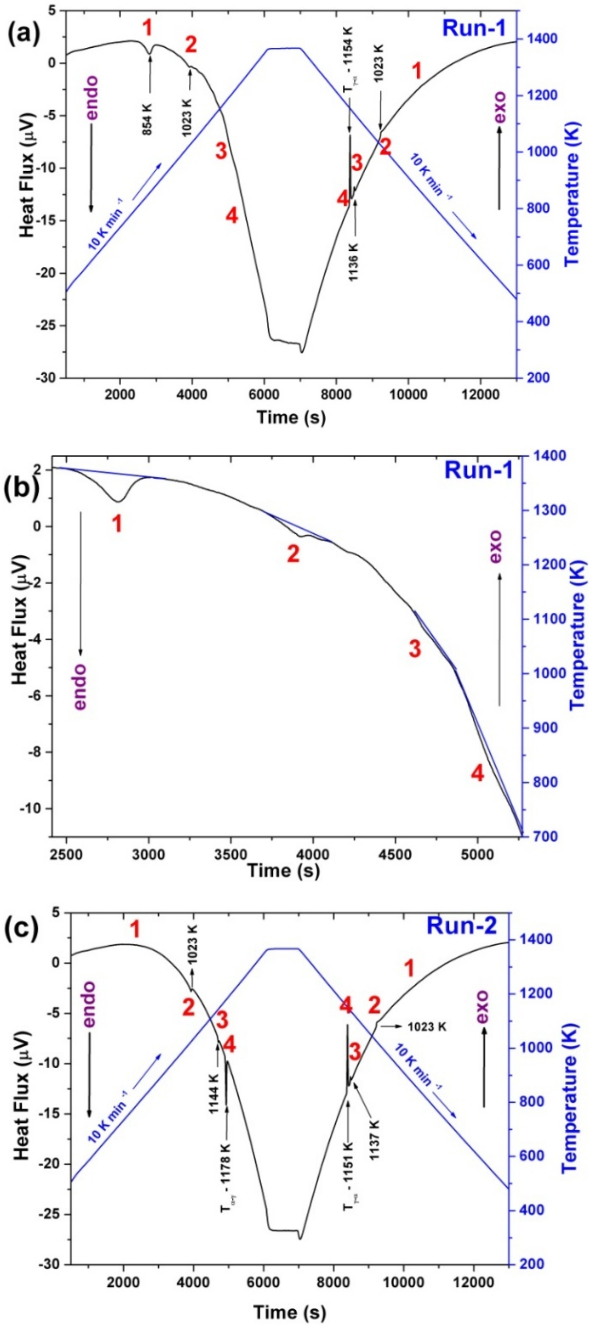

Figure 4.1: DSC run on 100h milled sample at 10 K min$^{-1}$ rate (a) Run-1 (b) Part of Run-1 magnified (c) Run-2 on the same sample

**Table 4.1: Summary of the peak positions in the DSC Run-1 and Run-2**

| *Peak No.* | *DSC peak positions in (K)* | *Run-1* | | *Run-2* | |
|---|---|---|---|---|---|
| | | *Heating* | *Cooling* | *Heating* | *Cooling* |
| 1 | 854 | ✓ | ✗ | ✗ | ✗ |
| 2 | 1023 | ✓ | ✓ | ✓ | ✓ |
| 3 | 1140 / 1136 / 1144 / 1137 | ✓ | ✓ | ✓ | ✓ |
| 4 | 1172 / 1154/ 1178 / 1151 | ✓ | ✓ | ✓ | ✓ |

### 4.2.2 Assignment of the DSC thermogram peaks

It is observed from Table 4.1 that the endothermic peak #1 at 854 K is present only in the heating profile of Run-1. Being an endothermic peak in the heating profile, the peak is attributed to an irreversible transformation process and needs further investigation, the results of which is discussed in the subsequent sections.

The peak #2 at 1023 K is reproducible during both the heating and cooling cycles of both Run-1 and Run-2. The peak is attributed to the Curie transition point of α-Fe [2]. Ideally, the peak should have appeared at 1043 K [3] for pure Fe, which is reduced by 20 K in the present case. A change in Curie temperature can be caused by size effects, internal stresses [4] or even by the presence of secondary particles in a composite [5]. Since both the runs have exhibited identical Curie temperatures, the size and stress effects are not manifested in the measurement. Hence, the reduction in Curie temperature is attributed to the presence of $ZrO_2$ dispersoids.

The peak #3 appears at 1140 and 1144 K in the heating profiles of Run-1 and Run-2, respectively and at 1136 and 1137 K in the cooling profiles of Run-1 and Run-2, respectively. These peaks do not correspond to any known transformations of Fe or monoclinic $ZrO_2$ and will be discussed subsequently in conjunction with the XRD and TEM results.

The peak #4 is observed at 1172 and 1178 K in the heating profiles and 1154 and 1151 K in the cooling profiles of Run-1 and Run-2, respectively. The peak clearly corresponds to α (bcc) ⇆γ (fcc) of Fe. Ideally, a sharp peak is expected at 1183 K for this transformation. However, the peak in the heating profile of Run-1 exhibits a large FWHM, which is dealt with in detail discussion in the following section.

### 4.2.3 Structural analysis for identification of phase transformations

As discussed earlier, the most intriguing phase transformations correspond to the peaks #1 and #3, both of which are observed to be endothermic in the heating cycle. Synchrotron XRD and analytical TEM studies have been carried out to understand these transformations. Figure 4.2(a) shows the synchrotron XRD patterns in the 2θ range from $3^o$- $36^o$ for the as milled powder, samples post Run-2 in DSC (hereafter referred as, DSC-2) as well as those annealed at 723 and 923 K.

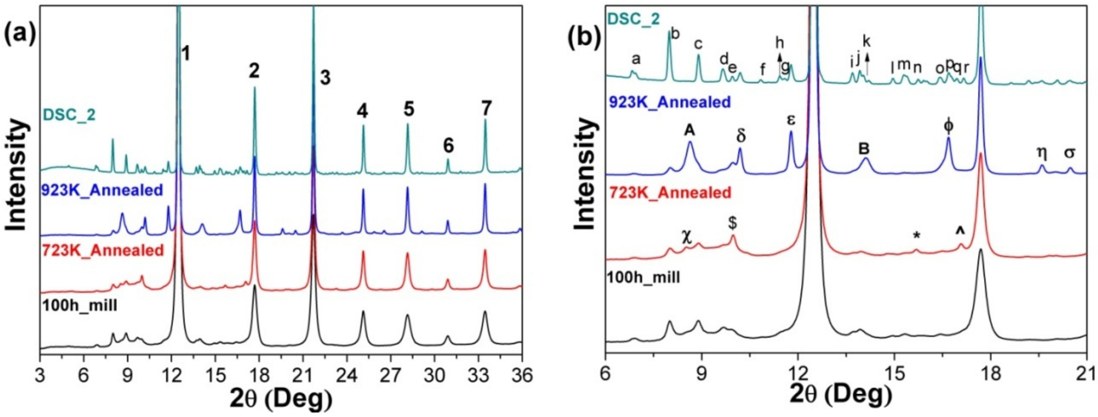

**Figure 4.2: (a) XRD results on the as milled and annealed powder samples (b) Part of the spectrum magnified**

While the XRD of the as milled powder is included for comparison purposes, those from samples annealed at 723 and 923 K have been selected, as these temperatures precede and follow the endothermic peak #1 at 854 K. Since peak #3, centered at 1140 K, appears both during heating and cooling profiles in all DSC experiments, it can be associated with a reproducible transformation of a phase, which needs to be identified. Hence, analysis of the XRD pattern from DSC-2 sample has been used to unearth the unknown phase. While most of the higher angle XRD peaks are sparsely spaced and relatively easy to identify, the ones in the range $6^o$– $21^o$ are rather closely spaced. Hence, figure 4.2(b) depicts the X-ray diffractogram in this range.

Table 4.2 summarizes the XRD peaks observed in figure 4.2(a) and 4.2(b). Peaks marked 1 to 7, correspond to the bcc phase of Fe (ICDD: 00-006-0696) while those marked ‘a’ to ‘r’ correspond to the monoclinic phase of $ZrO_2$ (ICDD: 00-036-0420). In addition to these peaks, which are present in the as milled as well as annealed powders, additional peaks marked as $\chi$, \$, * and $\Lambda$ are present in the sample annealed up to 723K while peaks marked A, B, $\delta$, $\varepsilon$, $\Phi$, $\eta$ and $\sigma$, are present in the sample annealed at 923K .

It is observed that the FWHM of peaks reduce on annealing indicating strain reduction and / or grain growth. Careful investigation of the peaks marked $\chi$, \$, * and $\Lambda$ reveals that they belong to the cubic $Fe_3O_4$ phase (ICDD: 00-019-0629). $Fe_3O_4$, which is absent in the as-milled powder, is expected to have formed at temperatures below 723 K by means of a reaction with residual Oxygen that is picked up during prolonged duration of ball milling, as have been reported in the literature [36,37]. This is in spite of milling in 5N pure Ar atmosphere. The Fe, residual O reaction is believed to be aided by nanocrystallinity of Fe [14].

The peaks marked δ, ε, Φ, η and σ in 923 K annealed sample are found to correspond to the FeO phase (ICDD: 01-089-0687). There was no evidence for the presence of $Fe_3O_4$ phase in the 923 K sample. From these results, it is inferred that peak #1 corresponds to FeO, which forms as a result of a chemical reaction involving $Fe_3O_4$. This is also supported by literature where Bonetti et al.[6], have reported the following eutectoid reaction at 843 K during ball milling of Fe/$Fe_3O_4$ nanocomposite system:

$$Fe + Fe_3O_4 \rightarrow FeO \tag{4.1}$$

FeO, which is also known as the wüstite phase, could be a non-stoichiometric oxide, $Fe_{1-x}O$, with "x" ranging from 0.05 to 0.17 [7]. It is a metal deficient oxide which is also found in the earth's core. It has attracted significant attention due to the complex defect structure of its pseudo phases, different from the conventional non stoichiometric oxides [8]. The phase is stable as it is present even in the DSC-2 sample. In fact, dispersion strengthening of Fe alloys by FeO has been reported in the literature [9].

**Table 4.2 : Summary of peaks identified from Figure 4.2**

| | | | | | | | | **Fig. No.** |
|---|---|---|---|---|---|---|---|---|
| **Fe (ICDD: 00-006-0696)** | **1**:(110) | **2**:(200) | **3**:(211) | **4**:(220) | **5**:(310) | **6**:(222) | **7**:(321) | 4.2(a) |
| **Monoclinic $ZrO_2$ (ICDD:00-036-0420)** | **a**:(011) | **b**:$(\bar{1}11)$ | **c**:(111) | **d**:(002) | **e**:(200) | **f**:(021) | **g**:$(\bar{2}11)$ | 4.2(b) |
| | **h**:$(\bar{1}21)$ | **i**:(022) | **j**:$(\bar{2}20)$ | **k**:$(\bar{1}22)$ | **l**:$(\bar{2}21)$ | **m**:(202) | **n**:$(\bar{1}13)$ | 4.2(b) |
| | **o**:(212) | **p**:(131) | **q**:$(\bar{2}13)$ | **r**:(311) | | | | 4.2(b) |
| **Cubic $Zr_{0.9}Fe_{0.1}O_{1.95}$ (ICDD:04-008-4173)** | **A**:(111) | **B**:(220) | | | | | | 4.2(b) |
| **$Fe_3O_4$ (ICDD:00-019-0629)** | **χ**:(220) | **$**:(311) | *****:(511) | **^**:(440) | | | | 4.2(b) |
| **FeO (ICDD:01-089-0687)** | **δ**:(111) | **ε**:(200) | **Φ**:(220) | **η**:(311) | **σ**:(222) | | | 4.2(b) |

Additional diffraction peaks observed in the 923 K annealed sample are marked 'A' and 'B', in figure 4.2(b). These peaks are identified using the ICDD Data card 04-

008-4173 as cubic $ZrO_2$ with a stoichiometry of $Zr_{0.9}O_{1.95}Fe_{0.1}$. This cubic phase can also be denoted as $Zr(Fe)O_2$ as reported by Bechta et al.[10], where the stability of this phase is derived from the dissolution of FeO in $ZrO_2$. However, the phase does not appear to be stable at high temperature, as the corresponding peaks are absent in DSC-2 sample, instead strong reflections of monoclinic $ZrO_2$ are observed.

On the other hand, peak #3 (1140 K) appears in all the thermal cycles indicating that it corresponds to the transformation of a persistent phase present in the material. Based on the results presented so far, the α-Fe, monoclinic $ZrO_2$, FeO and cubic $ZrO_2$ ($Zr_{0.9}O_{1.95}Fe_{0.1}$) phases have been unambiguously identified. Interestingly, there are no known transformations in the α-Fe, monoclinic $ZrO_2$ and FeO phases around this temperature of 1140 K. However, literature[10, 11] does hint at a possible phase transformation of cubic $ZrO_2$ close to this temperature. Jiang et al. [11] while carrying out in situ high temperature XRD experiments observed a cubic → tetragonal transformation in nanostructured Fe doped monoclinic $ZrO_2$ at 1100 K. This transformation temperature has been reported to be a function of the dopant concentration [12]. In line with these discussions, the peak #3 is attributed to the cubic to tetragonal transformation and vice versa of the FeO stabilized cubic $ZrO_2$ phase, during the heating and cooling profiles of DSC experiments, respectively.

The peak #4 (1173 K) is attributed to the α (bcc) $\leftrightarrows$γ (fcc) of Fe, but it was observed that the heating cycle in Run-1 showed a rather weak and broad peak while sharp transitions were observed during cooling in Run-1 as well as Run-2, in DSC experiments. Similarly, XRD analysis showed a rather broad FWHM corresponding to α-Fe peaks for samples annealed at 723 and 923 K, closely resembling the milled powder sample, while the DSC-2 sample showed very sharp peaks, indicating growth of crystallites after the Run-1 heating cycle. Scherrer analysis of the α-Fe peaks, showed that the average crystallite size measured 12 and 18 nm in the samples annealed at 723 and 923 K respectively. The sizes are comparable to 10 nm measured in the as-milled sample, as reported earlier [13]. However, sharpness of the α-Fe peaks in the DSC-2 sample, indicate significant increase in crystal size. Hence no attempt was made to calculate the crystallite size through XRD, knowing its inherent shortcomings [14].

In order to obtain confirmatory evidence for the presence of various phases observed during the DSC experiment, detailed TEM studies were also carried out. Figure 4.3(a) shows the BF micrograph of the sample annealed at 723 K. Diffraction contrast in the micrograph reveals a distribution of nanocrystallites. SAED pattern obtained from a large area using a 10 μm aperture is shown in Fig. 4.3(b). It reflects the polycrystalline nature of the sample with characteristic ring pattern. The rings are assigned to phases using symbols listed in Table 4.2. Fe, monoclinic $ZrO_2$ and $Fe_3O_4$ phases have been identified. A crystallite marked by a circle in Fig. 4.3(a) has been analyzed by micro-diffraction technique and the diffractogram is shown in figure 4.3(c). Analysis of the diffractogram reveals that this crystallite corresponds to $Fe_3O_4$ phase along $<\bar{1}11>$ zone axis. This finding further confirms the XRD evidence for presence of $Fe_3O_4$ in the sample annealed at a temperature prior to peak #1 (723 K).

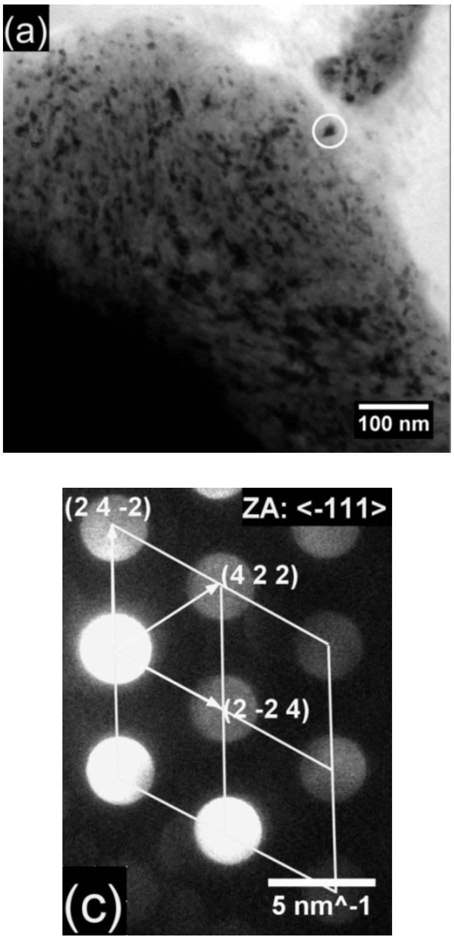

**Figure 4.3:(a) BF micrograph of sample annealed up to 723 K showing $Fe_3O_4$ crystallites marked in a circle. (b) is the SAED Pattern from the region shown in (a). Figure (c) shows themicro diffraction pattern obtained from a $Fe_3O_4$ crystallite**

Figure 4.4(a) shows the BF micrograph of the sample annealed at 923 K. Diffraction contrast in the micrograph reveals a nc microstructure. Figure 4.4(b) shows the SAED pattern obtained using a 10 μm aperture which shows a ring pattern characteristic of the polycrystalline nature of the sample. The rings are marked in accordance to the phases using the symbols listed in Table 4.2. Fe, monoclinic $ZrO_2$, cubic $ZrO_2$ and FeO phases have been identified. Using micro-diffraction technique the crystallite circled in figure 4.4(a) has been examined and shown in figure 4.4(c), which is analyzed as FeO phase along <111> zone axis. This provides confirmatory evidence for the XRD results on the presence of FeO in the sample annealed at 923 K, which arises due to the reduction of $Fe_3O_4$ phase, as discussed earlier. The EDS result from this crystallite is shown in figure 4.4(d) and its inset shows the average elemental composition as, Fe – 48.75 at. % and O – 51.25 at. %. The stoichiometry also is in agreement with the formation of FeO phase. It may be recalled that the cubic $ZrO_2$ ($Zr_{0.9}Fe_{0.1}O_{1.95}$) phase was identified from the XRD in figure 4.2(b). Reflections corresponding to (111) and (220) of the cubic $ZrO_2$ have also been identified in the SAED pattern. A DF micrograph using the relatively more intense (111) reflection of cubic $ZrO_2$ is shown in figure 4.4(e). The micrograph shows that, the cubic $ZrO_2$ crystallites measure ~ 10 - 15 nm in this sample. Peak #4 was reanalyzed using TEM and XRD.

Figure 4.5(a) shows the TEM DF micrograph taken using the (110) reflection of α-Fe for 923 K annealed sample. This is in support of the Scherrer analysis showing nc nature of α-Fe at 923 K. However, for an unambiguous confirmation of nanocrystallinity as the cause for the broad and weak peak during Run-1, it was essential to investigate the size of α-Fe grains just before the start of the $\alpha\rightarrow\gamma$ transformation, i.e. 1073 K. Figure 4.5(b) shows the TEM DF micrograph of the sample using the (100) reflections of α-Fe annealed at 1073 K. The distribution of crystallite size at 923 and 1073 K are shown in figure 4.5(c). It is observed that the distributions are comparable and the sizes vary in the range, 3– 80 nm. The values are in good agreement with the XRD results and confirm that Fe remains in NC until the onset of $\alpha \rightarrow \gamma$ phase transformation. Figure 4.5(d) shows the SEM micrograph of the powder after annealing at 1473 K for 15 minutes, which simulates the end of heating cycle of the DSC experiment during Run - 1. The micrograph and its inset clearly show large grains of Fe, in agreement with the sharp XRD peaks obtained for α-Fe, earlier. These grains are indicated by arrows in this figure. The grains measure as much as ~ 5–15 μm.

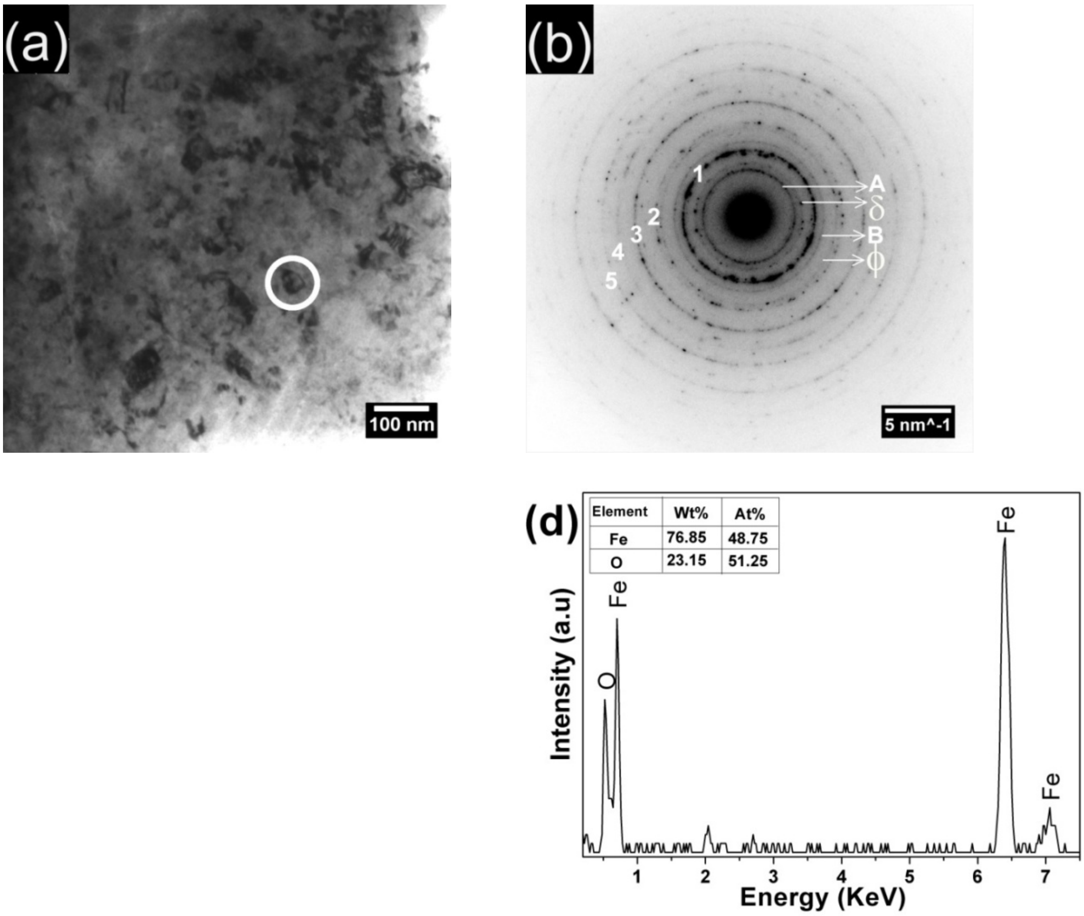

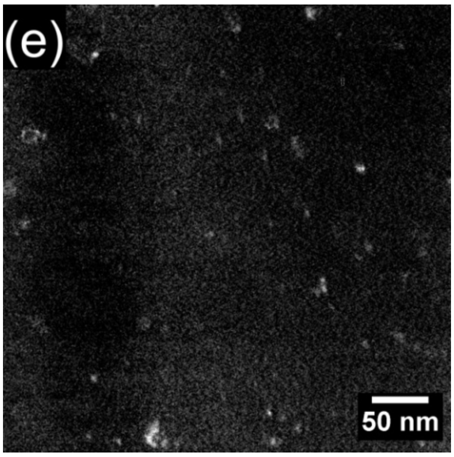

**Figure 4.4: (a): BF micrograph of the sample annealed at 973 K showing nano-crystallites. FeO crystallite is marked in a circle. (b): SAED pattern from the region shown in figure (a). Figure (c) shows micro-diffraction patterns from FeO crystallite. (d): EDS results from the FeO crystallite, showing the microchemistry. (e): DF micrograph from the (111) reflections of Cubic ZrO2, showing tiny crystallites**

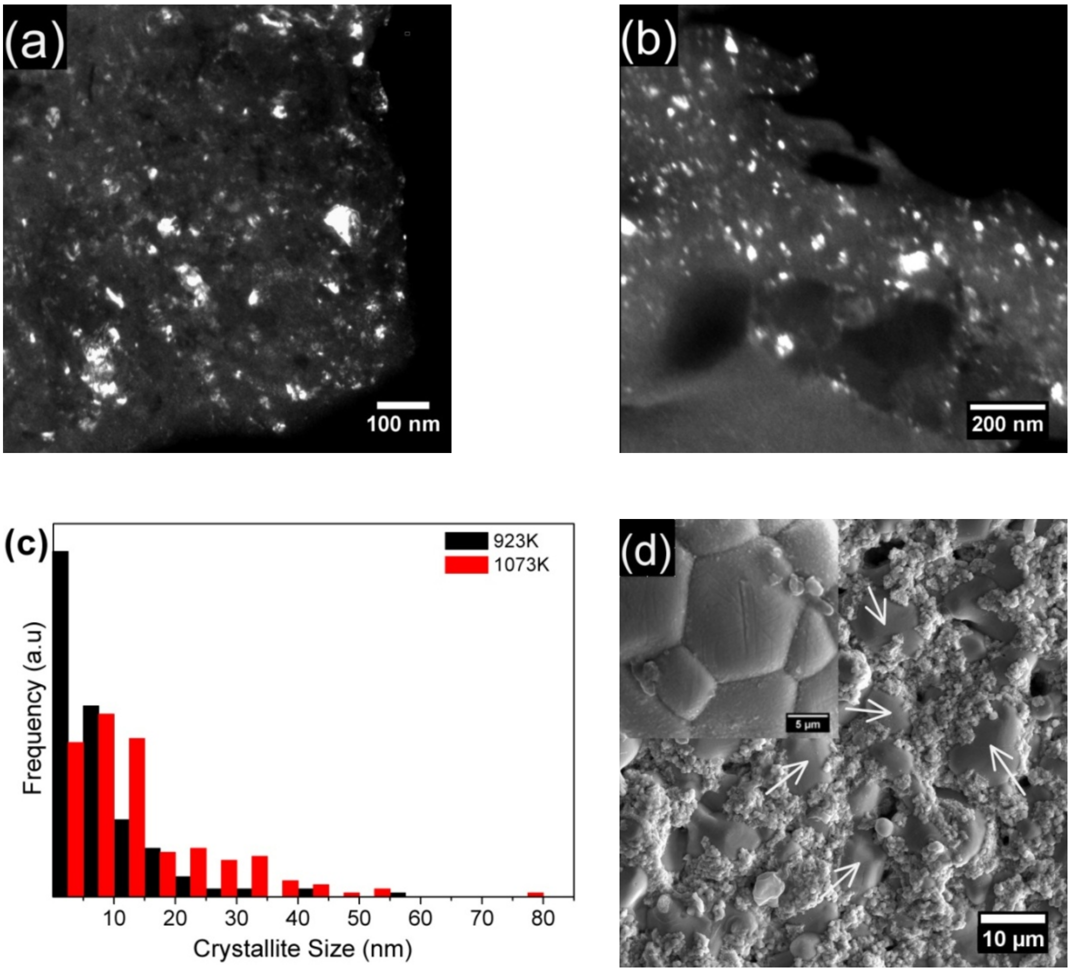

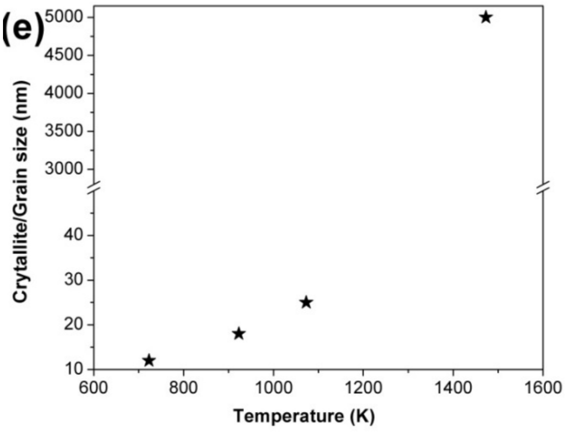

**Figure 4.5: DF-TEM micrograph from (110) reflections of Fe,for sample annealed at (a) 923K and at (b) 1073 K. Figure (c) is the crystallite size distribution analyzed from figure (a) and (b). SEM micrograph of sample annealed at 1473 K for 15 min is shown in (d) with arrows indicating the large Fe grains which is also shown in the inset. Figure (e) is the graph of Fe crystallite /grain size Vs Temperature for the sample annealed at 723 K, 923 K, 1073 K and 1473 K**

Figure 4.5(e) is a plot of bcc - Fe crystallite/grain size at different annealing temperatures. It is well known that strain energy, grain size and interfacial energy play important roles in phase transformations and phase stability in nc materials [15]. The rapid growth of the crystallites at the end of the heating profile of Run-1 is a testimony for the sharp α⇆γ in the subsequent DSC runs. In other words, it is confirmed beyond doubt that nanocrystallinity of the α-Fe grains is responsible for the broad transformation peak in DSC. Such a DSC thermogram behavior has also been reported for fine grained (~ 23 nm) Co [16]. The sequence of phase evolution in the Fe – 15 Wt. % $ZrO_2$ composite is summarized schematically as shown in figure 4.6.

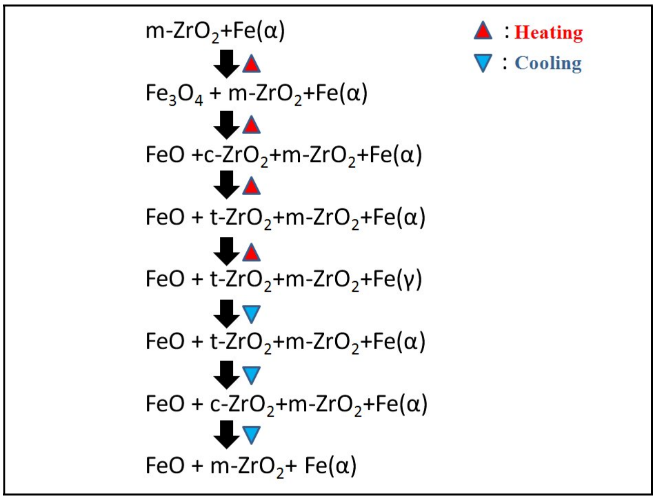

**4.6: Schematic of the transformation of phases with thermal treatment in Fe – 15 Wt.% $ZrO_2$ system**

## 4.3 X-ray Phase analysis by Rietveld method

The structural analysis discussed so far has established the phases and their thermal evolution. In order to qualitatively analyze the phase fractions and the lattice structure, Rietveld refinement was carried out on XRD data from 923 K annealed and DSC_2 samples. However, it is necessary to note here that the analyses have been carried out without an internal calibrant. In other words, the estimated phase fractions are only qualitative in nature. Accordingly, figure 4.7 (a) and 4.7(b) show the results of Rietveld analysis on 923 K annealed and DSC_2 samples respectively. The graph also shows the measured weight fractions of each phases and lattice parameters for these phases as an inset. Along with this, the fit parameters are also mentioned.

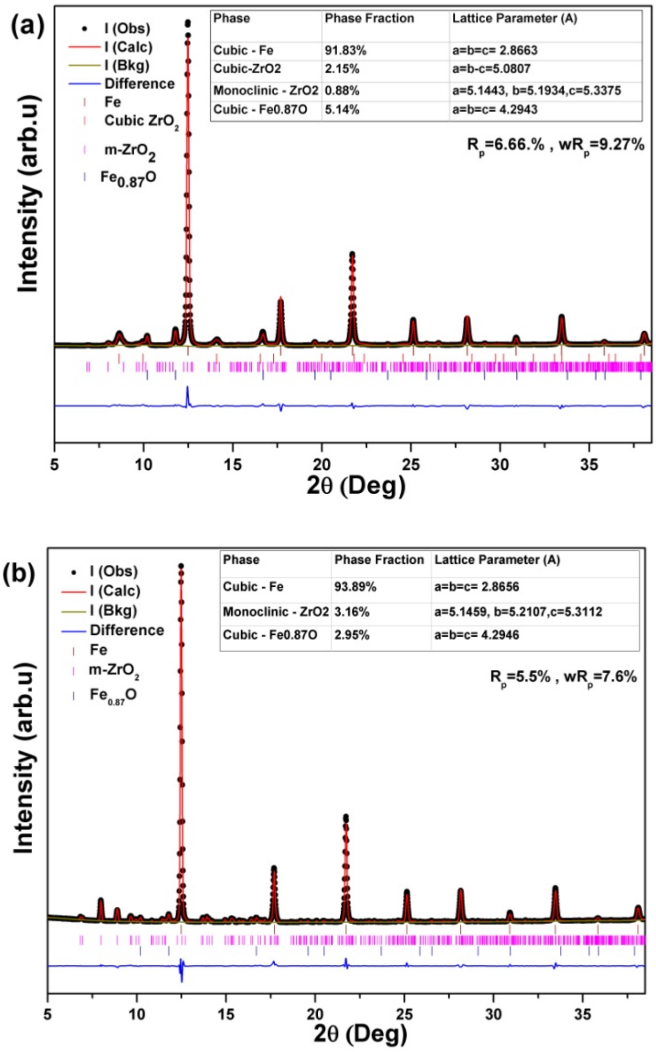

| Phase | Phase Fraction | Lattice Parameter (A) |
|---|---|---|
| Cubic - Fe | 91.83% | a=b=c= 2.8663 |
| Cubic-ZrO2 | 2.15% | a=b-c=5.0807 |
| Monoclinic - ZrO2 | 0.88% | a=5.1443, b=5.1934,c=5.3375 |
| Cubic - Fe0.87O | 5.14% | a=b=c= 4.2943 |

$R_p$=6.66.% , $wR_p$=9.27%

| Phase | Phase Fraction | Lattice Parameter (A) |
|---|---|---|
| Cubic - Fe | 93.89% | a=b=c= 2.8656 |
| Monoclinic - ZrO2 | 3.16% | a=5.1459, b=5.2107,c=5.3112 |
| Cubic - Fe0.87O | 2.95% | a=b=c= 4.2946 |

$R_p$=5.5% , $wR_p$=7.6%

**Figure 4.7: Rietveld refined Synchrotron XRD data for (a) 923 K annealed and (b) DSC_2 samples, showing the calculated (line), observed (dot) and difference between the two**

From the analyses, the stoichiometry of FeO phase present in either sample could be ascertained to be $Fe_{0.87}O$, which indicates the metal deficient nature of this oxide. A similar non-stoichiometric iron oxide is reported in case of a ball milled Fe,

$Fe\text{-}Y_2O_3$ and $Fe\text{-}Y_2O_3\text{-}Ti$ system also [17]. The measured lattice parameter of $Fe_{0.87}O$ is 4.2946(2) Å, which is slightly lower than 4.326(2) Å for stoichiometric FeO (ICDD: 01-089-0687). It is interesting to note that, the ratio of monoclinic $ZrO_2$ to cubic $ZrO_2$ is ~ 1:2.5 in the 923 K annealed sample whereas; it is fully monoclinic in DSC_2 sample. It signifies that a considerable fraction of m-$ZrO_2$ is transformed to its cubic phase, which usually is supposed to transform via tetragonal phase and that too at much higher temperatures. It has been argued earlier that such a metastable transformation is made possible by the presence of FeO ($Fe_{0.87}O$ here) [10]. The lattice parameter for the phase is estimated as 5.0807(4) Å, which is in close agreement with the reported value of 5.067(2) Å for the cubic $Zr_{0.9}Fe_{0.1}O_{1.95}$ (ICDD:04-008-4173). However, as mentioned earlier, the phase is unstable at high temperature and hence is not observed in the DSC_2 sample.

### 4.4 Modeling phase formation Kinetics of FeO

During the structural analysis of the Fe - 15 Wt. % $ZrO_2$ system, it is clear that the formation of a stable $Fe_{0.87}O$ phase by the reduction of $Fe_3O_4$, is a very crucial step apart from the $ZrO_2$ dispersoid. Hence a detailed kinetics analysis of this phase has been carried out.

The kinetics of chemical reaction can be analyzed by non-isothermal Kissinger model in order to evaluate the activation energy associated with that reaction. In the present study, the formation kinetics of $Fe_{0.87}O$ has been analyzed by employing Kissinger model for determining kinetic parameters such as the activation energy $E$ and Arrhenius pre-exponential factor $A$. The non-isothermal Kissinger model can be represented as,

$$\ln [\beta/T_p^2] = \ln(AR/E_a) - E_a/(RT_p) \tag{4.2}$$

Where $\beta$ is the heating rate, $A$ is the pre exponential factor and $T_p$ is the peak temperature. The DSC experiments have been carried out at different heating rates of 3, 10, 30, 50, 70 and 90 K min$^{-1}$. The heat flow versus temperature profile has been plotted for different heating rates in Fig. 4.8(a). A shift in the peak temperature is observed with increasing heating rate between 3 and 50 K, beyond which no shifting of formation peak is observed.

Further, ln $[\beta/T_p^2]$ has been plotted with $1/T_p$ in Fig. 4.8(b) which has been numerically fitted with a straight line. The activation energy calculated from the slope yielded a value of 195.8 kJ mol$^{-1}$. This corresponds to the activation energy of formation of $Fe_{0.87}O$ from $Fe_3O_4$.

Further, non-isothermal KJMA model [18] was adopted to study the fraction transformed as a function of heating rate. Fraction transformed has been evaluated from the ratio of partial peak area to that of total area from $T_s$(starting temperature) to $T_f$ which can be represented as

$$f= \left(\int_{T_s}^{T} \Phi(T)dT\right) / \left(\int_{T_s}^{T_f} \Phi(T)dT\right) \tag{4.3}$$

Where $\Phi(T)$ is the base line calibrated DSC output. Figure 4.9 show the fractional formation of $Fe_{0.87}O$ from $Fe_3O_4$ which depicts a sigmoidal behavior. The curve shows a shift towards higher temperatures with increase in heating rate from 3 to 50 K and shows no change beyond. It can be seen from figure 4.9 that the steepness of the fraction transformation curve appears similar for lower heating rate however the steepness has decreased with increasing heating rate beyond 50K.

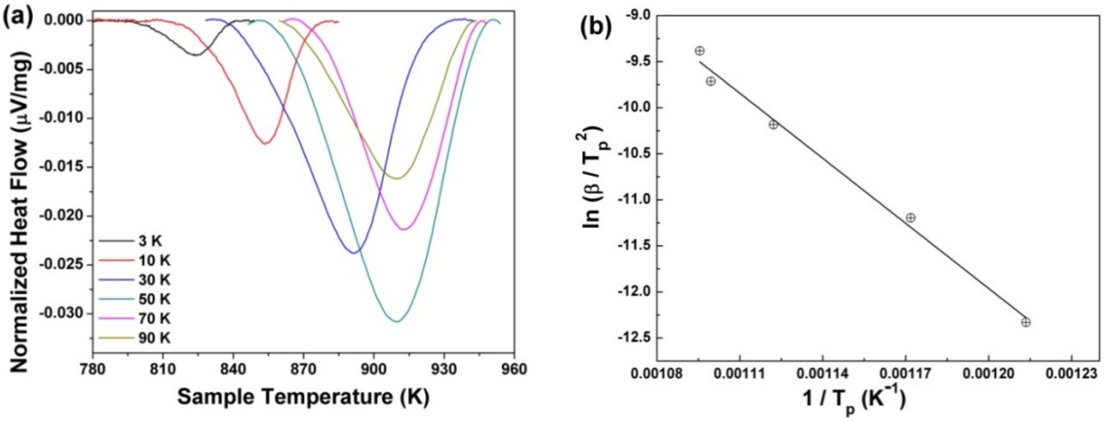

**Figure 4.8:(a) Variation of peak temperature with different heating rate (b) Kissinger's plot fitted with a straight line**

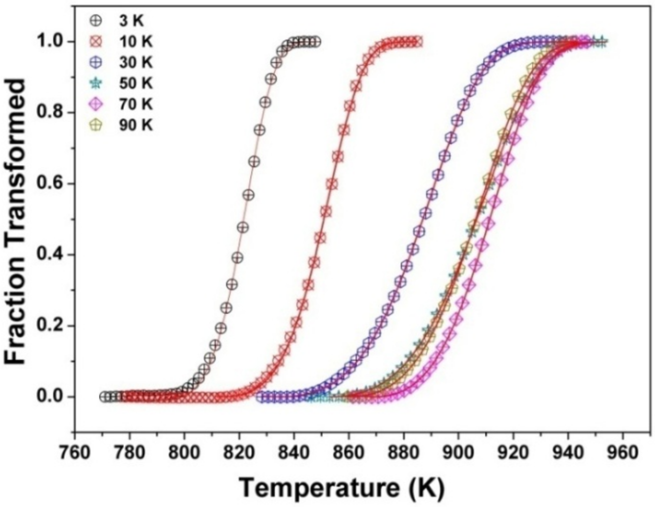

**Figure 4.9: Fractional phase formation as a function of temperature at different heating rates**

## 4.5 $ZrO_2$ crystallite size evolution with time and temperature

Having established the evolution of $ZrO_2$ with temperature, it would be intriguing to investigate its size evolution. Accordingly, the high - temperature stability of dispersoids are investigated and reported here. The following sections deal with determination of the $ZrO_2$ crystallite size as a function of time at $T_A$ of 973 K, 1073 K and 1173 K.

### 4.5.1 Determination of crystallite size by XRD

The XRD analyses of all the powder samples annealed at 973 K, 1073 K and 1173 K has been carried out to understand the microstructural evolution with isothermal annealing. The XRD spectrums recorded for all the samples are shown in Fig. 4.10, for (a) 973 K, (b) 1073 K and (c) 1173 K temperatures. The XRD spectrum for as milled powder is also included in Fig. 4.10(a) for reference. The patterns are indexed for their respective phases and marked. In all the spectra, bcc – Fe (marked 1, 2, 3) and monoclinic $ZrO_2$ (m-$ZrO_2$) (marked α, β) phases are identified. Additionally, the FeO phase has also been detected in the annealed samples and marked as Ø and Δ in the diffraction spectra. The list of phases and their corresponding (hkl) values are listed in Table 4.3.

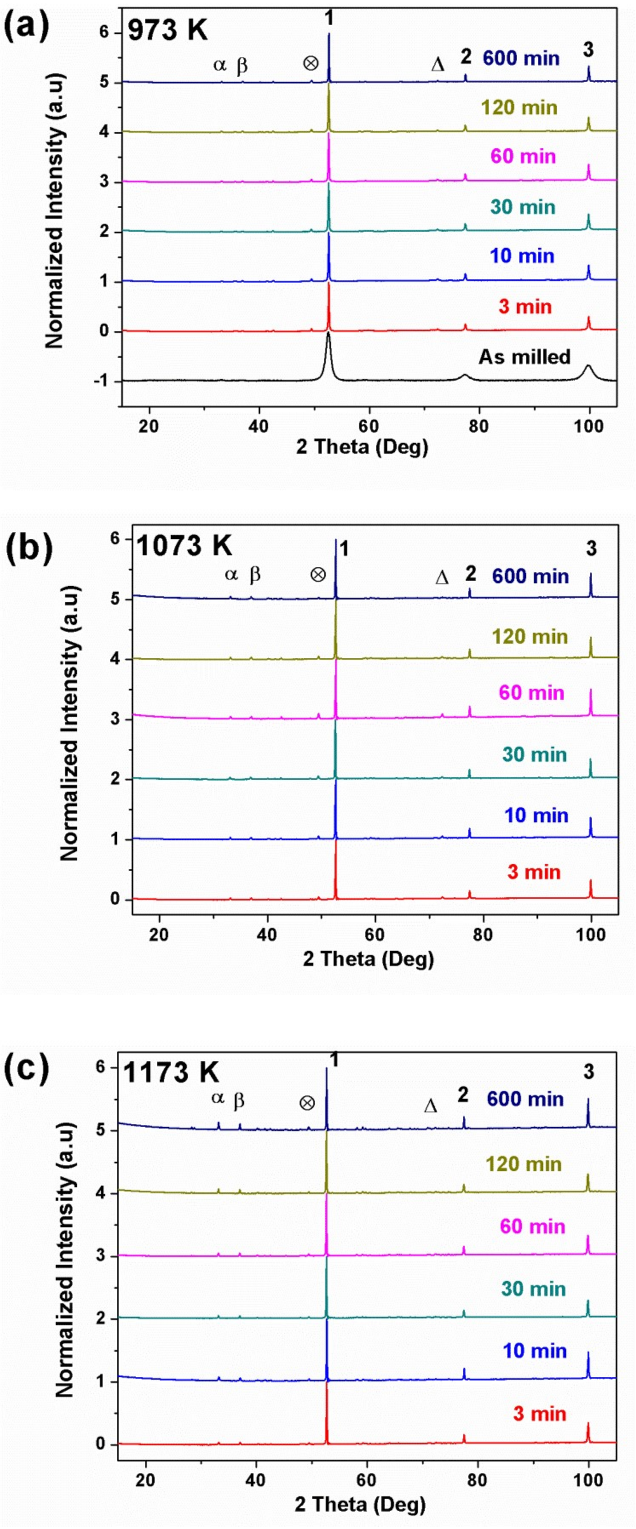

**Figure 4.10: XRD spectrum of the samples annealed for different durations at (a) 973 K (b) 1073 K and(c) 1173 K**

**Table 4.3: Summary of peaks identified from Figure 4.10**

| **Fe(ICDD: 00-006-0696)** | **1**:(110) | **2**:(200) | **3**:(211) |
|---|---|---|---|
| **m- ZrO$_2$(ICDD:00-036-0420)** | **α**:(011) | **β**:($\bar{1}$11) | |
| **FeO(ICDD:01-089-0687)** | **Ø**:(111) | **Δ**:(200) | |

Further, to calculate the crystallite sizes, broadening of diffraction peaks were considered and analyzed through W-H method. A Gaussian peak profile has been assumed for the diffraction peak profile analysis [19]. The W-H method relies on the principle that the total broadening of the diffraction peak β is due to sum of size contribution $\beta_{size}$ and strain contribution $\beta_{strain}$, and these contributions vary with respect to Bragg angle, θ as follows,

$$\beta = \beta_{size} + \beta_{strain} = \frac{0.9\lambda}{D\cos\theta} + \eta\tan\theta \tag{4.4}$$

Where $D$ is the crystallite size, $\lambda$ is the wavelength of the X-ray; $\theta$ is the diffraction angle and $\eta$ corresponds to strain. The term $\beta$ is the FWHM (Full Width at Half Maximum) of the diffraction peak for each of the sample after subtracting the instrumental broadening [20]. Now rearranging the parameters will result in the following equation,

$$\frac{\beta\cos\theta}{\lambda} = \frac{\eta}{2}\left(\frac{2\sin\theta}{\lambda}\right) + \frac{0.9}{D} \tag{4.5}$$

From the above equation, it can be seen that, the plot of $\frac{2\sin\theta}{\lambda}$ Vs $\frac{\beta\cos\theta}{\lambda}$ is a straight line whose intercept and slope can be used to calculate the size and strain, respectively. However, we have concentrated here on the size factor alone. Accordingly, figure 4.11 (a), (b) and (c) shows the graph of K (= $\frac{2\sin\theta}{\lambda}$ ) vs ΔK (= $\frac{\beta\cos\theta}{\lambda}$ ) for 973 K, 1073 K and 1173 K, respectively and their linear fits. The W-H plot for as milled sample (un-annealed sample) is also included in 4.11 (a) for reference.

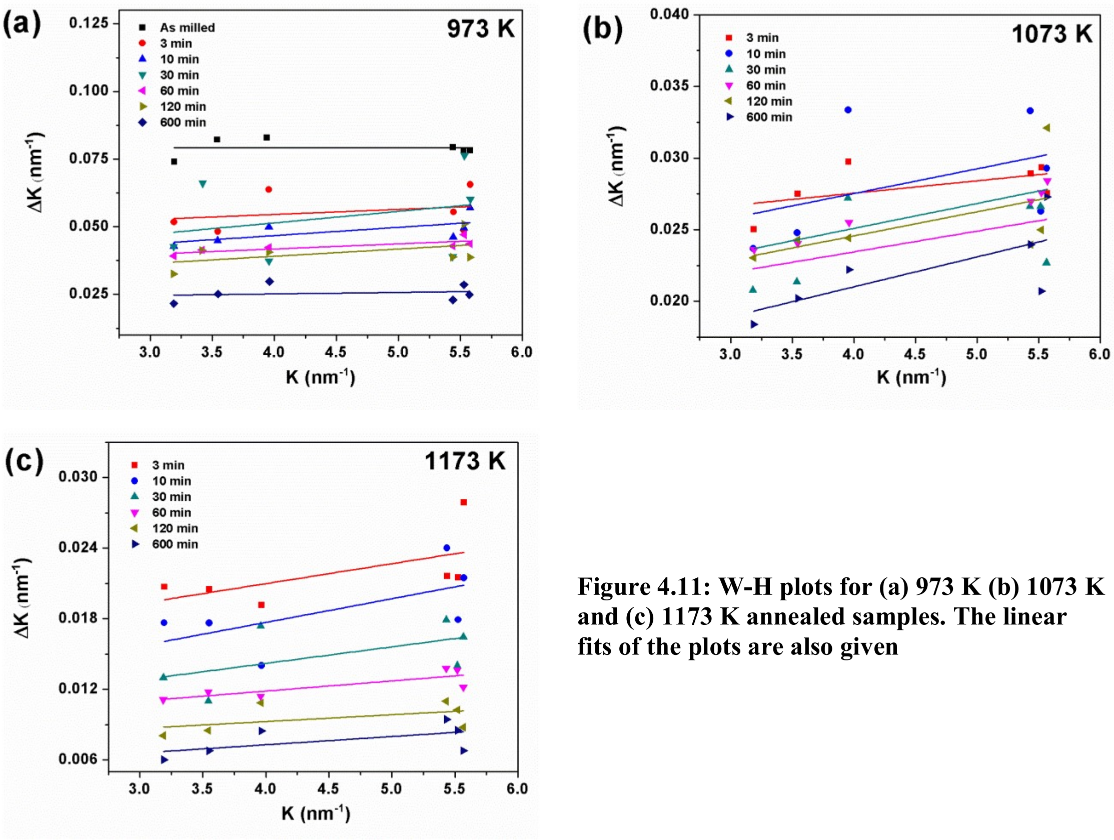

**Figure 4.11: W-H plots for (a) 973 K (b) 1073 K and (c) 1173 K annealed samples. The linear fits of the plots are also given**

The calculated crystallite sizes from the above analyses are listed in Table 4.4. It can be inferred from the table that, the measured sizes for the hold durations at 973 and 1073 K are in the nanocrystalline regime, with a maximum size of 39 nm and 71 nm respectively after 600 min holding. Whereas at 1173 K, the sizes measured 130 nm and 200 nm after 120 and 600 min hold respectively. It needs to be mentioned here that XRD technique measures the dimensions of coherent crystalline domains [19], whereas, larger crystals tend to have sub-grain boundaries and defect boundaries, often leading to an underestimation of sizes by XRD. Moreover, with larger crystallites, the broadening contribution due to size becomes negligible leading to error in estimation of sizes. Due to this inherent limitation on upper limit of grain size that can be determined through X-ray peak broadening analysis, TEM analysis has been carried out and discussed in the following section.

**Table 4.4: Dependence of crystallite size on annealing temperature ($T_A$) and time as determined by XRD analysis**

| Time, t (min) | Crystallite Size, r (nm) | | |
|---|---|---|---|
| | $T_A$= 973 K | $T_A$= 1073 K | $T_A$= 1173 K |
| 0 | 11.4 | 11.4 | 11.4 |
| 3 | 19 | 37 | 63 |
| 10 | 26 | 44 | 94 |
| 30 | 26 | 51 | 105 |
| 60 | 26 | 50 | 107 |
| 120 | 35 | 51 | 130 |
| 600 | 39 | 71 | 200 |

### 4.5.2 Determination of crystallite size by TEM

Microstructural analysis through TEM has been carried out on the samples annealed for holding durations of 120 min and 600 min at all $T_A$, i.e., at 973 K, 1073 K and 1173 K, wherein larger crystallite dimensions are expected, in line with XRD analyses. Figure 4.12 shows the results of microstructural analysis of the samples annealed for 120 min. The BF and corresponding $ZrO_2$ DF micrographs are shown for 973 K (Figure 4.12 (a) and (b)), 1073 K (Figure 4.12 (c) and (d)) and 1173 K (Figure 4.12(e) and (f)) samples, respectively. The SAED patterns for each of these samples are shown as an inset in each BF. As can be observed, the diffraction contrast in the BF micrograph reveals a nanocrystalline structure for 973 K sample which is also reflected by the SAED with a ring pattern characteristic of polycrystallinity. The SAED aperture being only 5 μm in diameter confirms that the crystals contributing to the ring pattern are nanocrystalline. The rings are identified as those from bcc-Fe, while, few spots

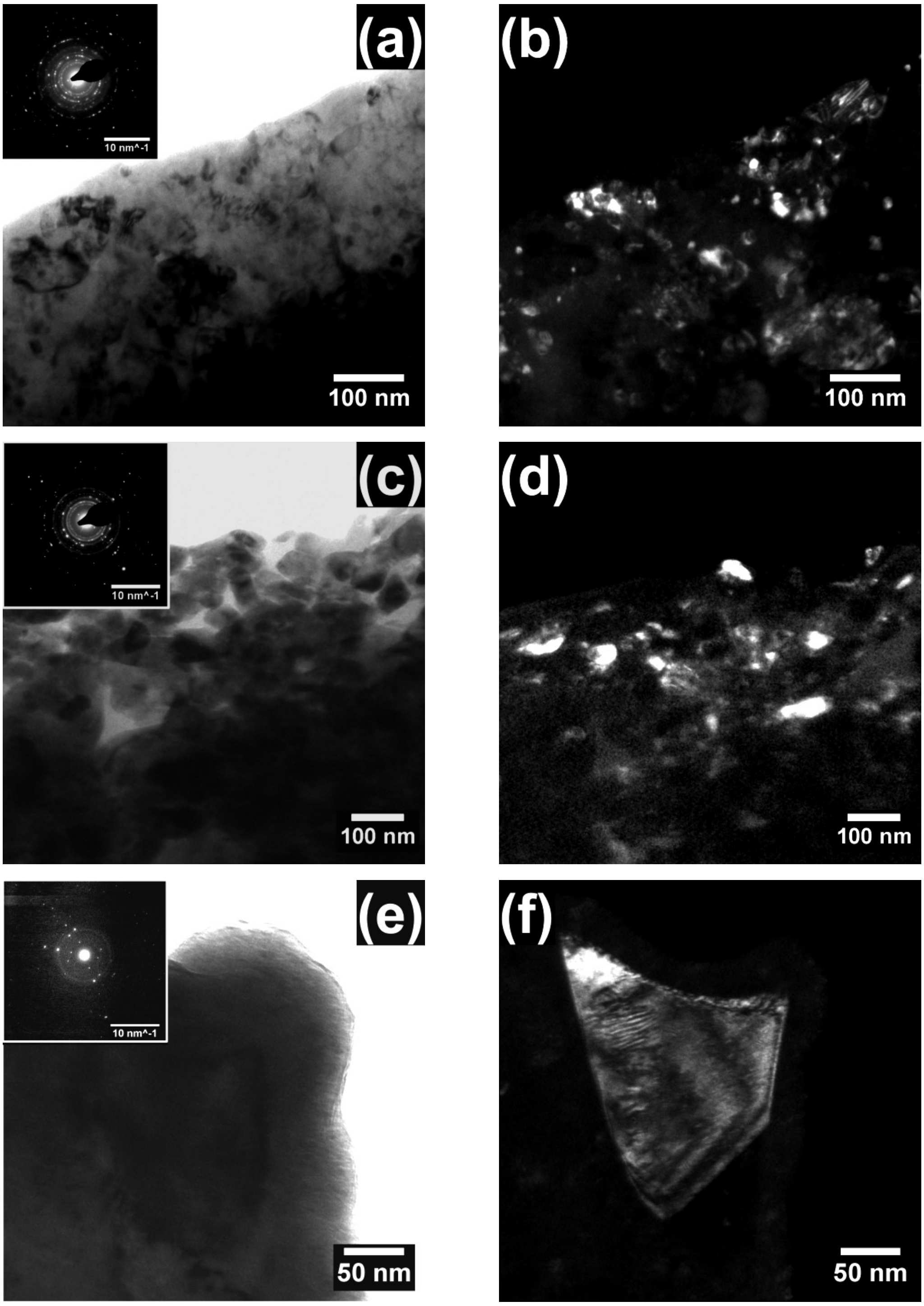

**Figure 4.12: TEM BF (a, c, e) and $ZrO_2$ DF (b, d, f) micrographs for the sample annealed at 973, 1073, 1173 K for a holding time of 120 min, respectively**

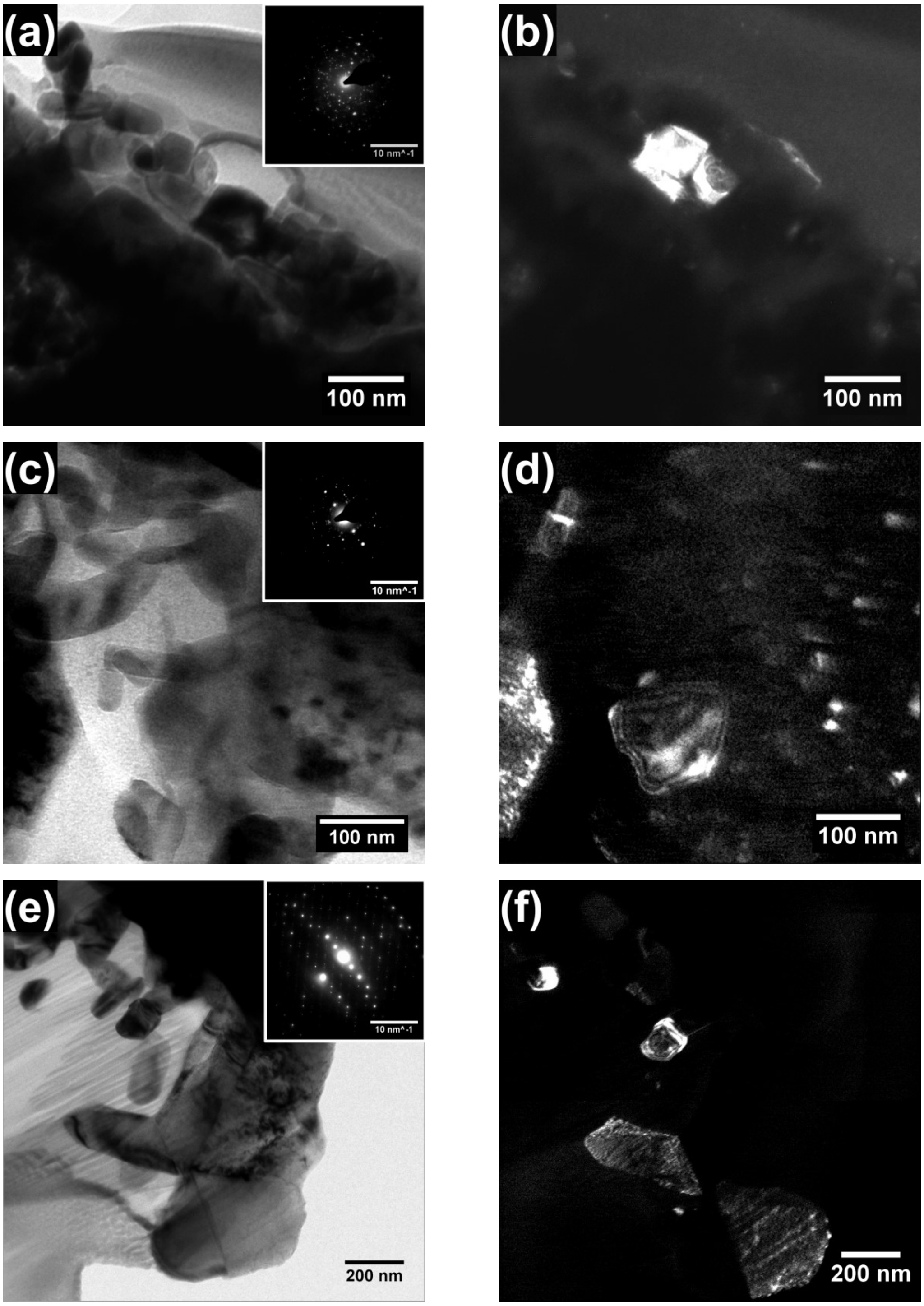

**Figure 4.13: TEM BF (a, c, e) and $ZrO_2$ DF (b, d, f) micrographs for the sample annealed at 973, 1073, 1173 K for a holding time of 600 min, respectively**

corresponding to m-$ZrO_2$ indexed as (111) are also observed. The spots for the later phase indicate less number of crystallites encountered in the SAED. In order to get a clearer picture, DF micrographs from (111) m-$ZrO_2$ are shown in figure 4.12 (b). Fine $ZrO_2$ crystallites measuring 5 - 40 nm are evident. Further, with the increase in temperature, the BF micrograph reveals a tendency for crystallite growth, which is also been observed through sharpened spots for $ZrO_2$ reflection in the SAED. The DF micrographs also reveal a slight increase in the crystallite size for 1073 K sample with a $ZrO_2$ size of ~ 10 – 90 nm. A large crystallite of $ZrO_2$ from 1173 K annealed sample can be seen from figure 4.12 (f).

Further, figure 4.13 shows the TEM BF and DF micrographs for the samples annealed for 600 min at 973 K (Figure 4.13(a) and (b)), 1073 K (Figure 4.13(c) and (d)) and 1173 K (Figure 4.13(e) and (f)). The SAED's are superimposed as insets in the respective BF micrographs. It is observed that the $ZrO_2$ retains its nanocrystallinity even up to 600 min of annealing time at 973 K and 1073 K. The crystallites measuring 20 – 100 nm are measured at 973 K and 50 – 300 nm at 1073 K. However, significant grain growth (50 – 300 nm) is observed after 600 min, when the annealing temperature is raised to 1173 K. The sizes measured from the TEM DF analysis compare well with the XRD measured values at all temperatures and hold times.

From the above results, the time evolution of crystallite size of $ZrO_2$ is plotted as a function of temperature and shown in figure 4.14. The graph representatively demonstrates that, crystallite size increases with an increase in the time as well as temperature of annealing. The crystallite size increases from an initial value of ~ 11.4 nm to ~ 39 nm, 71 nm and 200 nm after 600 min holding time at 973 K, 1073 K and

1173 K, respectively. It can be inferred from the figure that the $ZrO_2$ dispersoids are quite stable against coarsening up to 1073 K. However, growth of dispersoids is quite evident at 1173 K for holding durations of 120 min and beyond.

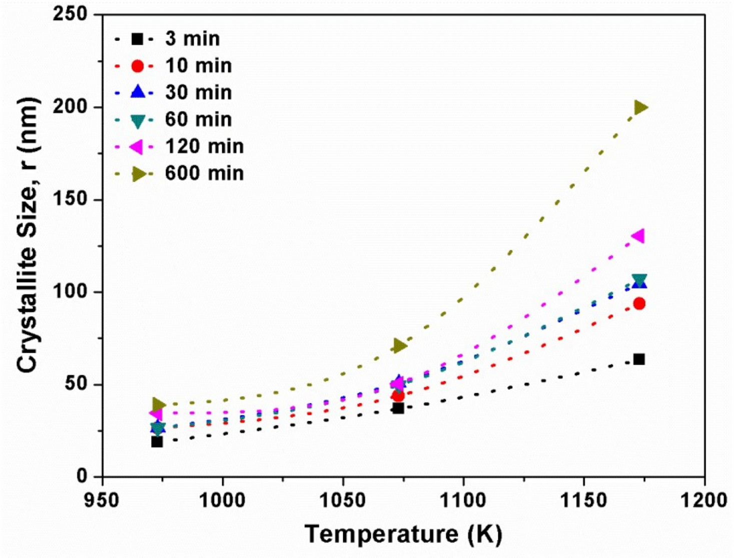

**Figure 4.14: Time evolution of $ZrO_2$crystallite sizes with Temperature**

### 4.6 Kinetics of grain growth - Ostwald ripening model

As the m-$ZrO_2$ crystallites grow with time at various temperatures, sometimes sluggishly and sometimes fast, it is important to quantitatively estimate the kinetics of growth. The coarsening of oxide particles at high temperatures takes place via Ostwald ripening, where, the driving force for coarsening comes from the decrease in total surface free energy and the process occurs by the growth of large particles at the expense of smaller ones which dissolve [21]. It is predicted that, at any stage during coarsening there is a critical particle radius $r^*$ in equilibrium with the mean matrix composition; particles with $r > r^*$ will grow and particles with $r < r^*$ will shrink. The decrease in the total grain boundary energy is the main driving force for the grain growth, and the rate of grain growth is proportional to the curvature of the grain surface

[22]. The kinetic relationship for such coarsening may be sought through the Ostwald ripening mechanism. The governing equation is a generalized parabolic growth law [23] and can be written as [24, 25],

$$r^n - r_o^n = kt \qquad (4.6)$$

The parameters, $r$ and $r_o$ are the crystallite sizes at time $t$ and before annealing, respectively. $k$is a kinetic parameter and $n$ is the grain growth exponent, which are discussed below.

The kinetic parameter, $k$follows an Arrhenius behavior and is a temperature and diffusion process dependent constant parameter described by Eq. (4.7) below:

$$K = k_o exp\ (-Q/RT) \qquad (4.7)$$

Where, $k_o$ is a kinetic constant, $Q$ is the activation energy, $R$ is the universal gas constant, $T$ is the temperature in K, $t$ is the annealing time.

The value of $n$ depends on the microstructure of the material and also on the mechanism of grain growth [26]. The value of $n$=3, corresponds to lattice diffusion, $n$=4 for grain boundary diffusion while $n$=5 for dislocation pipe diffusion [24]. '$n$' value could be even higher for nc materials; viz., a '$n$' value as high as 16 has been reported for nc Fe [22]. Some high purity, fully dense polycrystallinemetals show grain growth exponents ranging even from '$n$' = 20 to '$n$' = 2, with a systematic decrease in exponentas the testing temperature is increased [27].

Owing to the large surface area fraction in the nc materials, it can be presumed that, the diffusion mechanism in these systems differ much from their bulk counterpart. Considering that the material is processed through ball milling, which involves sever plastic deformation induced grain fragmentation, it can be assumed that pipe diffusion mechanism is dominant [24, 25], in which case, $n$=5. Pipe diffusion is dislocation driven, wherein, both interstitial and substitutional diffusion can occur via dislocations, owing to the large space available at these defect sites. This is consistent with the current analysis; as, a fairly high dislocation density (~ 2.3 x $10^{16}$ / $m^2$) has been reported for the initial (un-annealed) powder earlier [Chapter III]. Further, the activation energy barrier is also known to be lower for this kind of diffusion mechanism.

Based on above discussion, substituting n=5 in Eq. (4.6),

$$r^5 - r_o^5 = kt \tag{4.8}$$

Linear plot of $t$ versus $r^5 - r_o^5$,for 973 K, 1073 K and 1173 K are shown in figure4.15 (a), slope of which have been used for estimation of $k$. These values of $k$ have been used to plot $ln\ k$vs$1/T$ using the relationship given in Eq. (4) and shown in figure 4.15(b). Linear fits of this graph have been utilized for calculation of $Q$ ($379\ kJ\ mol^{-1}$) and $k_o$($3.85*10^{-22} m/s$) from the slope and intercept, respectively.

Substituting $k$ from Eq. (4.7) in Eq. (4.8) and rearranging the terms yields,

$$r = [r_o^5 + k_o exp\ (-Q/RT)*t]^{1/5} \tag{4.9}$$

Eqn. (4.9) is a kinetic equation, which, with the inputs of $r_o$, $k_o$ and $Q$, can be utilized to understand the size evolution at a particular temperature. $r_o$ can be obtained from Table 4.4, at $t$ = 0 and $k_o$ and $Q$ are also known. Accordingly, $r$ versus $t$ is plotted in figure 4.15(c). The experimentally measured crystallite sizes (Table 4.4) are also overlaid on this plot. A good correlation between predicted and experimentally measured grain size is observed.

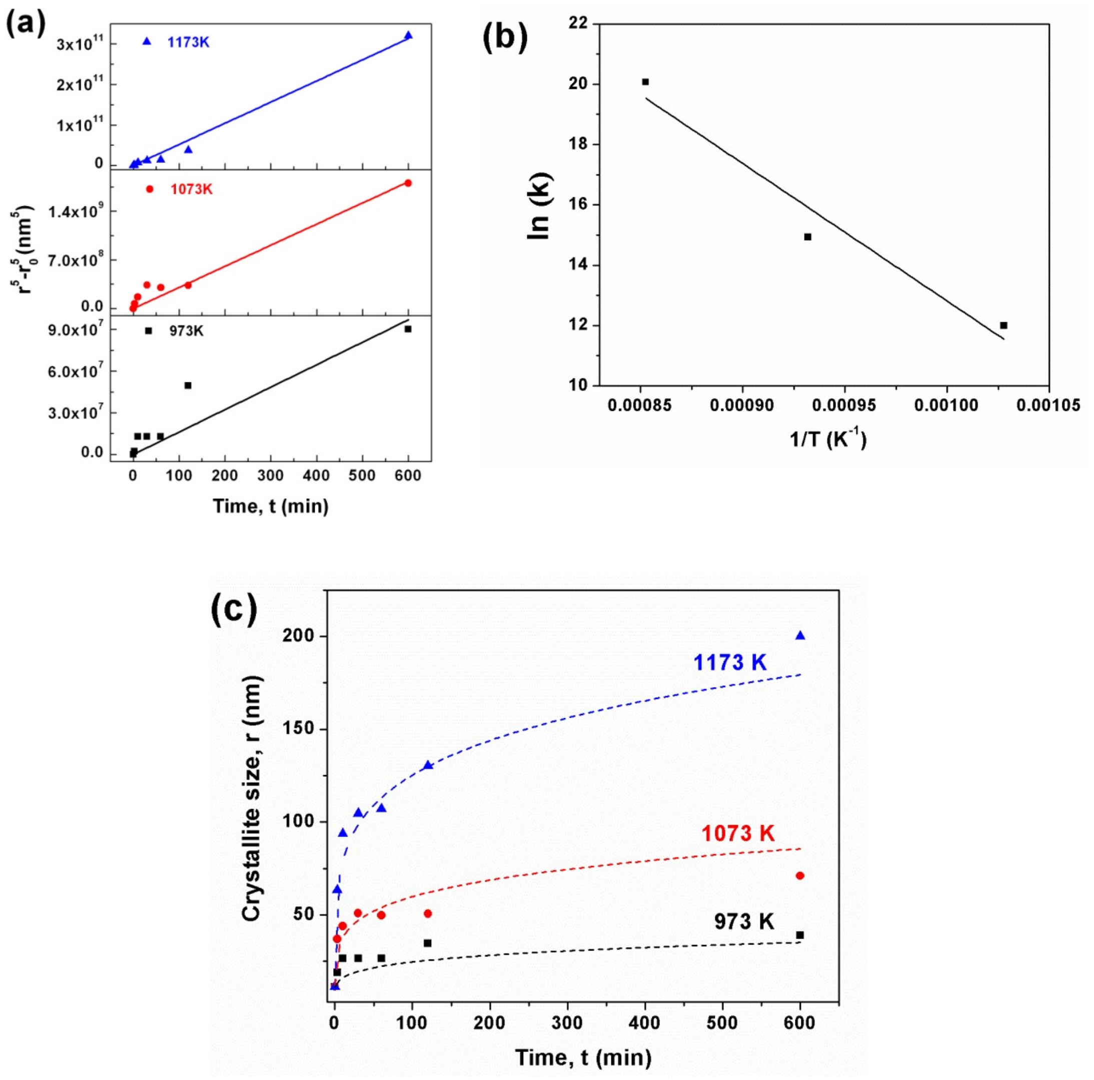

**Figure 4.15: (a) Graph of $r^5 - r_o^5$ vs *t* (b) *ln k vs 1/T* and (c) Crystallite size evolution with time fitted with Eqn. (4.9)**

The calculated activation energy of 379 kJ mol$^{-1}$ in this study, is lower than the reported value for the bulk $ZrO_2$, which is ~580 kJ mol$^{-1}$ [28] and it is attributed to the nc nature of the material. It is reported in the literature that, relatively low activation energy is typical of nc materials [26, 29, 30] owing to large surface area and higher diffusion coefficients of the migrating species. Additionally, the large fraction of nc Fe also tends to grow at these higher temperatures and possibly plays a role in the lower activation energy for $ZrO_2$ growth in this study. The relatively faster diffusing Fe crystallites and their migrating grain boundaries can also drag the $ZrO_2$ crystallites along with them, resulting in faster grain growth of nc $ZrO_2$. In comparison , the activation energies of nc $Y_2O_3$ and bulk polycrystalline $Y_2O_3$ are ~ 150 kJ $mol^{-1}$ and 290 kJ $mol^{-1}$, respectively [31]. Comparing the activation energies of nc m-$ZrO_2$ and nc$Y_2O_3$, it is clear that $ZrO_2$ is more resistant to coarsening than $Y_2O_3$. Thus the $ZrO_2$ is expected to be an excellent choice as an alternate dispersoid material for ODS steel.

### 4.7 Conclusions

A detailed analysis on thermal evolution of Fe -15 Wt.% $ZrO_2$ powders by DSC experiments revealed a number of endothermic and exothermic peaks corresponding to evolution of phases. Assignments of phases were arrived after detailed structural analysis using SEM, TEM and Synchrotron XRD of simulated samples. Important conclusions are drawn from the chapter are listed below.

- A FeO phase was found to form at about 854 K, which was analyzed to be a metal deficient oxide, namely $Fe_{0.87}O$, bearing a lattice parameter of 4.2946(2) Å. Kinetics of formation of the $Fe_{0.87}O$ phase was also estimated by KJMA analysis and the activation energy of ~195 kJ $mol^{-1}$ was calculated.
- A metastable cubic $ZrO_2$ ($Zr_{0.9}Fe_{0.1}O_{1.95}$) was observed to be stabilized by the $Fe_{0.87}O$ at around 923 K. The phase however, was found to be unstable at elevated temperatures.
- A broad Fe $\alpha \rightarrow \gamma$ endothermic transformation peak was observed during first DSC run. The phenomenon was attributed to nanocrystallinity of the Fe grains, by means of microscopy evidences.

- Concerning the stability, the $ZrO_2$ dispersoids found to retain their fine sizes at 973 K and 1073 K up to 600 min of hold time, with sizes measuring 39 nm and 71 nm, respectively. At 1173 K, crystallites found to grow even beyond 600 min hold time with measured sized of ~ 200 nm after 60 min.
- Ostwald ripening model is adopted for understanding the coarsening of $ZrO_2$. Dislocation driven pipe diffusion is assumed and growth kinetics are evaluated. An activation energy of ~ 379 kJ $mol^{-1}$ is observed for the growth of $ZrO_2$ crystallites, superior to nc $Y_2O_3$.
- Excellent grain growth resistance and stability by $ZrO_2$ even in a concentrated alloy is thought to be beneficial for the dispersoid coarsening resistance, thus validating the superiority of $ZrO_2$ as a candidate dispersoid for ODS application.

## 4.8 References

1. Mao, X., *et al.*, *Materials Characterization* (2016) 117, 91

2. Cochrane, R. W., *Rapidly Quenched Metals 6*. Elsevier Science: 1988

3. Landolt-B¨ornstein, Tables of Magnetic Properties of 3d Elements, New Series. Springer, (ed.), Berlin, (1986), Vol. 3

4. Hiroshima, T., *et al.*, *Journal of the American Ceramic Society* (1996) 79 (12), 3235

5. Hwang, H. J., *et al.*, *Journal of the American Ceramic Society* (1998) 81 (3), 709

6. Bonetti, E., *et al.*, *Journal of Applied Physics* (2001) 89 (3), 1806

7. Cornell, R. M., and Schwertmann, U., *The Iron Oxides*. Wiley: 1996

8. Worral, E., and Coley, K. S., *Canadian Metallurgical Quarterly* (2013) 52 (1), 23

9. Korznikov, A. V., *et al.*, *Acta Metallurgica et Materialia* (1991) 39 (12), 3193

10. Bechta, S. V., *et al.*, *Journal of Nuclear Materials* (2006) 348 (1–2), 114

11. Jiang, J., *et al.*, *Journal of Materials Research* (1999) 14 (4), 1343

12. Bannister, M. J., and Barnes, J. M., *Journal of the American Ceramic Society* (1986) 69 (11), C

13. Raghavendra, K. G., *et al.*, *Powder Technology* (2016) 287, 190

14. Bhaskar, P., *et al.*, *Materials Science and Engineering: A* (2014) 616 (0), 71

15. Rong, Y., *Current Opinion in Solid State and Materials Science* (2005) 9 (6), 287

16. Wen, C., *et al.*, *Materials Science and Engineering: A* (2006) 438–440, 420

17. Vijay, R., *et al.*, *Metall and Mat Trans A* (2013) 44 (3), 1611
18. Fanfoni, M., and Tomellini, M., *Il Nuovo Cimento D* (1998) 20 (7), 1171
19. Suryanarayana, C., and Norton, M. G., *X-Ray Diffraction - A Practical Approach*. Springer US 1998
20. Chen, S.-G., *et al.*, *Journal of Crystal Growth* (2004) 267 (1), 100
21. Baldan, A., *Journal of Materials Science* (2002) 37 (11), 2171
22. Mayo, M. J., *International materials reviews* (1996) 41 (3), 85
23. Rane, G. K., *et al.*, *Acta Materialia* (2012) 60 (20), 7011
24. Oono, N. H., *et al.*, *Journal of Nuclear Materials* (2017) 493, 180
25. Oono, N., *et al.*, *Nuclear Materials and Energy* (2016) 9, 342
26. Chen, Z. W., *et al.*, *Appl. Phys. A* (2005) 80 (4), 703
27. Koch, C. C., *et al.*, *Structural Nanocrystalline Materials: Fundamentals and Applications*. Cambridge University Press: 2007
28. Nieh, T. G., and Wadsworth, J., *Acta Metallurgica et Materialia* (1990) 38 (6), 1121
29. Lai, J. K. L., *et al.*, *Scripta Materialia* (2003) 49 (5), 441
30. Hynes, A. P., *et al.*, *Journal of the American Ceramic Society* (2002) 85 (8), 1979
31. Chaim, R., *et al.*, *Journal of the European Ceramic Society* (2009) 29 (1), 91

Chapter V

# Synthesis and characterization of $ZrO_2$ dispersed 9Cr steel powder

## 5.1 Introduction

The chapters III and IV have established $ZrO_2$ as an alternate dispersoid with rigorous analysis on its evolution during milling and annealing through studies on a Fe-15 Wt. % $ZrO_2$ model alloy. The comprehensive knowledge accumulated through the studies on this model system has been now utilized for the synthesis of a $ZrO_2$ dispersed 9Cr ODS steel, which will become the contents of this chapter and the next. The 9Cr variant steels have gained prominence due to their anisotropic structure and low DBTT compared to high Cr steels [1-4]. This chapter deals with the synthesis of a ODS steel powder of composition, Fe-9Cr-2W-0.01C-0.35 $ZrO_2$ (all in Wt. %) and its detailed characterization. The synthesis of the ODS steel powder has been carried out at optimized ball milling duration of 100 h under optimum milling parameters, as described in chapter III. The microstructure of the 9Cr $ZrO_2$ODS steel powder in as milled and high temperature annealed condition has been studied in detail. The chapter is organized as follows. Section 5.2 gives a brief introduction on the synthesis of powder followed with section 5.2.1 detailing about the structure and chemistry of starting 9Cr steel powder and $ZrO_2$dispersoid. The section 5.2.2 discusses the structure and chemistry of the milled 9Cr $ZrO_2$ODS steel powders. Structural evolution of the milled 9Cr $ZrO_2$ ODS powder during annealing is discussed in section 5.3 followed with a discussion on microstructural characterization by SEM in 5.3.1. Phase analysis by diffraction techniques is presented in 5.3.2 and phase evolution using Synchrotron XRD in 5.3.2.1. Confirmation of Phases through TEM – SAED technique is discussed in 5.3.2.2. Microstructural investigation by TEM is elaborated in section 5.3.3 followed with summary of the chapter in 5.4.

## 5.2 Synthesis of 9Cr $ZrO_2$ dispersed steel powder

The first step to production of ODS alloys is mechanical milling of pre alloyed steel powder reinforced with ($ZrO_2$) dispersoid. It is important to keep in mind that the knowledge of initial microstructure plays an important role in the ODS steel production. In line with this, section 5.2.1 discusses the initial microstructure of 9Cr steel powder and $ZrO_2$ dispersoid. The chemical composition of the pre alloyed steel powders may be recalled here from Table 2.1.

### 5.2.1 Structure and chemistry of starting 9Cr steel powder and $ZrO_2$ dispersoid

Figure 5.1(a) shows the SE micrograph of the starting 9Cr steel powder. The powder particles were observed to be in the size range of ~ 5 – 90 μm and spherical in shape, typical of the gas atomization process. Powder morphology is important during milling as the geometrical properties of the powder are interlinked with their mechanical properties [5]. The chemical composition of the powder was ascertained through EDS in SEM and shown in figure 5.1(b). Semi quantitative analysis showed the presence of Fe, Cr and W to be ~ 90.1%, 7.9% and 2% (all in Wt. %), respectively, which is in agreement with the initial composition (Table 2.1). Figure 5.1(c) shows the TEM BF micrograph of initial $ZrO_2$ powder particles. Varying particle sizes were observed with a considerable overlapping of the neighbouring particles. The ring SAED pattern shown as an inset in figure 5.1(c) indicates the polycrystalline nature of the sample. Further, to get an estimation of the crystallite size, $(\bar{1}10)$ reflections of the m-$ZrO_2$ phase was utilized to image the DF micrograph and shown in figure 5.1(d). It is observed that the $ZrO_2$ crystallites were measuring 5 – 90 nm in size. A finer initial crystallite size is important, as, it is difficult to reduce the crystallite size of hard ceramic particles if it is too large in the beginning. Further, the mechanical milling is expected to bring down the dispersoid sizes to < 5 nm with a homogeneous distribution which ensures a smaller inter-dispersoid spacing. This is a more effective means of increasing dispersion strengthening than increasing volume fraction of dispersoid[6].

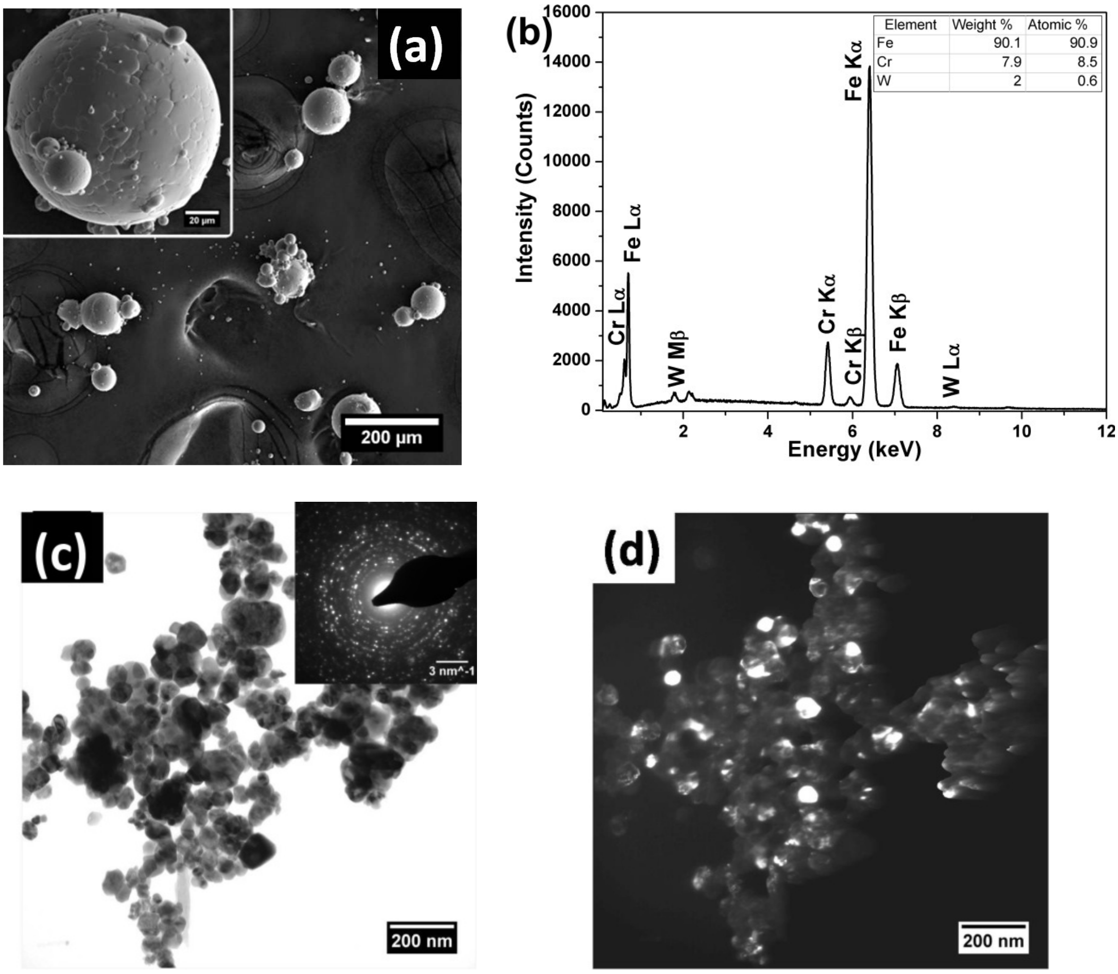

| Element | Weight % | Atomic % |
|---|---|---|
| Fe | 90.1 | 90.9 |
| Cr | 7.9 | 8.5 |
| W | 2 | 0.6 |

**Figure 5.1: (a) SE micrograph of gas atomized Plain 9Cr powder particles, inset showing an individual spherical powder particle. (b) EDS spectrum from the steel powder, depicting the chemistry. TEM (c) BF and (d) DF micrograph showing $ZrO_2$ powder crystallites**

### 5.2.2 Structure and chemistry of the milled 9Cr ODS steel powder

The SE micrograph of the milled 9Cr ODS steel powder is given in figure 5.2(a), which shows an irregular morphology. This is understood in terms of the prolonged milling, during which the powder particles agitate between themselves, with the walls of the container and between the balls [7, 8]. This results in the plastic deformation of the powder particles, thus changing their morphology [9, 10]. The sizes of the powder particles measure ~ 1- 20μm.

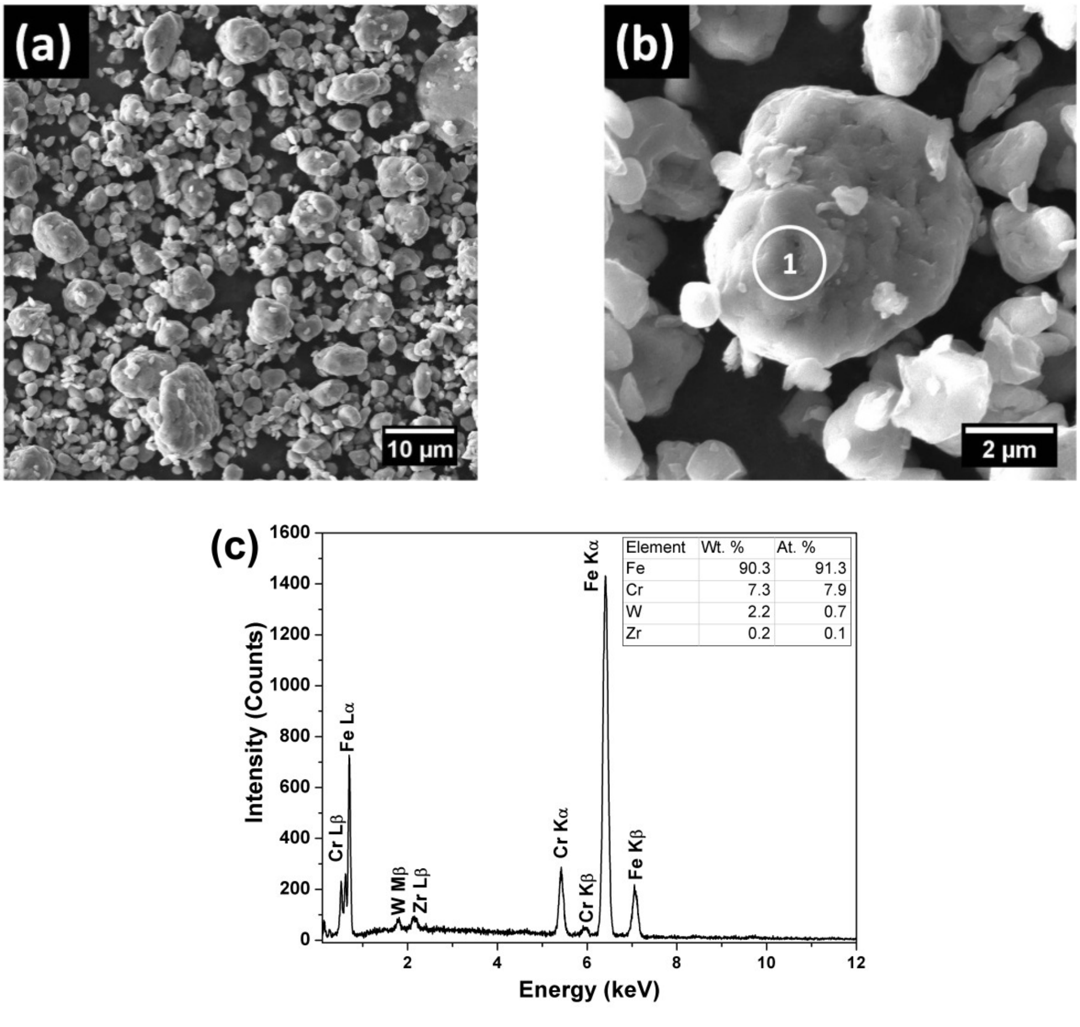

| Element | Wt. % | At. % |
|---|---|---|
| Fe | 90.3 | 91.3 |
| Cr | 7.3 | 7.9 |
| W | 2.2 | 0.7 |
| Zr | 0.2 | 0.1 |

**Figure 5.2: SE micrograph of the milled 9Cr ODS steel powder (a) Low magnification (b) an individual particle at higher magnification (c) EDS spectrum from the milled powder depicting the chemistry**

Further, the microstructure of the powder particle at a higher magnification is shown in figure 5.2(b) and it represents a convoluted lamellar structure typical of the ball milling [10]. As discussed in Introduction, the mechanical milling of ODS alloys fall in the Ductile (matrix) – Brittle (dispersoid) component category and the convoluted lamellar structure ensures the uniform dispersion of oxide particles in the composite steel powder [10]. The EDS result obtained from a typical powder particle (circle marked 1 in figure 5.2(b)) is shown in figure 5.2(c) and it shows a similar chemistry as that of the initial powder. The presence of Zr was also identified and used in the quantitative analysis, whereas O was not included in the quantification, owing to the inherent limitations of EDS in quantifying the low-Z elements.

TEM investigations of the milled 9Cr ODS steel powders have been carried out in order to examine its crystallinity. Figure 5.3(a) shows the BF micrograph obtained from a powder particle. The diffraction contrast in the micrograph reveals the numerous nc grains within the powder particle. This shows the complete nano-crystallization of the ODS steel after 100 h of milling. Further analysis of the nc grains were carried out by SAED pattern analysis on this powder particle shown in figure 5.3(b). The ring patterns seen in this figure are characteristic of the polycrystalline nature of the sample. Accordingly, each ring is indexed and assigned a number, as shown in the figure. It was noted that all the rings marked from 1 to 6, correspond to the bcc Fe phase [ICDD: 00-006-0696]. Further, a faint ring marked $ and a spot (highlighted with a circle) in the micrograph have been found to correspond to ($\bar{1}11$) and (111) reflections of m-$ZrO_2$, respectively. These reflections establish the retention of crystallinity of the $ZrO_2$ dispersoids, as conjectured. Further, in order to ascertain as to which of the nanocrystals belong to Fe and $ZrO_2$, DF TEM analyses have been carried out. Figure 5.3(c) shows DF micrograph corresponding to the (110) reflection of Fe. The image establishes that the Fe grains after 100 h of milling measures 5 – 100 nm in size; distribution is shown as an inset of figure 5.3(c). The nanocrystalline grain structure for Fe is attributed to severe plastic deformation during the milling process. Further, figure 5.3(d) shows the DF micrograph corresponding to the $(\bar{1}11)$ reflection of m-$ZrO_2$. The $ZrO_2$ nano-crystallites were found to be distributed uniformly. The size distribution of the crystallites is given as the inset in figure 5.3(d) and that shows that the majority of $ZrO_2$ crystallites are measuring < 5 nm in size. Finer dispersions are believed to be entrapped between the ductile lamellas of the matrix and uniformly distributed as discussed earlier. The DF results are also is in line with this conjecture. Further, it is important to note here that, both the matrix and dispersoid are nc in nature and together forms a nanocomposite structure.

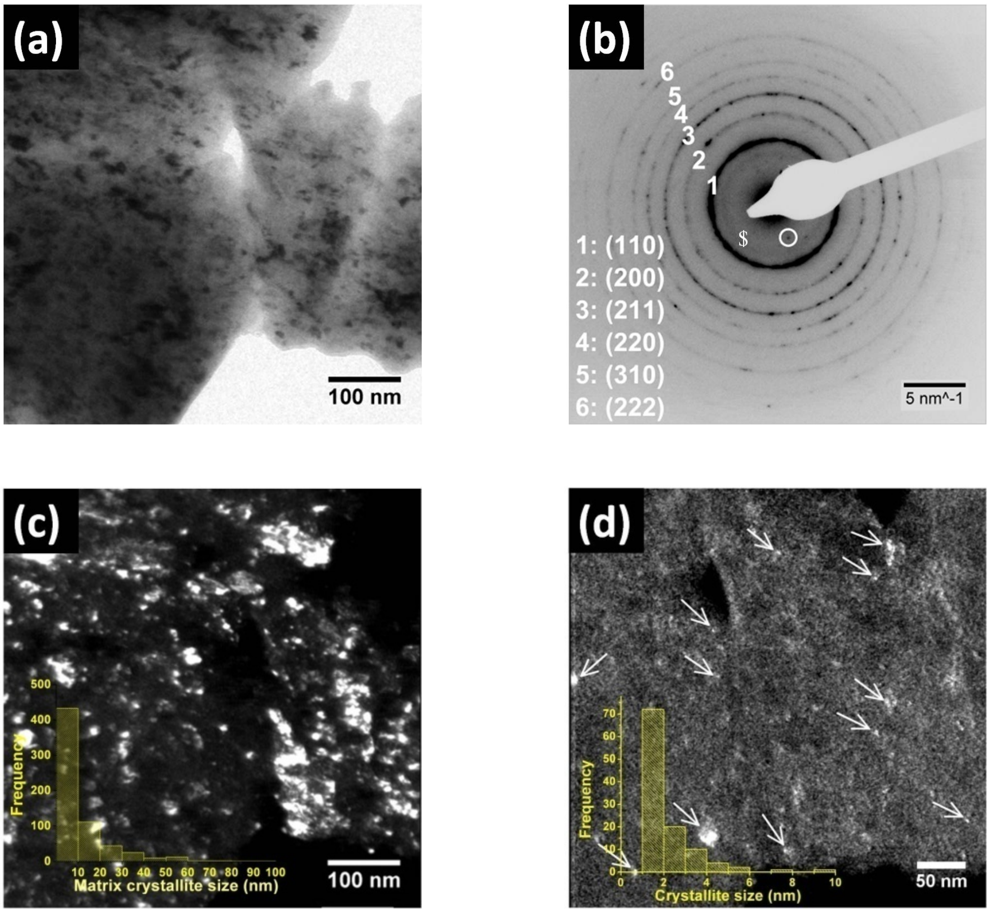

**Figure 5.3: (a) BF micrograph of the milled ODS steel powder (b) SAED pattern showing the ring pattern (c) DF micrograph corresponds to the matrix (Fe) phase (d) $ZrO_2$ DF micrograph showing nanocrystalline dispersoids, inset showing the size distribution of the dispersoids.**

## 5.3 Structural evolution of the milled 9Cr ODS powder during annealing

Annealing characteristics of the milled ODS powder is examined with an objective to understand the microstructural and microchemical evolution at high temperatures, knowledge of which, is important for the optimal choice of temperatures for consolidation and subsequent thermo-mechanical treatments. The samples are annealed at 723 K and 1223 K for 1h. Detailed analyses are discussed in the subsequent sections.

### 5.3.1 Microstructural characterization by SEM

Figure 5.4 (a) and (b) shows the SE micrographs of the powder annealed at 723 K and 1223 K, respectively. It is observed from the figures, that, for samples annealed at both these temperatures changes in the powder particle sizes in comparison to the initial powders (figure 5.2(a)), is insignificant. But the difference becomes apparent when we investigate the material at a higher magnification, as shown in figure 5.4(c) and 5.4(d), for 723 K and 1223 K annealed samples, respectively. A distinct microstructural difference is observed between the two, the latter showing fine grain features. The observation indicates temperature induced grain growth, which is further investigated by diffraction analysis using Synchrotron XRD and TEM.

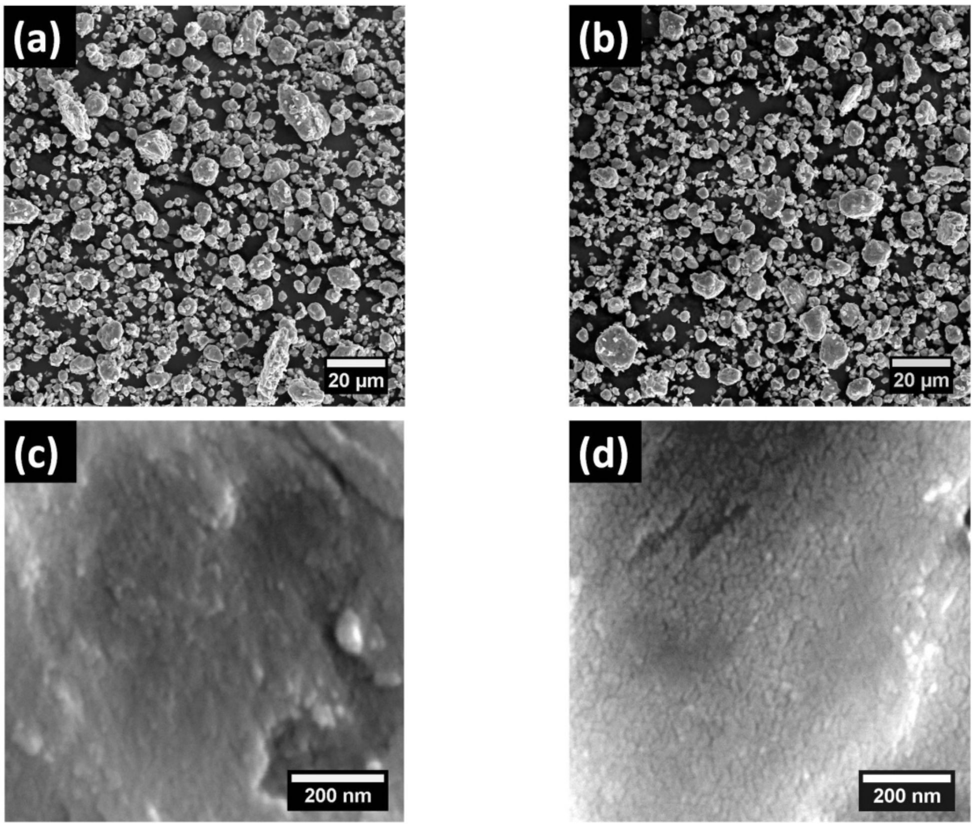

**Figure 5.4: SE micrographs of the milled and annealed ODS steel powder;(a) and (c) shows low and high magnification micrographs of powder annealed at 723 K whereas (b) and (d) shows low and high magnification micrographs of powder annealed at 1223 K.**

## 5.3.2 Phase analysis by Diffraction techniques

### 5.3.2.1 Understanding the phase evolution using Synchrotron XRD

The high temperature evolution of the material may result in precipitation of new phases, grain growth, phase transformations of the existing phases etc. In order to understand this, a high brilliance Synchrotron XRD has been used and the results are discussed as follows.

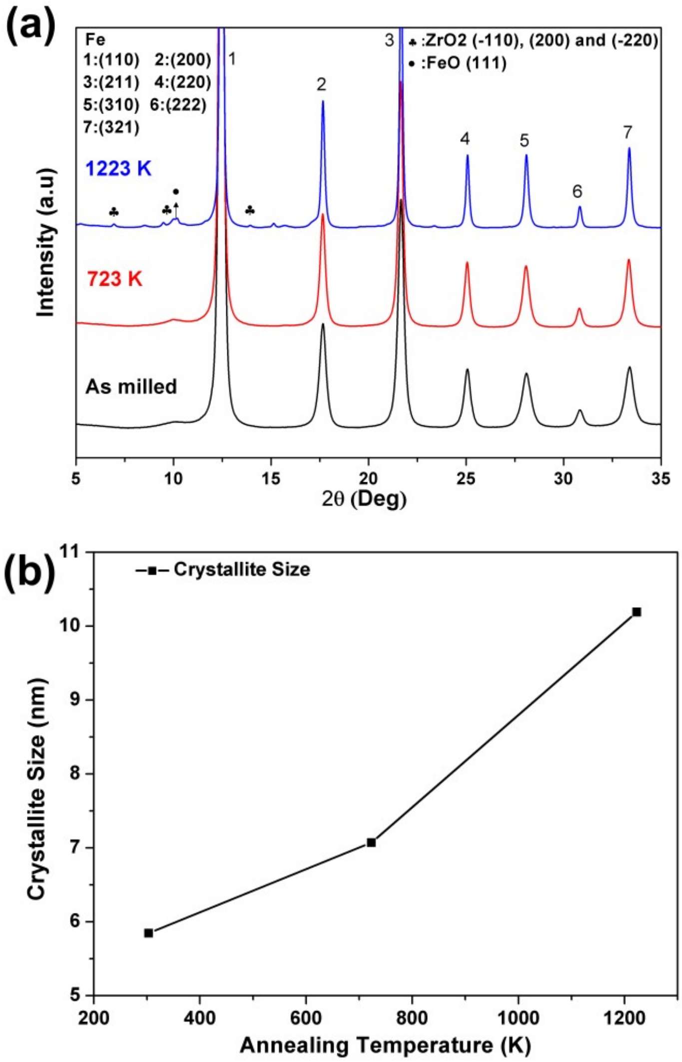

**Figure 5.5: (a) X-Ray Diffraction pattern of as milled and annealed steel powder (b) Variation of crystallite size with annealing temperature as calculated by W-H analysis**

Figure 5.5(a) shows the synchrotron XRD patterns of as milled and annealed samples at temperatures 723 K and 1223 K. It can be noticed that all the peaks show a gradual decrease in FWHM with increase in annealing temperatures. The peaks marked 1 to 7, represents the bcc Fe phase. The minor m-$ZrO_2$ phase is well identified in the sample annealed at 1223 K and marked as '♣'. Additionally, a reflection marked '●' is observed in the sample annealed at 1223 K, which is not present in the other two diffractogram. This peak is identified as a non-stoichiometric FeO ($Fe_{0.92}O$) phase as discussed in Chapter IV. It may be recalled that, the prolonged milling has lead to the accumulation of excess O in the matrix and further, during annealing this O reacts with the elemental Fe to form $Fe_3O_4$, which eventually lead to the formation of FeO at 854 K [11]. The current results are also is in line with this observation. Additionally, the sizes of the Fe crystallites are calculated using diffraction peak analysis by W-H method and graph showing the variation of size with annealing temperature is shown in figure5.5(b). With Increasing annealing temperature Fe crystallites showed an increasing size but remained nc throughout. A maximum of ~ 10 nm is observed after annealing at 1223 K.

#### 5.3.2.2 Confirmation of Phases through TEM – SAED technique

In order to confirm the phases present in the 9Cr ODS steel powder, TEM – SAED analysis was carried out. The SAED patterns from the alloy powder annealed for 723 K and 1223 K using a 10 μm aperture are shown in figure 5.6(a) and 5.6(b), respectively. Similar to the as-milled powder, ring patterns characteristic of polycrystalline bcc Fe is observed in both the samples. In order to identify the minor phases, the radial profiles of the SAED patterns are shown in figure 5.6(c). The figure also incorporates the radial profile from the SAED pattern of as milled powder (Figure

5.3(b)) as reference. Only Fe (1 to 7) and m-$ZrO_2$ (♣, ♠) are identified in the radial profiles of as milled and 723 K annealed samples. It is interesting to note that the 1223 K annealed sample reveals additional peaks marked as $ and *, which correspond to the (111) and (511) reflections of the FeO phase, respectively. This is in line with the synchrotron results described earlier.

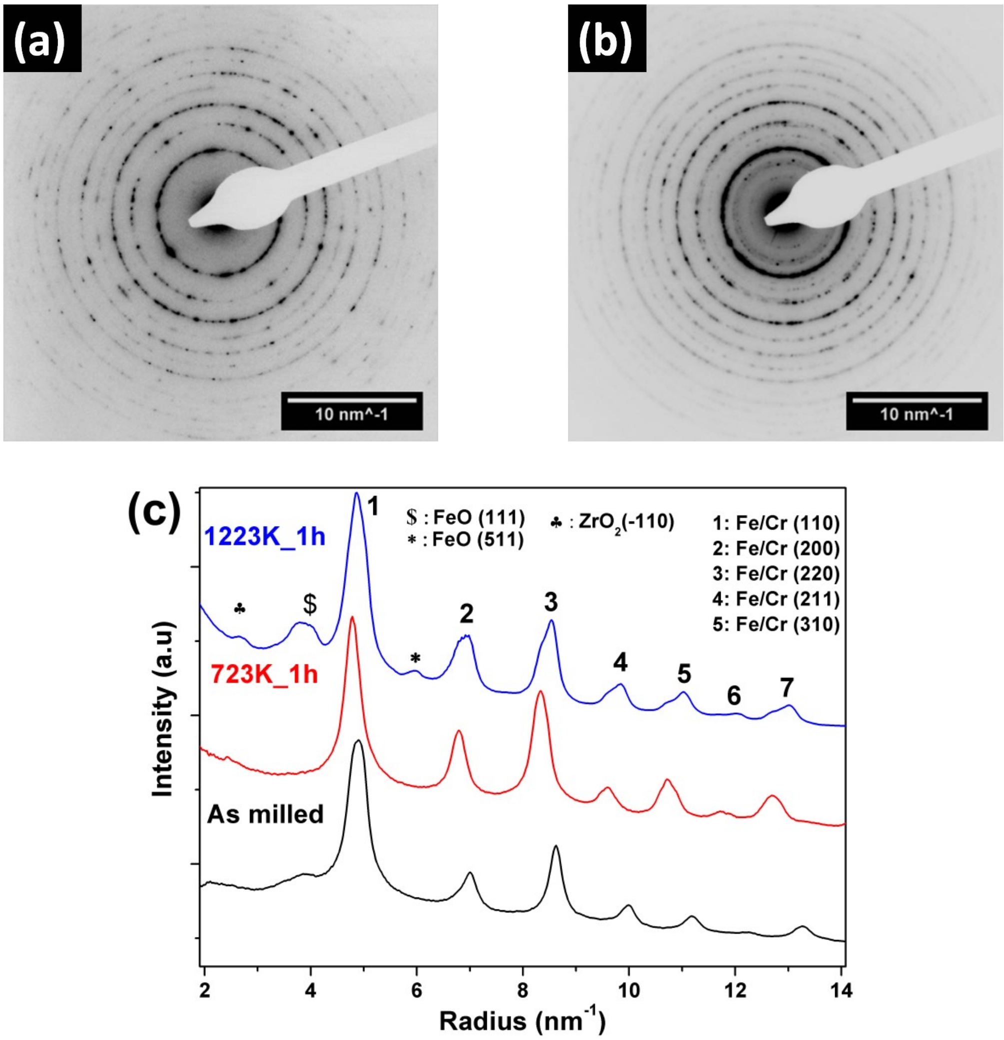

**Figure 5.6: SAED patterns of powder annealed at (a) 723 K (b) 1223 K. The radial profile of (a) and (b), along with the as milled powder SAED is shown in (c)**

### 5.3.3 Microstructural investigation by TEM

For a precise measurement of size of the minor phases, such as the $ZrO_2$ dispersoids and FeO precipitates, in the 1223 K annealed sample, TEM investigations, all from the same area of the sample, are presented in figure 5.7. Figure 5.7(a) shows the BF micrograph of the sample. The observed diffraction contrast in the micrograph shows the nc structure of the material. Figure 5.7(b) shows DF micrograph corresponding to (110) of Fe (matrix phase). It is interesting to observe that, even after annealing at 1223 K for 1 h, the matrix Fe phase still retained their nanocrystallinitymeasuring, ~ 10 – 150 nm, possibly owing to Zener Pinning effect [12] from the other nc phases present in the system. Retention of nc structure in this ODS steel powder is indicative of its good thermal stability at elevated temperatures. Additionally the (111) reflections of FeO precipitates and $(\bar{1}10)$ reflections of $ZrO_2$ dispersoids were utilized for obtaining the DF micrographs corresponding to the FeO and $ZrO_2$ phases and shown in figure 5.7(c) and 5.7(d) (marked with arrows), respectively. The micrographs show a uniform distribution of nanocrystalline FeO and $ZrO_2$ dispersoids in the material.

Further, the statistical analysis of crystallite size distribution of all the phases in material viz., Fe (matrix), FeO precipitates and $ZrO_2$ dispersoids are carried out and shown in figure 5.7(e) by means of cumulative frequency plots. A cutoff is chosen at 95% of cumulative frequency and the sizes of phases at this cut off are measured. As is observed, the crystallite sizes at this cut off are ~16 nm, 11 nm and 36 nm for FeO precipitates, $ZrO_2$ dispersoids and for Fe (matrix), respectively. This clearly hints at its exceptional thermal stability of the constituent phases and important from the view

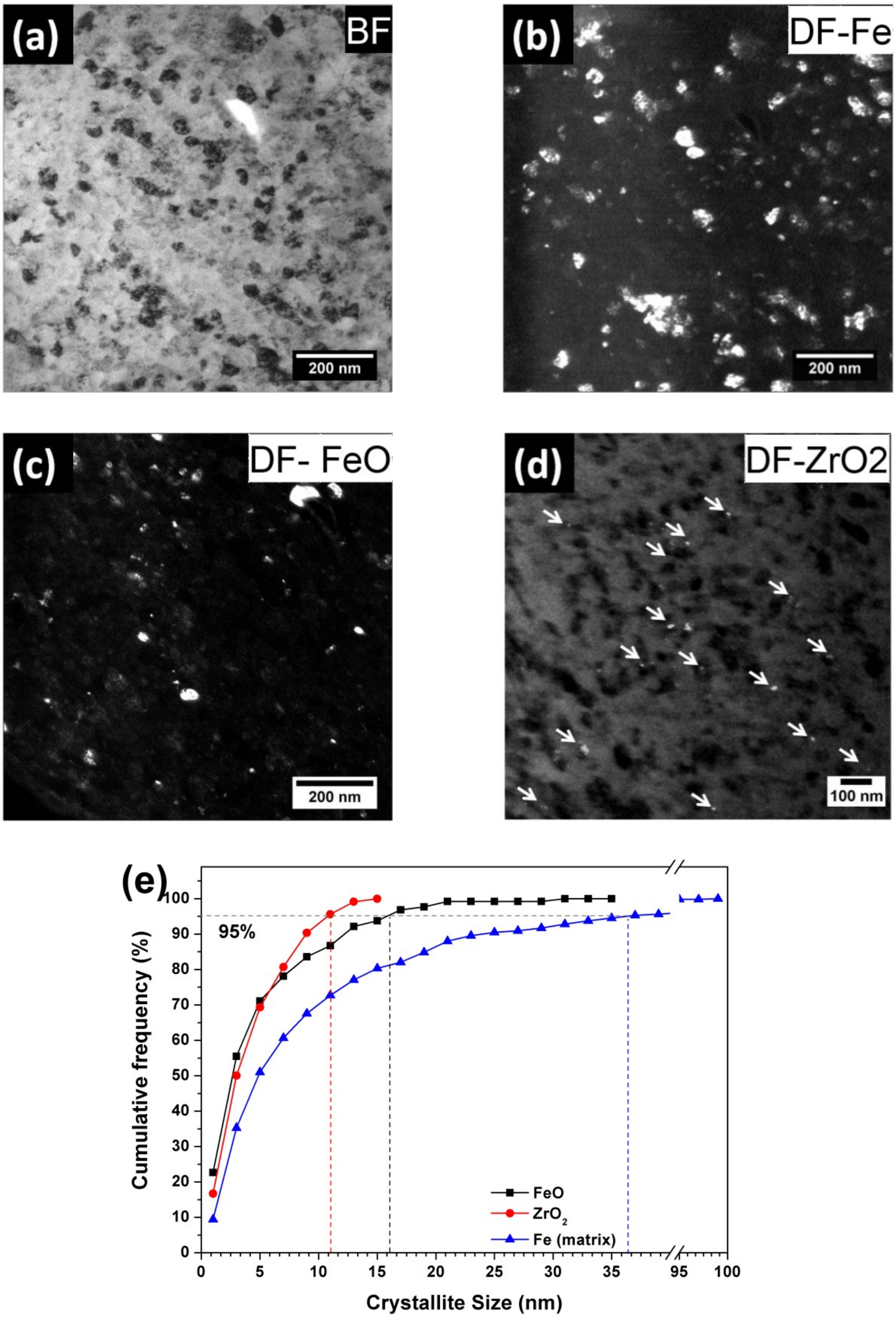

**Figure 5.7: TEM results of ODS steel powder milled and annealed at 1223 K (a) BF (b) Fe DF (c) FeO DF (d) $ZrO_2$DF (e) crystallite size distribution of $ZrO_2$ and FeO**

point of its high temperature mechanical properties. The measured size of Fe crystallites (matrix) are also in good agreement with the XRD measured sizes discussed previously. For further analysis of dispersoids and precipitates in the matrix, phase contrast microscopy has been carried out. Atomically resolved micrographs for the Fe matrix, m-$ZrO_2$ dispersoid and FeO precipitate are shown in figure 5.8 (a), (b) and (c), respectively.

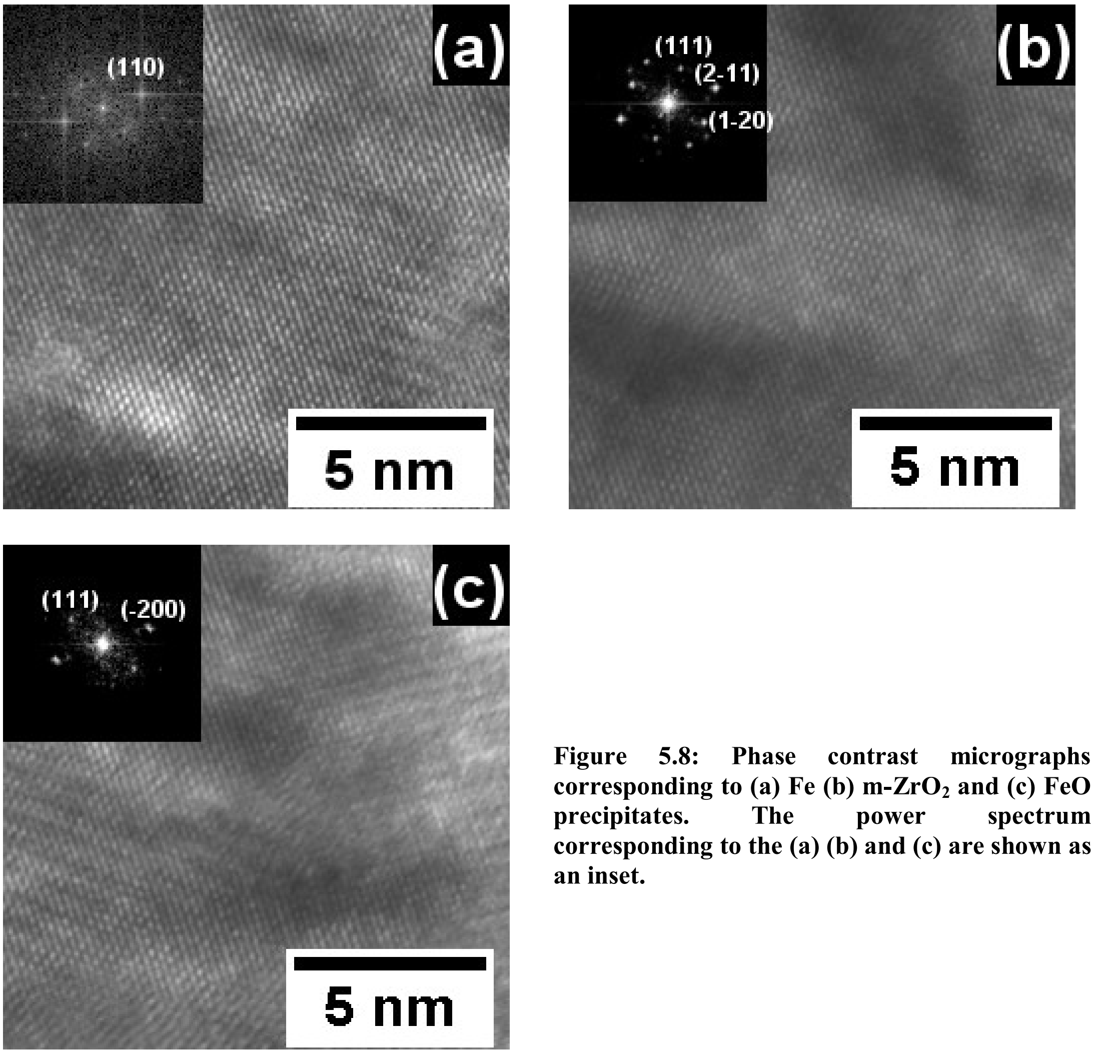

**Figure 5.8: Phase contrast micrographs corresponding to (a) Fe (b) m-$ZrO_2$ and (c) FeO precipitates. The power spectrum corresponding to the (a) (b) and (c) are shown as an inset.**

The lattice spacing as well as the inter-planar angles are measured by generating the power spectra from each of the phase contrast micrographs and shown as an inset. For all the micrographs, the lattice planes have been indexed and have been marked in the power spectrum. In a few regions of the micrographs, lattice distortion can be observed which can be attributed to the presence of localized strains [13]. Analysis of the phase contrast TEM images confirms the presence of m-$ZrO_2$ and FeO which is in support of the diffraction based characterizations, discussed earlier.

This is noteworthy from the above observations that, the material has nc matrix phase, dispersoids and precipitates in it. FeO precipitates in ODS alloys in also been reported earlier [14] but it fails to mention any consequences of their presence in the material. But dispersion strengthening by FeO in case of Fe alloys has been reported in the literature [15]. In this case, considering their fineness, stability and homogeneity, the FeO precipitates are expected to act as a precipitation strengthener to the material. This is because; the fine precipitates, similar to the dispersoids will act as a barrier to the dislocation motion, impedes the grain growth, as well as sinks for trapping of radiation-generated point defects. The FeO may also be called as autogenous dispersoids in this system. The retention of fine structure of $ZrO_2$ is in line with the reports of Xu et al [16], where the authors reported fine $ZrO_2$ particles with an average size ~3.5 nm even after annealing at 1173 K for 1 h in a Fe-14Cr-1.5Zr alloy. The authors also stated that, the size and dispersion of the $ZrO_2$ particles are comparable to those of Y–Ti–O oxides in conventional ODS alloy. These nano $ZrO_2$ particles are also known to have good He trapping ability and when subjected to 200 keV He irradiation[17]. As a whole, the nanostructured matrix, ultra-fine $ZrO_2$ dispersoids and fine FeO precipitates are believed to be efficient strengtheners to the material.

## 5.4 Conclusions

A 9Cr ODS steel powder with novel $ZrO_2$ dispersions was synthesized and subsequently exposed to high temperatures. SEM, TEM, EDS and XRD tools were used for characterizing the material. Following important conclusions were drawn from the analysis.

- ODS powder synthesized at optimum ball mill conditions showed powder particles reduced to 1 - 10 μm in size. TEM DF analysis showed that the crystallites were reduced to nanometric sizes, the majority are under 5 nm size.
- The matrix (Fe) phase still observed to be nanocrystalline, with ~ 95% of crystallites measuring < 36 nm after annealing at 1223 K for 1 hr. The results are also confirmed with XRD analysis by W-H method.
- The $ZrO_2$ dispersoids shown exceptional thermal stability even after annealing at 1223 K. The dispersoids retained their fine nanocrystalline structure; with ~ 95% of crystallites measuring sizes < 11 nm. Additionally, the matrix phase is also shown to be nanocrystalline.
- Annealing also revealed the presence of non-stoichiometric FeO precipitates in the powder. It has been observed that ~ 95 % of the FeO precipitates are under ~16 nm in size, as observed from the DF analysis.
- A stable nanostructured bcc matrix, ultrafine $ZrO_2$ dispersoids and fine FeO precipitates, all in unison, are expected to be beneficial in terms of its high-

temperature mechanical properties and enhanced void swell resistance of the material.

## 5.5 References

1. Ukai, S., *et al.*, *Materials Science and Engineering: A* (2009) 510–511, 115
2. Ukai, S., *et al.*, *Journal of Nuclear Materials* (1993) 204 (0), 65
3. Sundararajan, G., *et al.*, *Current Science* (2013) 105 (8), 1100
4. Sun, Q. X., *et al.*, *Journal of Alloys and Compounds* (2014) 598 (0), 243
5. Carson, J. W., and Pittenger, B. H., (2013)
6. Mirchandani, P. K., *et al.*, Aluminum-base composite alloy. Google Patents(1992)
7. Murty, B., and Ranganathan, S., *International materials reviews* (1998) 43 (3), 101
8. Khatirkar, R. K., and Murty, B. S., *Materials Chemistry and Physics* (2010) 123 (1), 247
9. Suryanarayana, C., *Progress in Materials Science* (2001) 46 (1–2), 1
10. Suryanarayana, C., *Mechanical Alloying And Milling*. Taylor & Francis: 2004
11. Bonetti, E., *et al.*, *Journal of Applied Physics* (2001) 89 (3), 1806
12. Koju, R. K., *et al.*, *JOM* (2016) 68 (6), 1596
13. Rentenberger, C., *et al.*, *Scripta Materialia* (2004) 51 (8), 789
14. Vijay, R., *et al.*, *Metall and Mat Trans A* (2013) 44 (3), 1611
15. Korznikov, A. V., *et al.*, *Acta Metallurgica et Materialia* (1991) 39 (12), 3193
16. Xu, W. Z., *et al.*, *Journal of Nuclear Materials* (2014) 452 (1–3), 434
17. Xu, W., *et al.*, *Journal of Nuclear Materials* (2016) 469, 72

## Chapter VI

# Microstructural characterization of consolidated $ZrO_2$ dispersion strengthened ferritic steel

---

### 6.1 Introduction

The previous chapter discussed the microstructure and chemistry of as synthesized and annealed 9Cr $ZrO_2$ ODS powder. This analysis dealt with influence of milling parameters and temperature effects on the powder. It is now important to understand the consolidation behavior of 9Cr $ZrO_2$ODS steel and consequently, this chapter describes the result of a $ZrO_2$ dispersed ODS steel consolidated by means of SPS. This chapter essentially deals with the understanding of microstructure and mechanical properties of 9Cr $ZrO_2$ODS steel and is arranged in the following manner. Chapter begins with a brief introduction to the subject in section 6.1 followed with a note on the selection of sintering temperature and pressure in section 6.2. The relative density has been reported in section 6.3 and microstructure of the as SPS samples is discussed in 6.4. The conventional normalizing and tempering (N&T) treatment is carried out to homogenized SPS specimens and its stability during the thermal exposure at service condition (973 K) has been analyzed through EBSD and discussed in section 6.5. TEM investigations of the N&T and thermal exposed samples are discussed in section 6.6. An attempt is made to assess the mechanical properties using experimental and predictive tools and discussed in section 6.7. The major conclusions drawn from the studies are summarized and listed in section 6.8.

## 6.2 Consolidation of ODS steel powders by SPS – selection of temperature and pressure

The consolidation of powder materials through SPS is gaining interest in the recent past owing to their very high heating and cooling rates and drastically low holding times (typically ~ 10 min). As a result of beneficial aspects of SPS, there is a growing attention in consolidation of ODS steels through SPS technique. During SPS, owing to the low hold times, the material is known to prevent grain growth and retain the fine structure of dispersoid, which otherwise may coarsen during consolidation. Thus the major advantage with SPS is that, intrinsic properties of the nano powders are retained in the consolidated products leading to dense products with improved properties [1]. However, the choice of temperature and pressure and their variation profiles during SPS of ODS steel powders is known to play a crucial role in mechanical properties of the material being developed [2, 3].

**Table 6.1: Important literature reports on SPS consolidated ODS steels**

| Sl. No. | System | SPS Conditions<br>Temperature_Pressure_Duration | Ref. |
|---|---|---|---|
| 1. | 9Cr ODS | 1323 K_50MPa_6 min | [4] |
| 2. | 9Cr ODS | 1223 K_40MPa_5min | [5] |
| 3. | 9Cr ODS | 1223 K_40MPa_5min | [6] |
| 4. | 9Cr-1Mo ODS | 1073 K_30MPa_10min | [7, 8] |
| 5. | 12Cr ODS | 1273 K_50Mpa_5 min | [9] |
| 6. | 13Cr ODS | (1098 K – 1163 K)_(70-80) MPa_>3 min | [10] |
| 7. | 14Cr ODS | 1323 K_70MPa_10min | [11] |
| 8. | 14Cr ODS | (1023 K - 1223 K)_80MPa_7min | [12] |
| 9. | 14Cr ODS | (1223 K – 1298 K)_40MPa_5min | [3] |

The choice of temperatures for SPS varies over a wide range from ~ 1073 K to 1373 K and pressure varies from 30 – 80 MPa in the reported literature of which important ones are consolidated in Table 6.1. It was observed from the studies that, the increase of relative density and decrease of porosity was found to occur with increase in sintering temperature from 1223 K to 1323 K. Whereas, the compaction behavior saturated for further increase of sintering temperature (beyond 1323 K). In the current study, SPS is carried out at 1323 K at a pressure of 50 MPa, for a hold time of 10 minutes. The analysis of the dense products is discussed in the following sections.

### 6.3 Density Measurement of consolidated 9Cr $ZrO_2$ ODS steel

The density of the consolidated specimen is calculated by Archimedes principle. The SPS consolidated samples are machined from various regions and used for the density analysis. The objective here was to calculate an overall average density of the sample and also to get the best samples for further microstructural analysis. The measured values of the samples taken from various regions of the consolidated specimen are tabulated in Table 6.2 below.

**Table 6.2: Measured densities of 9 Cr $ZrO_2$ ODS**

| Specimen No. | Relative Density (%) |
|---|---|
| 1 | 92.42 |
| 2 | 94.80 |
| 3 | 95.67 |
| 4 | 93.96 |
| 5 | 94.17 |
| **Average** | **94.20** |

It can be observed from the above table that, relative densities vary between ~ 92 – 95% with an average of ~94%. This indicates a uniform distribution of porosity and less probability of local inhomogeneity within the sample during consolidation and indicates that the sintering parameters are optimum to achieve the higher efficiency of thermal energy aided in faster diffusion in compaction.

## 6.4 Microstructure of as-SPS 9Cr $ZrO_2$ ODS Steel

Typical microstructure of the as-SPS steel is shown in figure 6.1(a). The specimen showed a fairly homogeneous distribution of grains and pores, and the grain features were clearly smaller. The overall distribution of pores is about ~50-80 nm size and exhibits a tendency to network along grain boundaries. Figure 6.1 (b) shows the corresponding EBSD IPF - Z map superimposed with grain boundary, after the standard post processing (to assign average orientation to non-indexed points based on its surrounding pixels). It reveals equiaxed grain morphology with nearly similar grain shape/size. Grain boundaries with a misorientation 5 – 15° and > 15° were identified as high angle and low angle boundaries respectively. The average grain size was measured to be 0.8 ± 0.3μm. The colors denote the type of crystallographic plane aligned with the sample surface and the myriad of colors denotes an essential random type of texture in the specimen. In addition to this, the resultant grain boundary distribution results show that low energy low angle grain boundaries in as-SPS condition is ~ 14%, in contrast to theoretical values (~2%) [13]. This could be attributed to the rapid coarsening of crystallites during consolidation, which leads to boundaries with low angle type. In addition, grain growth kinetics is restricted in the process due to minimum holding time at high temperature during consolidation and subsequent pinning effect of dispersoids. This pinning effect tends to restrict the boundary migration and also result in persistant low angle boundaries. Figure 6.1 (c) displays KAM distribution (0.5° – 5°) across neighboring pair of pixels with grain boundary (>10°). It provides a qualitative mapping of the degree of deformation during consolidation. The distribution of local misorientation in sample is found to be highly non-uniform as shown in figure 6.1 (c), which is attributed to the heterogeneous nature of strain localization at the grain boundaries and within the grains with a average 0.9º KAM value across all the grains, irrespective of their shape/size and orientation, implies the restricted diffusion steered phenomena during the consolidation process.

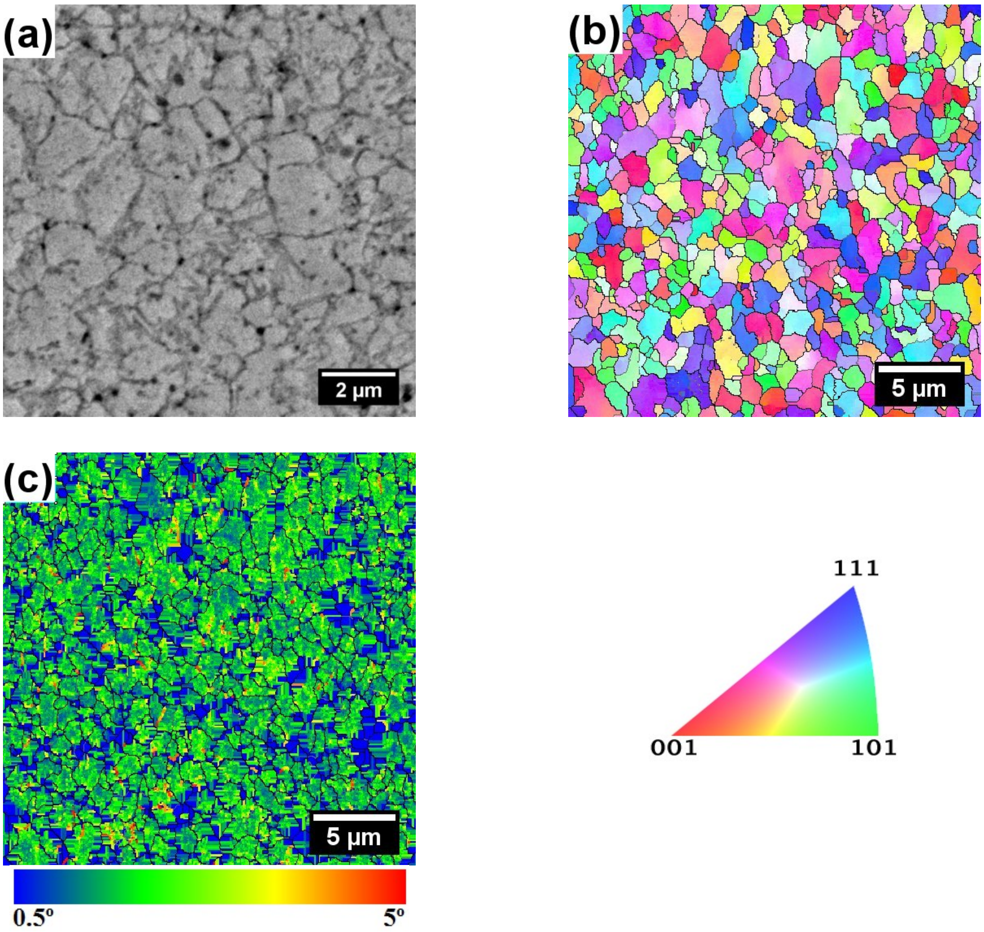

**Figure 6.1. Microstructure of as-SPS 9Cr $ZrO_2$ODSsteel (a) SEmicrograph, EBSD map of (b) inverse pole figure and (c) KAM distribution with grain boundary (>10º) contour (black line).**

Figure 6.2 shows the TEM microstructure of the as-SPS 9Cr $ZrO_2$ODS steel. The diffraction contrast from the figure 6.2 (a) reveals a microstructure, in which some fine faceted ferrite grains with high dislocations density are seen. This is indicative of retention of strain even after consolidation. In addition to it, few larger precipitates are also seen from this figure. TEM investigation at higher magnification revealed the presence of uniform distribution of nano-sized particles inside the grains (figure 6.2 (b)). It is observed from the above analysis that these nano-sized precipitates in the matrix after consolidation through SPS retains their fine size ranging between 2- 10nm.

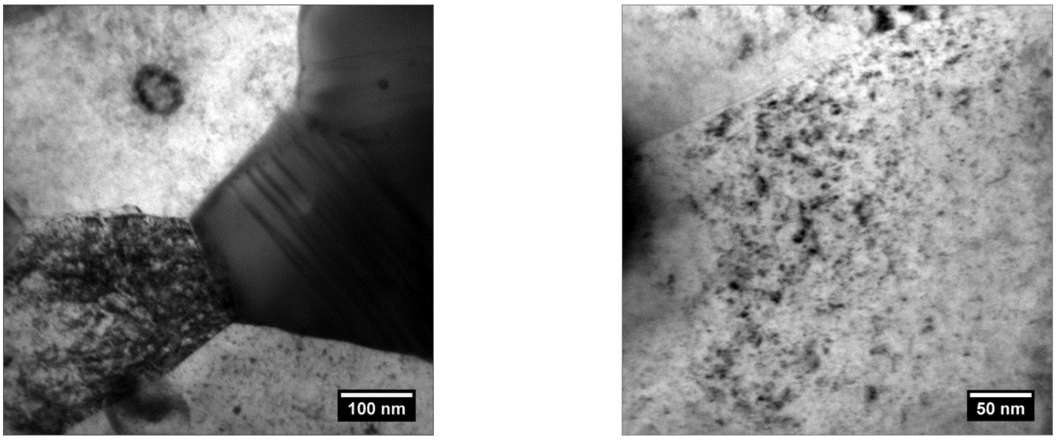

**Figure 6.2: TEM micrographs of as SPS 9Cr $ZrO_2$ODS steelat two different magnifications, showing (a) the grain structure and (b) a grain dispersed with finer particles**

Further, owing to this inhomogeneous microstructure as observed through TEM, it is concluded that, this issue needs to be addressed before carrying out further investigation. Accordingly, the samples were normalized at 1323 K for 1h followed by a tempering treatment at 1023 K for 1h to homogenize the microstructure and results are discussed in subsequent section.

## 6.5 Effect of high temperature thermal treatment on 9Cr $ZrO_2$ ODS Steel

Figure 6.3 (a) show the EBSD crystal orientation map of N&T 9Cr $ZrO_2$ ODS steel. It is noted that, a very similar to as SPS microstructure is observed with an average grain size of ~1 ± 0.4 μm, also exhibiting a random orientation.

Further, the long term annealing of the N&T sample at 973 K is carried out for 400 h and 1000 h, to understand the microstructural stability. The temperature here is typical at the service conditionof reactor operation and hence this study is expected to provide vital information about the material microstructure. Figure 6.3 (b) and (c) shows the corresponding EBSD crystal orientation map for the 400 h and 1000 h aged samples respectively. The grain size distribution is quantified and analysis is carried out and shown in figure 6.3(d). All three samples (N&T, 400h and 1000h) show a uniform size distribution with little shift in peak grain size towards higher values. The average value of ~ 1.0 ± 0.4μm, 1.1 ±0.5μm and 1.3 ± 0.6 μm were observed for N&T, 400h and 1000h samples; respectively. The grain size distribution of as SPS sample is also been included in the graph and shown a value of ~ 0.8 ± 0.3μm. The finer grain sizes even after prolonged annealing is indicating the superior stability of the microstructure in this time-temperature domain which could be attributed due to the presence of hasten pinning effect by uniformly distributed fine dispersoids even at 973 K.

Further, the qualitative strain analysis of the samples are carried out through KAM maps for all the samples and shown in figure 6.4. The amount of KAM distribution inside the volume of the material is used to evaluate a qualitative estimation of strain distribution [14]. The KAM maps are known to provide strain information by assigning a value for each pixel equal to the average disorientation that pixel has with its neighbors (the 1st order KAM are used for the calculation). Accordingly, the misorientation map for N&T, 400 h and 1000 h samples are obtained and shown in figure 6.4 (a), (b) and (c); respectively.

It is quite obvious from the maps that, the misorientation angle tends towards a lower distribution value from as consolidated by SPS (figure 6.1 (c)) to annealed (N&T, 400 and 1000h aged) samples. The difference is drastic from as-SPS to N&T but not much of a difference is found in going from N&T to aged specimen. To understand the same, the average misorientation angle for each of the samples is calculated and plotted in figure 6.4 (d). As explained earlier, a sharp dip in average misorientation angle from as-SPS to N&T is noticed and saturated thereon.

The sharp reduction in misorientation angle during N&T, indicates at relieve of excess strain in the material during annealing. The defects resulted due to rapid consolidation at high temperature in SPS are the major source of strain here and it is expected that, the dislocation annihilate during annealing, resulted with decrease in dislocation density and thus strain in the material. Beyond 400 h, the strain saturates, hinting at a saturation of defect density in the material, thus the stability. The superior stability of the microstructure with no substantial grain growth and saturated strain during this prolonged annealing is believed to be arising also from the stability of the dispersoids at this time–temperature domain. The dispersoids are known to effectively pin the grain boundaries thus inhibiting their growth is believed to be the case here. It can be recalled from chapter IV that, the dispersoids were quite stable at 973 K retaining their nanocrystallinity, even in a model alloy and similarly, similar stability of the dispersoids are expected here.

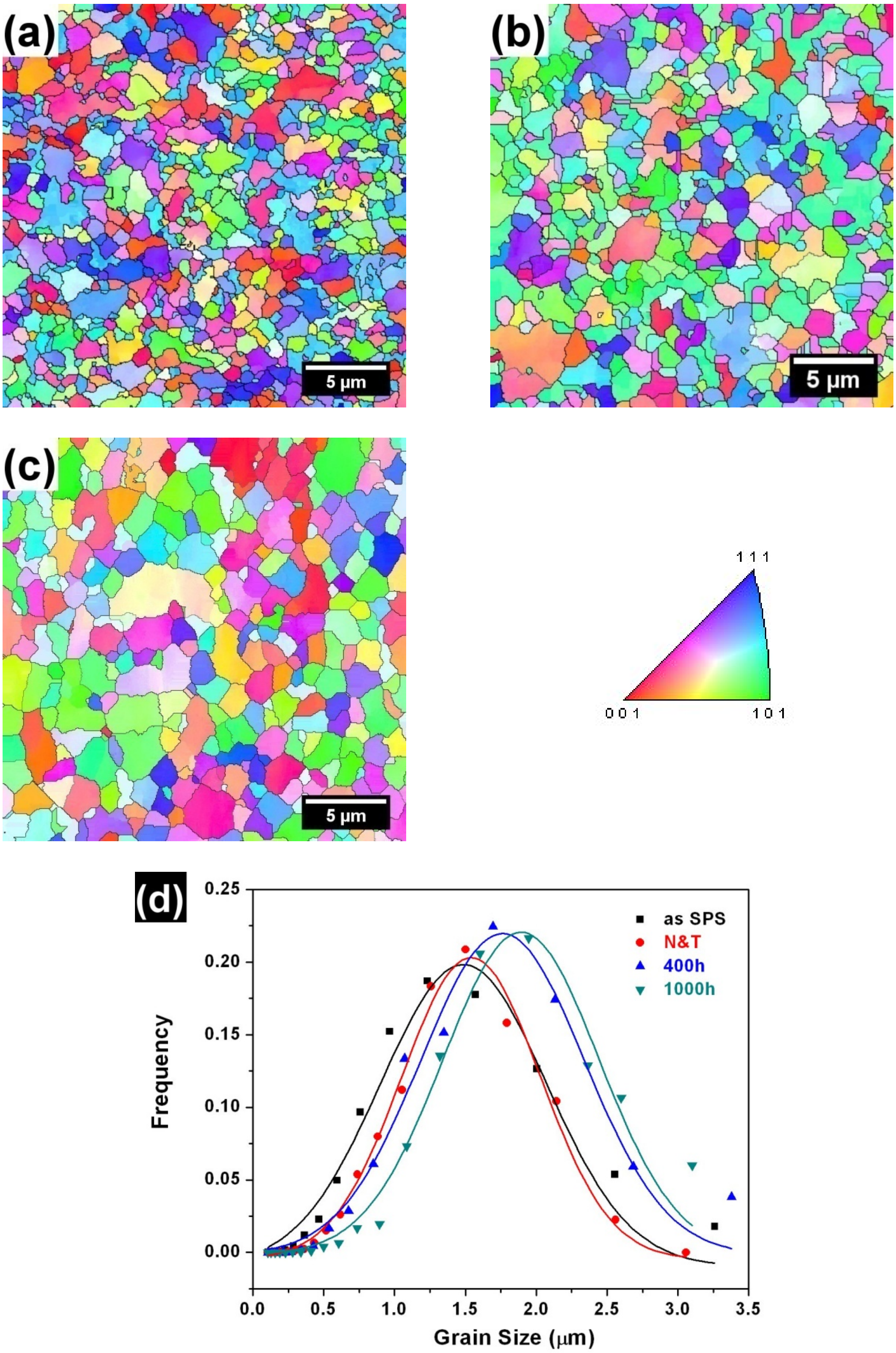

**Figure 6.3: EBSD IPF map superimposed with grain boundary (>10º) of (a) N&T, (b) 400h and (c) 1000h aged specimen, and (d) comparative grain size distribution map**

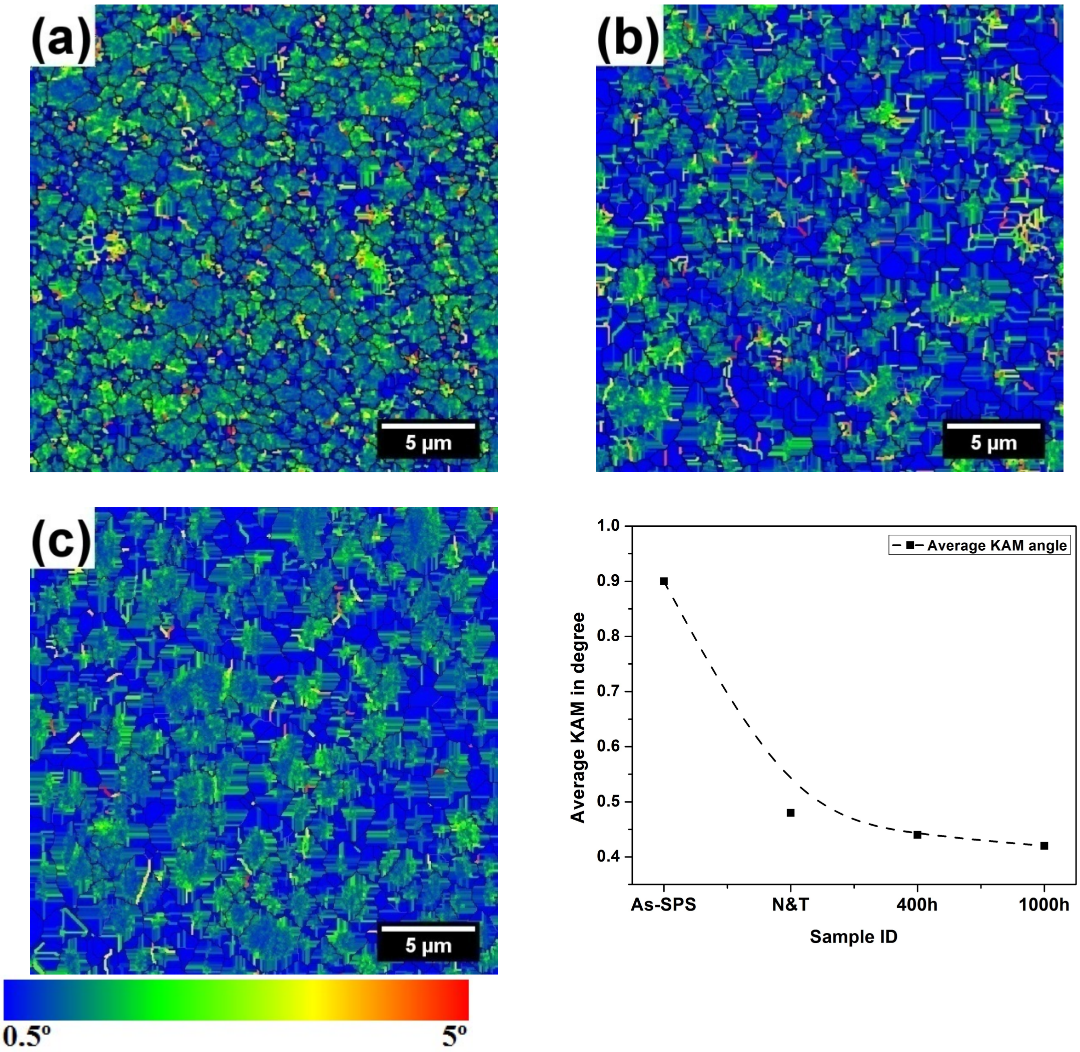

**Figure 6.4: EBSD lay over image of KAM distribution with grain boundary (>10°) contour (black line) of (a) N&T, (b) 400h and (c) 1000h aging and (d) average KAM angle distribution of 9Cr ZrO$_2$ODS steel**

## 6.6 Microstructural analysis by TEM

To shed more light on the microstructural stability displayed by the sample, as seen via EBSD analysis, further investigation through TEM is carried out and discussion is made herewith.

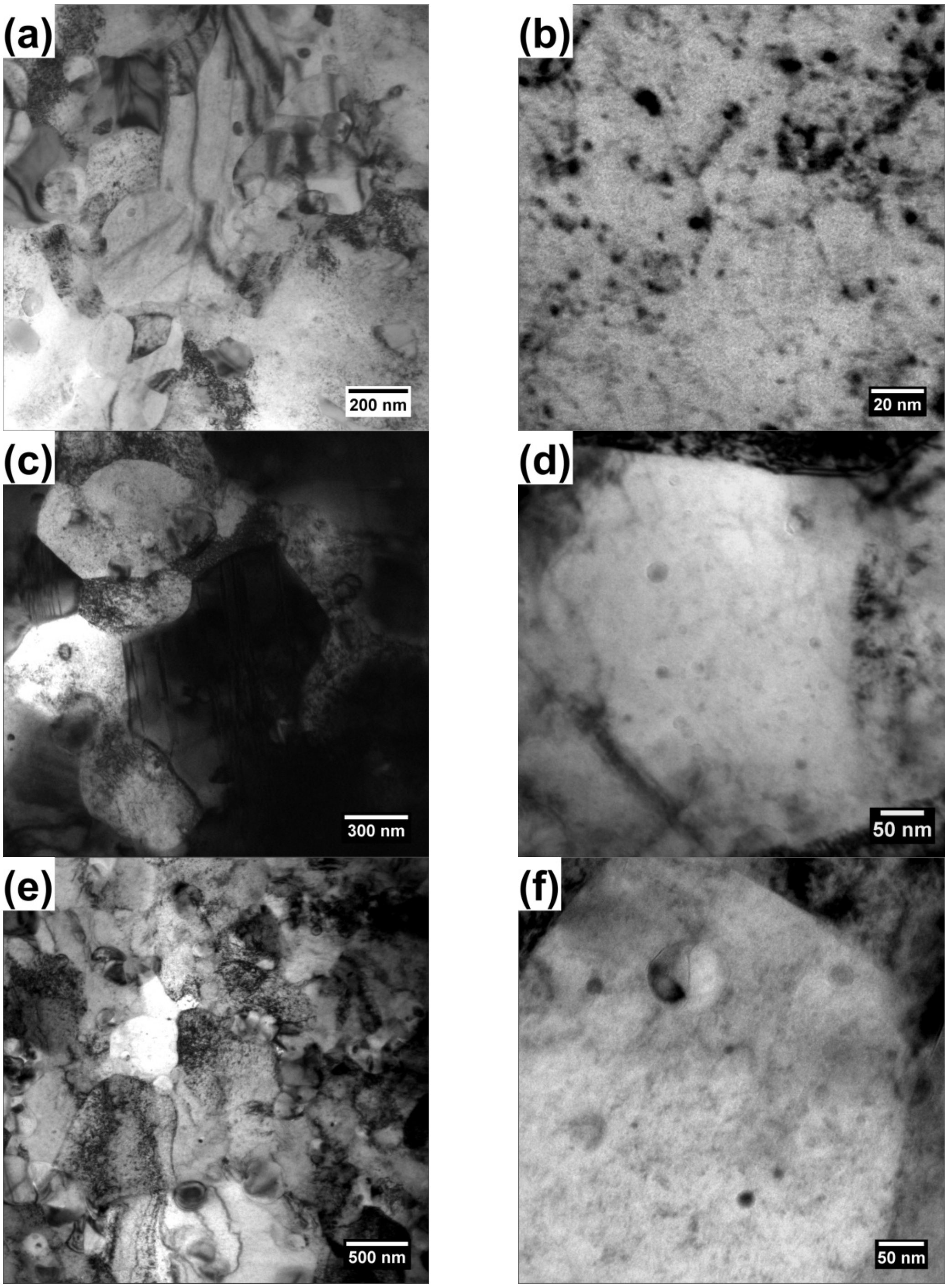
(a)
200 nm
(b)
20 nm
(c)
300 nm
(d)
50 nm
(e)
500 nm
(f)
50 nm

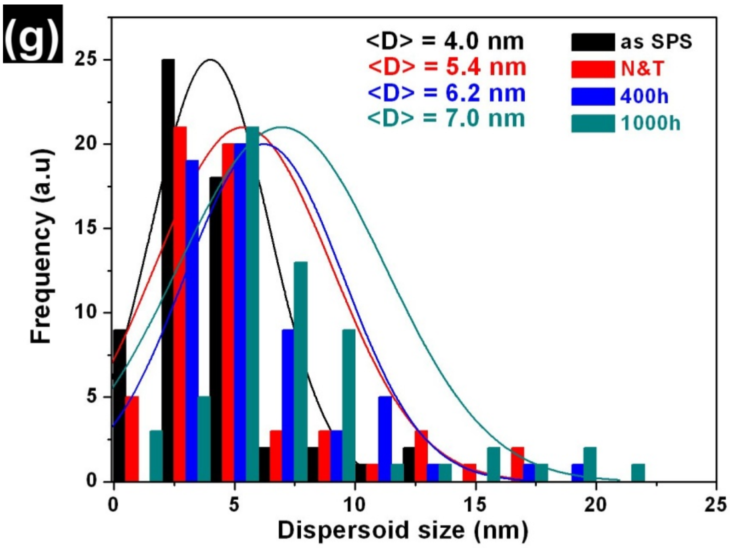

**Figure 6.5**
**(a) & (b) BF micorgraphs of N&T $ZrO_2$ ODS steel**
**(c)&(d) BF micorgraphs of 400 h annealed sample**
**(e)&(f) BF micorgraphs of 1000 h annealed sample**
**(g) Dispersoids size ditribution histogram for as SPS, N&T and long term annealed samples**

Figure 6.5 (a) shows the TEM BF micrograph of N&T sample exhibiting a finer microstructure. Owing to a small quantity of carbon (~0.01 Wt. %), the martensitic structure is not obviously seen but only finer martensitic lath features are revealed. Figure 6.5 (b), shows the BF micrograph at a higher magnification, showing uniformly distributed nano-dispersoids. Further, the microstructure of long term annealed samples are also investigated and shown in the figure. Figures 6.5 (c) and (d) displays the BF micrographs correspond to 400 h annealed at low and high magnifications, respectively. A matrix with equiaxed grains, in line with the EBSD analysis is observed here also. The nano features as seen in from a grain interior in figure 6.5 (d), shows the retention of fine nature of these features. The results are incessant with 1000 h annealed samples also, and shown in figure 6.5 (e) and (f). Further, the quantification of nano-dispersoids in the materials is carried out through and the results are summarized in figure 6.5 (g), which shows a dispersoid size distribution histogram. The size distribution for as-SPS sample is also shown in the graph. It is quite evident from the figure that, the dispersoids retain their fine structure throughout the annealing duration with an average size varying from ~ 4 nm in the as SPS sample to ~ 7 nm after 1000 h annealing, exhibiting extraordinary stability by the dispersoids. Additionally, the normal distribution to the histogram is also plotted and shown in the graph, which reveals that, the distribution of sizes is relatively narrower for the as-SPS sample in comparison to 400 h and 1000 h samples. Also, it was observed that, the peak of the size distribution chart is shifting slightly towards a higher size from N&T to 1000 h.

## 6.7 Evaluation of Mechanical Property from hardness measurements

### 6.7.1 Hardness measurements

The microstructural analysis as discussed earlier, indicated at a stable microstructure with ultrafine grains and high-density of nano-scale oxides. Attempts are made here to correlate the observed behavior to mechanical properties through Vickers hardness measurements. Table 6.3 shows the variation of hardness for 9Cr $ZrO_2$ ODS steel under different conditions. A hardness value of ~ 479 $HV_{0.05}$ (measured using 50g load) is observed in as SPS sample, which decreased to ~ 402 $HV_{0.05}$ after N&T. Further, the hardness shows a little dip in going from N&T to 400 h, but shows saturation from 400 h to 1000 h. The results can be correlated to the EBSD analysis wherein, the KAM map showed an initial dip in strain from N&T to 400 h and saturation from 400 h to 1000 h. As discussed earlier, the observed behavior is attributed to the annihilation of strain during the prolonged annealing, which essentially takes place during the initial hours. The saturation of hardness from 400 h to 1000 h is also consistent with the comparable grain sizes and dispersoid sizes at these conditions. The retention of a high hardness value even after a long-term thermal exposure at 973 K is believed to be beneficial from its application point of view.

**Table 6.3 : Comparison chart for hardness**

| Sl. No | Sample ID | Hardness ($HV_{0.05}$) |
|---|---|---|
| 1 | $ZrO_2$ ODS: as SPS | 479±79 |
| 2 | $ZrO_2$ ODS: N&T | 402±26 |
| 3 | $ZrO_2$ ODS: 400h | 378±22 |
| 4 | $ZrO_2$ ODS: 1000h | 374±20 |

### 6.7.2 Estimation of Yield strength

To understand the strengthening behavior in the 9Cr $ZrO_2$ ODS steel due to the contribution from dispersoids and fine grains, the microstructural details discussed so far are utilized and arrived at an estimation of yield stress. The yield stress at room temperature may be estimated from [15],

$$\sigma_y = \sigma_m + \sigma_d + \sigma_i \tag{6.1}$$

Where, $\sigma_m$is the matrix yield stress, $\sigma_d$ is the direct strengthening due to the dispersoids or nano-clusters, and $\sigma_i$ is the indirect strengthening due to the Hall–Petch effect. The direct strengthening due to dispersoids may be written as [3],

$$\sigma_d = \frac{MGb}{d_p}\left[\frac{6f}{\pi}\right]_{1/2} \tag{6.2}$$

Where, M, G, b are Taylor factor, shear modulus and the Burgers vector, respectively. The strengthening due to dispersoids can be estimated with an input from the volume fraction f of the dispersoids and its diameter, $d_p$. The indirect strengthening due to grain size is also known as Hall-Petch strengthening and can be calculated from,

$$\sigma_i = k * d^{-1/2} \tag{6.3}$$

Where k is a Hall-Petch constant and d is the grain size.

The analysis of yield stress is carried out for N&T, 400 h and 1000 h samples. The grain size and average dispersoid diameter are obtained from the EBSD and TEM investigations, as discussed earlier. The other material related parameters for the calculation of yield stress are taken from literature and listed in Table 6.4.

**Table 6.4:The material constants used in the estimation of yield stress**

| Parameter | Value | Ref |
|---|---|---|
| Taylor factor, M | 3.06 | [15] |
| Shear modulus, G | 80 GPa | [15] |
| Burgers vector, b | 0.248 nm | [15] |
| Hall Petch constant, k | 0.2 MPa $m^{1/2}$ | [16] |

The various contributions for strengthening in 9Cr $ZrO_2$ ODS are evaluated using the above parameters and summarized in figure 6.6.

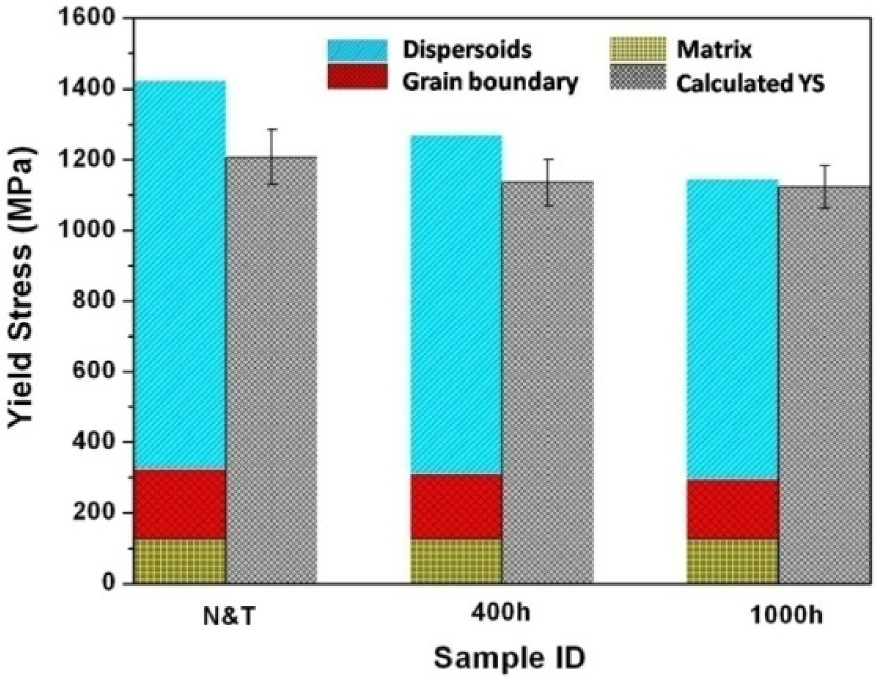

**Figure 6.6: Comparison of measured and calculated yield stress. The various contributions to strengthening through predictive tools are also listed**

It can be observed from the above graph that, the major contribution for yield strength of 9Cr $ZrO_2$ ODS steels comes mainly from dispersoids. The finer grain size also contributes substantially to the yield strength thanks to SPS. The measured yield stress mentioned in the above graph is obtained by using the numerical relation that yield stress = 3*Vickers Hardness [8]. A good correlation between measured and calculated values is obtained. The superior strength of the alloy at room temperature and a large contribution of strength from dispersoids indicate at a superior strength at elevated temperatures because dispersoids in ODS steels can suppress the dislocation movement, as well as inhibit the grain boundary migration through pinning. Thus it is expected that material shows superior properties even at high temperatures.

## 6.8 Conclusions

- The consolidation of 9Cr $ZrO_2$ ODS powder through SPS is carried out and a specimen of ~ 94% density is obtained.
- Microstructure of as-SPS sample characterized through EBSD and TEM revealed a fine grained microstructure. But excess strain is observed owing to large number of dislocation density, indicating an inhomogeneous microstructure.
- The studies on N&T and annealed specimens indicated an excellent stability of the microstructure with retention of fine grained structure and dispersoids. The KAM maps indicated at a drastic reduction in strain from as-SPS to N&T specimens but a saturated strain after 400 h annealing.
- The mechanical properties are measured through Vickers Hardness and correlated to Yield stress. The Yield stress is also calculated through predictive tools and a good correlation between the two are observed. Major contributor to strength was proved to be dispersoids, with a substantial contribution from fine grains.

- The stable microstructure with fine grains, stable dispersoids and high strength, indicates at promising high temperature properties of the material, thus validating the superiority of 9Cr $ZrO_2$ ODS.

## 6.9 References

1. Suárez, M., *et al.*, *Sintering Applications*, Ertuğ, B., (ed.) InTech, Rijeka, (2013), p Ch. 13
2. Li, Z., *et al.*, *Fusion Engineering and Design* (2017) 121, 159
3. Li, Z., *et al.*, *Materials Science and Engineering: A* (2016) 660 (Supplement C), 52
4. Jian Yang, Z. M. G., Wei Wei Yang, Ji Luo, Cun Guang Chen, (2013), *Materials Science Forum*
5. Lu, C., *et al.*, *Journal of Nuclear Materials* (2016) 474 (Supplement C), 65
6. Xie, R., *et al.*, *Fusion Engineering and Design* (2017) 115 (Supplement C), 67
7. Rajan, K., *et al.*, *Metall and Mat Trans A* (2013) 44 (9), 4037
8. Rajan, K., *et al.*, *Materials Science and Engineering: A* (2012) 558 (Supplement C), 492
9. Chang, Y., *et al.*, *Powder Metallurgy* (2014) 57 (2), 103
10. Staltsov, M. S., *et al.*, *Nuclear Materials and Energy* (2016) 9, 360
11. Hilger, I., *et al.*, *Journal of Alloys and Compounds* (2016) 685 (Supplement C), 927
12. Pasebani, S., and Charit, I., *Journal of Alloys and Compounds* (2014) 599, 206
13. Karthikeyan, T., *et al.*, *Metall and Mat Trans A* (2013) 44 (4), 1673
14. Wright, S. I., *et al.*, *Microscopy and Microanalysis* (2011) 17 (3), 316
15. Schneibel, J. H., *et al.*, *Acta Materialia* 59 (3), 1300
16. Horvath, W., *et al.*, *Computational Materials Science* (1997) 9 (1), 76

Chapter VII

# Summary and Future scope

## 7.1: Summary of the thesis

This thesis has focused on the assessment of an alternative rare earth oxide, namely monoclinic $ZrO_2$, for dispersion strengthening in ODS steel. The observations of this dissertation indicate that this alternate dispersoid is successful that it could well replace the conventional bcc $Y_2O_3$ in the next generation ODS steels.

During the course of the thesis, two alloy systems have been developed, (1) Fe – 15 $ZrO_2$ and (2) Fe-9Cr-2W-0.01C-0.35 $ZrO_2$ (all in Wt. %). The former was chosen as a model system to understand the behavior of $ZrO_2$ dispersoid during mechanical milling and subsequent annealing. The knowledge accumulated through these studies was utilized in developing the latter system, 9Cr steel with $ZrO_2$ dispersions. Some of the important results that aroused out of studies on these two systems are summarized below.

The optimization of milling duration for synthesis of Fe – 15 Wt. % $ZrO_2$ composite was based on microstructural uniformity and microchemical homogeneity of the constituents in the mechanically milled powder. After a milling duration of 100 h, a reduced and uniform powder particle size with increased sphericity with uniform mixing of the Fe and $ZrO_2$ phases was obtained. In addition, crystallite sizes of both Fe and $ZrO_2$ were reduced to size ~ 2 – 10 nm with a narrow crystallite size distribution. The behavior of dispersoids with milling was carefully followed and it was observed that, even after 100 h of milling, the $ZrO_2$ phase was found, not to amorphize unlike the widely used dispersoid $Y_2O_3$. This exceptional structural stability by $ZrO_2$ is assumed because of its smaller unit cell structure in comparison to $Y_2O_3$.

A detailed analysis on thermal evolution of Fe - 15 Wt. % $ZrO_2$ powders, mechanically milled for 100 h, has been carried out to understand the microstructural and phase transformations. A thermally stable $Fe_{0.87}O$ phase was found to be forming at 854 K. The kinetics of phase formation was estimated by KJMA analysis and the activation energy of ~195 kJ $mol^{-1}$ was calculated for this phase. Owing to its thermal stability and fineness, the $Fe_{0.87}O$ phase was deemed as an autogenous dispersoid, useful for strengthening the matrix alongside the $ZrO_2$. Additionally, metastable cubic $ZrO_2$ ($Zr_{0.9}Fe_{0.1}O_{1.95}$) was observed to be stabilized by the $Fe_{0.87}O$ at around 923 K. The phase however, was found to be unstable at elevated temperatures. Further the $ZrO_2$ dispersoids were found to retain their nanocrystallinity at 1073 K, even up to 600 min of annealing, whereas, at 1173 K, crystallites found to grow even beyond 600 min hold time. The coarsening kinetics study of $ZrO_2$, measured activation energy of ~ 379 kJ $mol^{-1}$ for the growth of $ZrO_2$ crystallites. This value, in comparison to nc $Y_2O_3$, is higher, indicating its higher resistance to coarsening. Excellent grain growth resistance and stability by $ZrO_2$ even in a concentrated alloy is thought to be beneficial aspects for its role as a dispersoid, thus strengthening the candidature of $ZrO_2$ as a dispersoid for ODS application.

The knowledge on the model alloy was then utilized in developing a 9Cr ODS steel using 0.35 Wt. % of $ZrO_2$ dispersions. The synthesis of ODS powder was carried out under optimized milling conditions and it was observed that the $ZrO_2$ crystallite sizes were reduced to a few nanometric with majority under 5 nm. Annealing studies carried out at 1223 K showed the thermal stability of the fine $ZrO_2$ dispersoids and $Fe_{0.87}O$ particles in terms of size and phase. A stable nanostructured bcc matrix with ultrafine dispersoids and fine precipitates, are expected to greatly benefit high-temperature mechanical properties and enhanced void swell resistance of the material.

First results (both nationally and internationally) in producing a consolidated 9Cr $ZrO_2$ODS steel has been reported in this thesis. SPS technique has been used for the purpose. A material with ~ 95% density was obtained with equiaxed ferrite grains measuring ~ 1 µm and a uniformly distributed nano sized dispersoids measuring 2 - 10nm. Inhomogeneous distribution of strain was observed in the as compacted steel. Conventional N&T treatment was carried out for relieving the built in stress and homogenizing the microstructure. In addition, long term thermal stability of the material at 973 K up to 1000 h was studied. A stable microstructure with minor grain growth was observed. EBSD based KAM maps indicated a significant reduction in strain from as SPS to N&T conditions. While strain levels continued to decrease with annealing at 973 K, it saturated after 400 h of annealing. The dispersoids were found to retain their fine structure even during the long term annealing. An estimate of the mechanical properties were obtained through Vickers Hardness and correlated to yield stress measurements. The yield stress was calculated through predictive tools and a good correlation between the two was observed. Major contributor to strength was found to be the dispersoids, with a substantial contribution also from fine ferrite grains. The stable microstructure with fine ferrite grains (matrix), stable dispersoids and high strength, indicates promising high temperature properties for the material, thus validating the superiority of 9Cr $ZrO_2$ ODS steel.

## 7.2: Scope for future work

This thesis has brought the success in developing a novel $ZrO_2$ dispersion strengthened steel. In line with the objectives, the thesis is has established $ZrO_2$ as an alternate dispersoid through rigorous investigation on model alloy and preliminary studies on the $ZrO_2$ dispersed steel. However, much needs to be done towards fully establishing the development of $ZrO_2$ dispersed steel in terms of optimization of the dispersoid content, consolidation procedures so as to obtain higher densification and superior strengthening properties. As a result of this, there is plenty of scope for further investigations in this field of study. Some of the most prominent ones are mentioned below:

1. Improved consolidation of the material can be achieved with a careful optimization of SPS process parameters, which is worth investigating. Attempts can also be made to consolidate the specimen through other methods such as HIP and HE and compare it with SPS.
2. The steel produced in this study carried a fixed quantity of ~ 0.35 Wt. % $ZrO_2$ dispersoid. This is based on the typical dispersoid fraction in $Y_2O_3$ ODS steel. However, varying the dispersoid quantity and its optimization must be investigated, in order to derive the best properties of the steel.
3. The thesis carries an introductory evaluation of 9Cr $ZrO_2$ ODS steel. A detailed evaluation of microstructure and texture is a necessity for establishing structure-property correlations for a better understanding of the material.
4. There was no comparative study between $Y_2O_3$ and $ZrO_2$ based 9Cr ODS steels in the current investigation. It would be extremely interesting to investigate the

same and arrive at a definitive conclusion on superiority between the two. The comparative study can also help in understanding specific properties of the dispersoid in strengthening the material which may help in tailoring the microstructure as per the property demands.

5. The present thesis is limited to 9Cr variant of the steel. Increasing Cr content to an optimum level without significant increase in texture is a demanding subject which can be investigated in future. Owing to the presence of novel dispersoid for strengthening, every aspect of texture studies with varying Cr content will be a novel analysis with potential for exciting results.